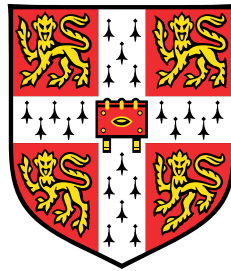


Plasmonic Sensing via Surface-Enhanced Spectroscopies



Cloudy Carnegie

Department of Physics
University of Cambridge

This dissertation is submitted for the degree of
Doctor of Philosophy

Downing College

October 2019

Dedicated to my family: Miranda, Rory, Sholto and Lorcan

Declaration

This thesis is the result of my own research undertaken at the University of Cambridge, United Kingdom. It includes nothing which is the outcome of work done in collaboration except where indicated in the text. This dissertation has not been submitted in whole or part for a degree or other qualification at the University of Cambridge or any other university and is within the specified word limit of 60,000 words.

Cloudy Carnegie
October 2019

Acknowledgements

Completing a PhD in Physics is something I'm not sure I really ever believed was possible, and I have a huge amount of gratitude to all the people who have got me here and who made my time in Cambridge a massively enjoyable and valuable period of my life, both in and out of the lab.

The first person I would like to thank is my supervisor, Jeremy Baumberg. The endless energy and dedication to your PhD students is something I am truly grateful to have in a supervisor. Thank you for always having the time to discuss science, for teaching me how to argue my ideas and for consistently pushing me beyond what I thought I was capable of.

The Nanophotonics group is such a great group and I am so glad to have been a part of it. I want to thank Felix Benz, Bart de Nijs and Rohit Chikkaraddy for getting me started in the lab when I first arrived. Thank you for being the original 'SERS team' and for helping me every step of my PhD, I have really enjoyed all our discussions as well as all the great dinners at St Johns.

Thank you to Marie-Elena Kleemann and Will Deacon for always being there for advice (both science- and life-based) and for the many hilarious escapades throughout these last three and a half years. It wouldn't have been the same without you guys!

Thank you to Yago del val Inclan Redondo, Sean Cormier, Dean Kos, Demelza Wright, Jack Griffiths, Junyang Huang, Giuliana Di Martino, Charlie Readman, Marlous Kamp, David Grys, Matthew Cheetham, Elena Pavlenko, Andrew Salmon, Ivana Lin, and the rest of the Nanophotonics group for the endless coffees, pub trips, barbecues, and conversations covering almost every topic. Who knows how many hours I've spent drinking coffee (and the occasional g&t) on those steps and putting the world to rights.

Thank you to my undergraduate personal tutor, Professor Michele Dougherty for convincing me to do a PhD, I'm definitely glad you did!

I want to thank Myfanwy James for being the best writing partner and for keeping me going from wherever you are in the world. To Alice Prodger for the many conversations and for showing me the beautiful Cambridge countryside by bike. Not much can beat a summer evening whizzing around, chatting away about all our life plans of places we want to visit!

I want to thank Cyan Williams, Fay Allen, Victoria Honour and Millie Hood for being major huns and pretty damn inspirational women. My time at Cambridge is so much better for knowing you and I'm constantly in awe of you all.

I want to give a huge thank you to Alex Casalis de Pury for your unwavering belief in me and for always making me laugh, especially when I was frustrated with all things PhD. Thank you for all our adventures.

Lastly and most importantly I want to thank my family for their encouragement and belief in me with everything I do. I am incredibly lucky to have such a supportive and incredible family. To my parents Miranda and Rory and my brothers Sholto and Lorcan: thank you for being my team. I would never be here without you.

Abstract

The research reported in this thesis focuses on the high field localisation formed in the nanometric gaps between gold nanoparticles. Sub-wavelength sized nanoparticles irradiated with light support electron oscillations known as *plasmons*, and coupling of plasmons between adjacent nanoparticles leads to hot-spots of high field enhancements in the gaps between them. The scattering processes of molecules placed in these gaps is drastically enhanced by the hot-spot, a technique utilised in *surface-enhanced Raman spectroscopy* (SERS). This thesis focuses on the optimisation of the SERS signals from these gaps. What is the limiting volume we can observe and what does this tell us about molecular interactions on the single-atom scale? Two types of nanostructure are utilised in this thesis for formation of nanometric gaps: long chain nano-aggregates and single junction nanoparticle-on-mirror structures.

The first part of this thesis explores the use of nano-aggregates for plasmonic sensing via SERS. A key parameter to control is the gap distance between adjacent nanoparticles. Here the barrel-shaped cucurbit[*n*]uril macromolecules are utilised. I show how nano-aggregates formed with CB[*n*] spacer molecules can be used for robust drug sensing of synthetic cannabinoids down to the nanomolar regime through use of reliable gap distances in conjunction with *principal component analysis* (PCA) algorithms. I also show how depositing aggregates onto a substrate can effect both the inelastic and elastic scattering, through mapping the signals across a $12 \times 12 \mu\text{m}$ area, demonstrating that although placing aggregates on a gold substrate can enhance the recorded signals, it is the inter-nanoparticle hotspots which dominate the signal.

In the second part of this thesis I look at the subtleties of metal-molecule dynamics at single junctions formed in the *nanoparticle-on-mirror* (NPoM) construct. The nanoparticle-on-mirror construct comprises of a single nanoparticle spaced above a flat gold film by a molecular spacer layer. Here the spacer layers are *self-assembled monolayers* (SAMs) which form a robust coverage of the metal film. I show that ‘picocavities (atomic protrusions from the gold surface) can be observed and studied at room temperature. A key finding is the discovery and characterisation of new ‘flare modes’ which are millisecond increases in light intensity, shown to likely come from regions of reduced local plasma frequency, indicative of a nanoparticle grain boundary.

List of publications

1. Cloudy Carnegie, Mattin Urbietta, Rohit Chikkaraddy, Bart de Nijs, Jack Griffiths, Felix Benz, William Deacon, Marlous Kamp, Javier Aizpurua, Jeremy J. Baumberg. **Plasmonic Flares: Using Ambient Nano-Optics to Track Nanoscale Grain Boundaries**. *Submitted, Nature Nano*. (2019)
 2. Cloudy Carnegie*, Jack Griffiths*, Bart de Nijs, Charlie Readman, Rohit Chikkaraddy, William M. Deacon, Yao Zhang, István Szabo, Edina Rosta, Javier Aizpurua, Jeremy J. Baumberg. **Room-Temperature Optical Picocavities below 1 nm³ Accessing Single-Atom Geometries**. *J. Phys. Chem. Lett.* (2018)
 3. Cloudy Carnegie, Rohit Chikkaraddy, Felix Benz, Bart de Nijs, William M. Deacon, Matthew Horton, Wenting Wang, Charlie Readman, Steven J. Barrow, Oren A. Scherman, Jeremy J. Baumberg. **Mapping SERS in CB:Au Plasmonic Nanoaggregates**. *ACS Photonics*. (2017)
-
4. Bart de Nijs, Cloudy Carnegie, Istvan Szabo, Rohit Chikkaraddy, David Grys, Marlous Kamp, Charlie Readman, Marie-Elena Kleeman, Oren A. Scherman, Edina Rosta, Jeremy J. Baumberg. **Chemically Tailoring Plasmonic Hotspots for SERS Sensing**. *Submitted (ACS Nano.)* (2019)
 5. Rohit Chikkaraddy, V.A. Turek, Nuttawut Kongsuwan, Felix Benz, Cloudy Carnegie, Tim van de Goor, Bart de Nijs, Angela Demetriadou, Ortwin Hess, Ulrich F Keyser, Jeremy J. Baumberg. **Mapping nanoscale hotspots with single-molecule emitters assembled into plasmonic nanocavities using DNA origami**. *Nano Lett.* (2017)
 6. Bart de Nijs, Marlous Kamp, Istvan Szabo, Steven J Barrow, Felix Benz, Guanglu Wu, Cloudy Carnegie, Rohit Chikkaraddy, Wenting Wang, William M. Deacon, Edina Rosta, Jeremy J. Baumberg, Oren A Scherman. **Smart Supramolecular Sensing with Cucurbit[n]urils: Probing Hydrogen Bonding with SERS**. *Faraday Disc.* (2017)
 7. Marie-Elena Kleemann, Rohit Chikkaraddy, Evgeny M. Alexeev, Dean Kos, Cloudy Carnegie, William M. Deacon, Alex Casalis de Pury, Christoph Große, Bart de Nijs, Jan Mertens, Alexander I Tartakovskii, Jeremy J. Baumberg. **Strong-coupling of**

-
- WSe₂ in Ultra-Compact Plasmonic Nanocavities at Room Temperature.** *Nature Comm.* (2017)
8. Bart de Nijs, Felix Benz, Steven J. Barrow, Daniel O. Sigle, Rohit Chikkaraddy, Aniello Palma, Cloudy Carnegie, Marlous Kamp, Ravishankar Sundararaman, Prineha Narang, Oren A. Scherman, Jeremy J. Baumberg. **Plasmonic Tunnel Junctions for Single-Molecule Redox Chemistry.** *Nature Comm.* (2017)
9. Rohit Chikkaraddy, Xuezhi Zheng, Felix Benz, Laura J. Brooks, Bart de Nijs, Cloudy Carnegie, Marie-Elena Kleemann, Jan Mertens, Richard W. Bowman, Guy A. E. Vandenbosch, Victor V. Moshchalkov, Jeremy J. Baumberg. **How Ultranarrow Gap Symmetries Control Plasmonic Nanocavity Modes: From Cubes to Spheres in the Nanoparticle-on-Mirror.** *ACS Photonics.* (2017)
10. Felix Benz, Mikolaj K. Schmidt, Alexander Dreismann, Rohit Chikkaraddy, Yao Zhang, Angela Demetriadou, Cloudy Carnegie, Hamid Ohadi, Bart de Nijs, Ruben Esteban, Javier Aizpurua, Jeremy J. Baumberg. **Single-Molecule Optomechanics in “Picocavities”.** *Science.* (2016)
11. Felix Benz, Rohit Chikkaraddy, Andrew Salmon, Hamid Ohadi, Bart de Nijs, Jan Mertens, Cloudy Carnegie, Richard W. Bowman, Jeremy J. Baumberg. **SERS of Individual Nanoparticles on a Mirror: Size Does Matter, but so Does Shape.** *J. Phys. Chem. Lett.* (2016)

Table of contents

List of figures	xvii
1 Introduction	1
2 Fundamentals	9
2.1 Light-Matter Interactions	9
2.1.1 Free Electron Gas in a Metal	9
2.1.2 Plasmonic Confinement	11
2.2 Coupled Nanostructures	15
2.2.1 Coupled Plasmons	15
2.2.2 Fabrication of Coupled Nanostructures	15
2.2.3 The Nanoparticle-on-Mirror Geometry	17
2.2.4 Facets on ‘Spherical’ Commercial Nanoparticles	21
2.3 Surface-Enhanced Raman Scattering	22
2.3.1 The Raman Scattering Process	22
2.3.2 Raman Enhancement	25
2.3.3 Picocavities and the Optomechanical Description of SERS	26
2.4 Spacers for Coupled Plasmonic Systems	29
2.4.1 Cucurbit[<i>n</i>]urils	29
2.4.2 Self-Assembled Monolayers	30
2.4.3 Other Spacer Materials	32
2.5 Grain Boundaries in Metals	33
3 Experimental Details	37
3.1 Spectroscopic Techniques	37
3.1.1 Dark-Field Spectroscopy	37
3.1.2 Integrating Dark-Field with Surface-Enhanced Raman Spectroscopy	39
3.2 Auto-Detection Methods	42

3.3	Theoretical Simulations	43
3.3.1	Finite-Difference Time-Domain Simulations	44
3.3.2	Boundary Element Method	44
3.4	Sample Fabrication	45
3.4.1	Nanoparticle Aggregates	45
3.4.2	Nanoparticle-on-Mirror	46
4	Optimising SERS from Nanoparticle Aggregates	49
4.1	Aggregation Kinetics and the Formation of Chain Modes	50
4.2	Plasmonic Sensing with Principal-Component-Analysis	52
4.3	Mapping SERS in CB:Au Plasmonic Aggregates	58
4.3.1	Experimental Results	58
4.3.2	Finite-Difference Time-Domain Modelling	65
4.4	Conclusion	69
5	Observing Picocavities at Room Temperature	71
5.1	Room Temperature Dynamics	71
5.1.1	Picocavity Mode Positions	75
5.1.2	Temperature Trends	76
5.2	Breaking Molecular Symmetry in the Gap	78
5.3	Conclusion and Outlook	80
6	Broad-Band ‘Flare’ Events	83
6.1	Observation of Flare Modes	84
6.2	Multi-NPoM Analysis	86
6.2.1	Power-Dependent Measurements	89
6.3	Comparison with Other Molecular Spacers	92
6.4	Combined White-Light and Inelastic Laser Light Scattering	95
6.5	Conclusion and Outlook	97
7	Possible Origins of Flare modes	99
7.1	Black-body Radiation	100
7.2	Two-Photon Absorption and Emission	102
7.3	Hot Electrons	104
7.4	Structural Changes	104
7.4.1	The Picohole Geometry	106
7.4.2	The Nanoparticle Crack Geometry	107

7.4.3	A Grain Boundary Modelled by a Reduction in Local Plasma Frequency	108
7.5	Stimulated Electronic Raman Scattering	114
7.6	Conclusion and Outlook	115
8	Conclusion and Outlook	119
	References	123
	Appendix A Comparison of Hot-Spot Density	135
	Appendix B Room-Temperature Picocavity Examples	137
	Appendix C Derivation of the ERS Background Increase	143

List of figures

1.1	The Nanoparticle-on-Mirror Structure	5
2.1	The Drude Model Compared to Johnson-Christy data	11
2.2	Surface Plasmons	12
2.3	EM Fields Surrounding Nanoparticles	14
2.4	Techniques for the Fabrication of Coupled Nanostructures	16
2.5	The Nanoparticle-on-Mirror (NPoM) Geometry	18
2.6	Analytical Model for Coupled Mode Resonance Position of a Dimer-like System	20
2.7	Geometries of Commercial ‘Spherical’ Nanoparticles	21
2.8	The Raman Scattering Process	23
2.9	Raman and Infrared Activity	24
2.10	Raman Enhancement	25
2.11	Optomechanical Descriptions of SERS Emitted from Picocavities	27
2.12	Cucurbiturils	29
2.13	Self-Assembled Monolayers	31
2.14	Other Nanoparticle Spacers	32
2.15	Grain Boundaries in Metallic Nanoparticles	34
3.1	Dark-Field Spectroscopy	38
3.2	Integrated Raman and Dark-Field Spectroscopy	39
3.3	Dark-Field Images and Spectra	40
3.4	Automated Experimental Protocol	41
3.6	Theoretical Methods	44
3.7	Nanoparticle Aggregates	45
3.8	Formation of Self-Assembled Monolayers	47
4.1	Scanning Electron Micrographs	50
4.2	Formation of Nanoparticle Aggregates	51

4.3	Sensing THC Using Nano-Aggregates	53
4.4	Separation of Raw Data into Principal Components	55
4.5	Sensing Synthetic Cannabinoids	56
4.6	Mapping SERS Intensities Across Nano-Aggregates	58
4.7	SERS Intensity Maps	60
4.8	Plasmonic Background Maps	61
4.9	SERS and Background Counts	62
4.10	Correlation of SERS with Bright-Field Scatter	63
4.11	Dark-Field Scattering Spectra	65
4.12	Toy Model System	66
4.13	Magnitude of E field	67
4.14	Extracted Near-Field Spectra	68
5.1	The NPoM system with BPT as a molecular spacer	72
5.2	Picocavities Observed at Room Temperatures	74
5.3	Picocavity Mode Positions	76
5.4	Nanocavity and Picocavity Temperature Trends	77
5.5	Breaking Molecular Symmetry in the Gap	79
6.1	Nanoparticle-on-Mirror Structure for Single Hot-Spot Analysis	84
6.3	Gaussian Lineshape of Flare Modes	86
6.4	Occurrence Statistics of Flares	87
6.5	Plasmonic Mode Comparisons	89
6.6	Power-Dependent Analysis of Flare Modes	90
6.7	Further Power Dependent Analysis of Flare Modes	91
6.8	Comparison of Flare Modes for Different Spacer Molecules	93
6.9	Simultaneous Observation of Flare and Coupled Modes	94
7.1	Black-Body Radiation	101
7.2	Two-Photon Absorption and Emission	103
7.3	Electronic Raman Scattering	105
7.4	'Pico-hole' in a Nanoparticle Facet	106
7.5	Nanoparticle Crack	107
7.6	Grain Defect on the Nanoparticle Facet	108
7.7	Further Simulations on the Grain Defect Patch Geometry	109
7.8	Analytic Model for Patch Perturbed by ω_p at the Centre of Nanoparticle Facet	111
7.9	Comparison of Analytical Model to Simulations and Experiments	113
7.10	Stimulated Electronic Raman Scattering	115

Chapter 1

Introduction

Introduction

The study of light has been fundamental in improving our understanding of the physical world. In 1665 Robert Hooke [1] proposed that light behaved as a wave, with Thomas Young showing in 1800 that light waves could interact with each other through his famous double slit experiments, still repeated by physics students around the world today. However it was Micheal Faraday who began the era of modern optics with his proposal of light as electromagnetic radiation in 1846 [2].

Visible light is widely used today for imaging and microscopy techniques, however this typically requires that the objects of interest are on the order of the wavelength of light used to study them. For nano-scale imaging, where the object has sub-wavelength dimensions, techniques which increase the confinement of light are needed. The field of nanophotonics attempts to address this.

Nanophotonics utilises the confinement of light by plasmonic nanostructures. When incident visible light interacts with sub-wavelength structures it induces coherent oscillations of the conduction electrons within the metal. This is known as a *plasmon resonance*, the frequency of which is strongly dependent on the size, shape and material of the nanostructure [3, 4]. The plasmon resonance leads to a large enhancement of electromagnetic fields surrounding the nanostructure.

Nanostructures separated by a few nanometres support coupled plasmons, with hot-spot regions of high field intensity in the gaps between the structures. The high field intensities in these cavities can drastically enhance optically driven processes. This thesis focuses on the enhancement of vibrational scattering from molecules placed within the gap, with Surface-enhanced Raman scattering (SERS) a key technique used in the identification and sensing of very small quantities of molecules of interest.

Historical Progress in the Field

Raman scattering was discovered by C.V. Raman in the 1920s [5]. It was shown to be an inelastic scattering process which could happen alongside Lord Rayleigh's classical theory of light, which only described the elastic scattering process. Chandrashekhara Venkata Raman was born and educated entirely in India. At the start of his career Raman worked in the Civil Service as part of The Indian Association for the Cultivation of Science (IACS). His work mainly focused on optics and acoustics, in particular studying stringed instruments such as the violin and the tambura. His work quickly became well-recognised around the world, publishing 27 research papers in his first 10 years and helping to put IACS on the map. He was invited to visit London in the early 1920s, where he met and talked with J.J. Thomson and Lord Rutherford, amongst others.

After meeting Thomson and Rutherford, Raman quickly became more interested in the field of optics. It is said that he spent his 15 day return voyage by boat to India fascinated and thoughtful over considering the incredible blue colour of the Mediterranean sea. Lord Rayleigh had explained the colour of the sea by saying that it simply reflected the colour of the sky, but this explanation did not satisfy Raman. Raman outlined his thoughts on this and sent it to the editors of the journal *Nature* while docked in Mumbai, still on his journey home. Not long after, Raman and his team experimentally showed that the blue colour of the sea in fact arose from the inelastic scattering of sunlight by water molecules.

On returning to his research group in Calcutta, Raman now focused his research entirely on the study of the scattering of light. He began a series of experiments looking at how light was scattered by numerous liquids, as well as some solids. His first paper on this topic was published in *Nature* and was titled "A New Type of Secondary Radiation" [5]. He reported that his group had studied the light scattering from over 50 different liquids. All showed the same effect: some of the scattered light was of a different colour than that of the light incident on it. Raman concluded: "It is thus a phenomenon whose universal nature has to be recognised." This inelastic light scattering is now known as Raman scattering.

These original measurements by Raman and his team had solely looked at the colour changes by eye. From here he moved on to a spectroscopic analysis of the scattered light. This required careful experimental design, due to the small number of Raman scattered photons and the low intensities of light available at this time. The samples of interest were illuminated by monochromatic light, which was generated by a mercury gas discharge lamp. These liquid samples were of high concentration and volume in order to maximise the amount of Raman scattered light observed. The scattered light was recorded using photographic plates.

The significance of Raman scattering was recognised by scientists around the world, in particular with regards to quantum theory, which was still being debated. The mechanism of Raman scattering required the existence of photons and their ability to change in energy as they interacted with atoms in a molecule. R. W. Wood wrote to Nature following Raman's paper "I have verified this brilliant and surprising discovery", "it appears to me that this very beautiful discovery which resulted from Raman's long and patient study of the phenomenon of light scattering is one of the most convincing proofs of the quantum theory" [6].

Raman won the Nobel Prize in 1930 for his discovery and in his address underlined the importance of the discovery: "The character of the scattered radiations enables us to obtain an insight into the ultimate structure of the scattering substance" [7].

Technical Developments

Although Raman correctly predicted in his Nobel Prize speech that Raman spectroscopy would ultimately be used for determining "the ultimate structure of the scattering substance", in the years following his discovery it was not used much in practice, due to its very low sensitivity.

Raman scattering was discovered three decades before the invention of the laser. It was this invention in the 1960s which reignited interest in the field of Raman spectroscopy and made it a truly feasible technique of determining the chemical structure of the object of interest.

The invention of the laser has a disputed history. Schawlow and Townes of Bell Labs filed a patent application in 1958 for what they called "a proposed optical maser" as well as submitting their theoretical calculations to Physical Review [8]. At a similar time Gould published his paper "The LASER, Light Amplification by Stimulated Emission of Radiation" [9]. Decades of legal dispute between the two groups over the right to own the patent ensued.

Sensitivity of detection was also improved by the invention of charged coupled devices (CCDs). Before this monochromators coupled to photomultiplier tubes were used, with the monochromator moved in order to scan across the desired spectral range.

Filters are needed when carrying out Raman spectroscopy in order to separate the Raman scattered light from the elastically scattered Rayleigh light. Holographic notch or long-pass filters are often used. Previously the elastic light was removed by using triple-grating monochromators in subtractive mode.

Development of the Field of Plasmonics

At the same time as progress was happening in the discovery and application development of Raman scattering and spectroscopy, the field of plasmonics was being developed. It was these two fields coming together which would ultimately lead to the development of SERS as the tool which is so widely used today.

A description of the two key types of plasmons: *surface plasmon polaritons* and *localised surface plasmon polaritons* was developed from a mathematical point of view by Sommerfeld in 1899 [10] and Zenneck in 1907 [11]. Both these studies described these surface waves in the context of radio waves propagating along the surface of a conductor. This was later expanded into the visible light domain by Ritchie et al. [12] who studied the diffraction of electron beams on thin metallic foils. An important practical step was the ability to excite these surface waves, which was achieved by Kretschmann and Raether in 1968 with what is now known as the Kretschmann prism geometry [13].

Bringing together these two fields, surface-enhanced Raman spectroscopy (SERS) was first achieved by Fleischmann, Hendra and McQuillan [14] at the University of Southampton in 1973. In this experiment they measured the Raman scattered light from pyridine molecules which had been adsorbed onto electrochemically roughened silver substrates. It was debated whether the observed dramatic increase in scattering signals was due to electromagnetic or chemical effects, but it is now widely accepted that an increase in field density in the region of the molecules is the root of this enhancement.

Current Applications of SERS

The main benefit of surface-enhanced Raman spectroscopy is that it is close to non-invasive. The caveat of this is that the incident laser power must be low enough that it does not damage the sample. This has led to its application across a broad number of fields.

SERS is widely used across chemistry in order to identify molecules as well as study chemical processes and reactions. By identifying the individual bonds through their unique bond energies (corresponding to unique Raman shifts in the resulting Raman spectrum), a picture of the molecule can be built up. This is often called the ‘vibrational fingerprint’ of a molecule.

This fingerprint is also used in biological sciences and medicine. It has been used to determine the vibrational structure and investigate the functions of DNA and other proteins [15]. It has also been used to study wounds and their healing progress in situ [16]. Another important application of SERS in medicine is for cancerous tumour detection, with the benefit in contrast to other techniques that it can be label-free [17].

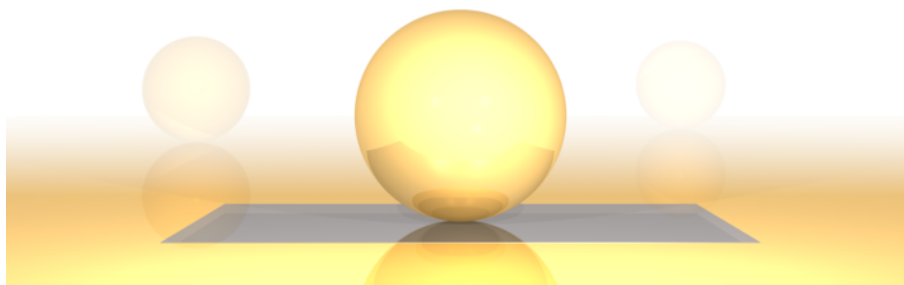


Fig. 1.1 **The Nanoparticle-on-Mirror Structure (NPoM)**

A key struggle for the field of SERS is difficulty in achieving quantitative results, hindering its ability to become a fully viable technique. There are multiple ways this issue is being approached. One way is by further increasing the confinement, and by doing so knowing the exact quantity within the achieved mode volume. The other method is by using statistical techniques, such as bioanalyte analysis to prove the number of molecules in the region of interest [41]. Single molecule SERS spectroscopy has now been achieved [28], opening up the possibility of watching chemical reactions occur on a single molecule scale. Further confinement was achieved on the observation of single atom movement was in 2016 with the discovery of ‘picocavities’ by Benz et al. [18]. This work also demonstrated that SERS measurements can be used to elucidate information on the structure and movement of the enhancement substrate itself. It is with this in mind that the research outlined in this thesis is undertaken. How can SERS as a technique be fine-tuned by optimising the plasmonic substrate? And what can we learn about the substrate itself through careful analysis of the resulting SERS spectra?

In this thesis I firstly discuss this scattering from molecules placed within the multitude of hot-spots present in long chain nano-aggregates. I show how these nanostructures are useful constructs for augmenting scattering signals, before moving down the confinement scale to investigate single junctions formed via the dimer-like ‘nanoparticle-on-mirror’ (NPoM) structure. This structure (Figure 1.1) consists of a single gold nanoparticle spaced above a flat gold surface by a molecular layer. Charges in the nanoparticle couple to image charges in the gold, forming a hot-spot of field intensity in the gap between the two. Formation of these NPoM structures is a valuable method for creating and analysing single plasmonic junctions. Within this single NPoM junction I look at cavities formed by single atoms on the nanoparticle surface, and discuss how this affects the observed scattering signals. From

here I look at additional inelastic scattering from the nanoparticle-on-mirror gap of unknown origin, and discuss possible theories to explain its origin.

Outline

The structure of this thesis is as follows:

Chapter 2 introduces the main theoretical concepts required for the subsequent experimental results. The Drude model of a free-electron gas in a metal is derived and compared to empirical data, and its implications on the formation of surface plasmons are explored. Raman scattering and its subsequent enhancement by plasmonic cavities is detailed, with a brief qualitative introduction to the optomechanic description of SERS. Coupled nanostructures, including nanoparticle-on-mirror and long-chain aggregate systems are introduced, as well as the molecular spacers required in their self-assembly. Finally a brief introduction to metallic grain boundaries in the context of plasmonics is given.

Chapter 3 describes the experimental techniques used throughout this thesis. The spectroscopic techniques used are described, specifically dark-field spectroscopy and microscopy, and surface-enhanced Raman spectroscopy. This includes a description of the measurement set-up and the particle tracking software used to integrate the two techniques in a typical automated experiment. Next, some of the theoretical simulation tools used throughout this thesis are briefly described, in particular boundary element methods (BEM) and finite-difference time-domain (FDTD) methods. Lastly, a description of the experimental protocol developed for forming both nanoparticle aggregates and nanoparticle-on-mirror samples with different molecular spacers is given.

In **Chapter 4** scattering from nanoparticle aggregates is investigated. Firstly, surface-enhanced Raman scattering measurements of many aggregates in solution are considered, with principal-component-analysis techniques described as a method for maximising the amount of information extracted from a complex system. Secondly the anchoring of nanoaggregates to surfaces in a dry environment is investigated, with comparative studies made between substrates of gold, silicon and silicon dioxide. Finally a comparative theoretical study is discussed, with a toy model simulated using finite-difference time-domain (FDTD) methods.

In **Chapter 5** the time-dependent surface-enhanced Raman scattering signals from single nanoparticle-on-mirror structures are analysed. In particular ‘picocavities’, formed by fluctuating surface gold adatoms, are discussed, with particular emphasis on the differences observed at room temperatures compared with previous studies at cryogenic temperatures [18]. In the second part of this chapter the symmetry of the molecular spacer is broken

in order to investigate the relative propensity of picocavity adatoms originating from the nanoparticle compared to the mirror.

In **Chapters 6 & 7** I discuss the emission of transient broad-band spectral features observed in high-speed CW SERS spectra. Here termed as ‘flare’ modes, this inelastic light emission is of unknown origin. In Chapter 6, I present a myriad of experimental observations and statistical analysis collected from thousands of nanoparticles in order to give clues towards the origin of these events. This includes time-dependent and power-dependent measurements, variations in molecular spacers and combined white-light and laser light scattering methods. In Chapter 7 I discuss a number of theories on the possible origin of this light emission, in light of the experimental observations in Chapter 6.

In **Chapter 8** the experimental findings of the previous chapters are summarised and future outlooks discussed.

Chapter 2

Fundamentals

In this Chapter I will briefly introduce some of the fundamental understanding required for the experimental results of Chapters 4-7. I will start by discussing the Drude model of a free electron gas in a metal and how this can be compared to empirical data. I will then briefly discuss *surface plasmon polaritons* and *localised surface plasmon polaritons* before reviewing how coupled nanostructures can be used to enhance optical processes, with particular emphasis on *surface-enhanced Raman scattering*. Finally, I will examine the different spacers which can be used in fabrication of coupled nanostructures, as well as a brief mention of the grain boundaries which can form in metallic nanoparticles.

2.1 Light-Matter Interactions

2.1.1 Free Electron Gas in a Metal

We can think of electrons in a metal behaving like a negative gas moving within a fixed three-dimensional lattice of positive ions. This is known as the *plasma model*, and will be introduced here. To consider the properties of electrons in a metal we first assume that the electrons undergo harmonic oscillator-type behaviour under the influence of an attractive electromagnetic field, \mathbf{E} . Therefore the displacement, \mathbf{x} , of a single electron with mass m^* and charge e can be described by the equation

$$m^* \ddot{\mathbf{x}} + m^* \gamma \dot{\mathbf{x}} = -e\mathbf{E} \quad (2.1)$$

where γ refers to the damping rate, and the effective mass, m^* , is the electron mass m_e , with an additional factor due to the electron moving within a crystal lattice. If we assume that both \mathbf{E} and \mathbf{x} have a harmonic time dependence of the form $\mathbf{x} = \mathbf{x}_0 e^{-i\omega t}$, $\mathbf{E} = \mathbf{E}_0 e^{-i\omega t}$, where

ω is the frequency of incident light, this results in the relation

$$\mathbf{x} = \frac{e}{m^*(\omega^2 + i\gamma\omega)} \mathbf{E}. \quad (2.2)$$

The displacement field is defined by: $\mathbf{D} = \epsilon_0 \mathbf{E} + \mathbf{P}$, where ϵ_0 is the permittivity of free space, and \mathbf{P} is the polarisation field. Therefore we can write this as

$$\mathbf{D} = \epsilon_0 \left(1 - \frac{\omega_p^2}{\omega^2 + i\gamma\omega} \right) \mathbf{E}, \quad (2.3)$$

where $\omega_p^2 = \frac{ne^2}{\epsilon_0 m^*}$ gives the *plasma frequency* of the free electron gas. The complex dielectric function of the free electron gas can be written (from the definition of the displacement, $\mathbf{D} = \epsilon \epsilon_0 \mathbf{E}$) by

$$\epsilon(\omega) = 1 + \frac{P}{\epsilon_0 E}. \quad (2.4)$$

Therefore we can write this dielectric function as

$$\epsilon = \epsilon_\infty - \frac{\omega_p^2}{\omega^2 + i\gamma\omega}, \quad (2.5)$$

where the 1 is replaced by a dielectric constant, ϵ_∞ , to account for the residual polarisation from filled d bands in noble metals. This equation is known as the Drude Model. We can split Equation 2.5 into its real and imaginary parts, where $\text{Re}[\epsilon(\omega)]$ gives the phase velocity in the metal and $\text{Im}[\epsilon(\omega)]$ gives the losses of the system.

$$\text{Re}[\epsilon(\omega)] = \epsilon_\infty - \frac{\omega_p^2}{\omega^2 + \gamma^2} \quad (2.6)$$

$$\text{Im}[\epsilon(\omega)] = \frac{\gamma\omega_p^2}{\omega(\omega^2 + \gamma^2)}. \quad (2.7)$$

These relations are plotted in Figure 2.1, alongside the experimentally determined values for gold from Johnson and Christy [19]. It can be seen that at low frequencies, the Drude model is a good fit to experiment, however at high frequencies the model breaks down due to interband transitions. In order to account for these, additional terms can be added to the model, subsequently referred to as the Drude-Lorentz model. However for the spectral region covered in this thesis (wavelengths > 500 nm), the real part dominates, and the Drude model can be taken as a good estimate for the dielectric function of gold.

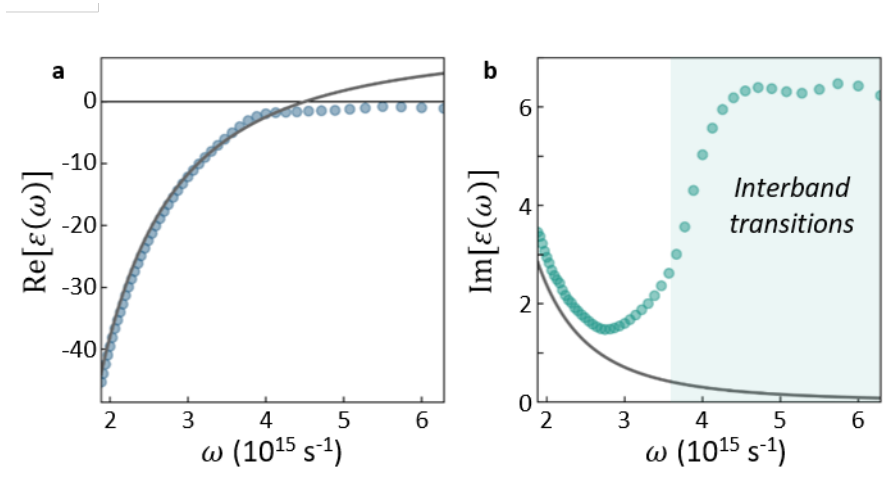


Fig. 2.1 **The Drude Model Compared to Johnson-Christy data.** **a** The real part and **b** imaginary part of the dielectric function of gold. Points show experimental data by Johnson and Christy [19] and grey lines show Drude model, calculated with parameters $\epsilon_{\infty} = 9.4$, $\omega_p = 13.8 \times 10^{15}$, $\gamma = 10^{14}$ [20]. Model shows good agreement for low frequencies, but diverges from experimental values for higher frequencies due to interband transitions (shaded region)

2.1.2 Plasmonic Confinement

An important constraint in classical optics is the diffraction limit, which states that light cannot be used to resolve features smaller than its wavelength divided by 4π .

$$\Delta x \geq \frac{\lambda}{4\pi} \quad (2.8)$$

where Δx is the feature to resolve (in one dimension). Here we will show how plasmonics breaks this diffraction limit. The confinement of light to much smaller volumes is achieved through coupling to collective oscillations of free electrons in metals, known as plasmons. Alongside *Volume Plasmons*, (not discussed here), there are two main types of localised plasmons, *Surface Plasmon Polaritons* and *Localised Surface Plasmon Polaritons*. These will be discussed in detail in the following sections.

Surface Plasmon Polaritons

Surface Plasmon Polaritons (SPPs) can be excited at the interface between two materials of differing refractive indices, such as a metal and a dielectric. SPPs were first predicted theoretically by R.Ritchie in 1957 [12] and have been extensively studied since [21]. Excited by incident light, SPPs are electromagnetic (EM) waves confined in the perpendicular

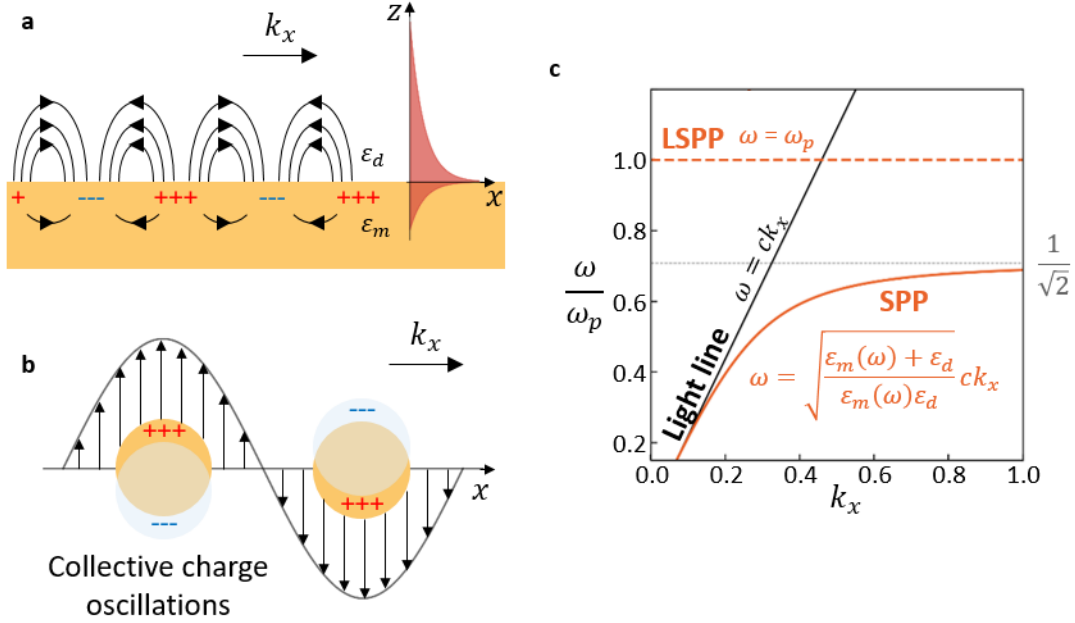


Fig. 2.2 **Surface Plasmons.** **a** Depiction of a Surface Plasmon Polariton (SPP) propagating at the metal-dielectric interface, with propagation direction labelled by k_x , and permittivity of adjacent regions marked by ϵ_d (dielectric) and ϵ_m (metal). Red curve shows the exponential decay of the evanescent field away from the interface. **b** Depiction of Localised Surface Plasmon Polariton, excited by incident EM field. Delocalised electron cloud shown by transparent blue sphere. **c** Dispersion relation for both an SPP (solid orange line) and an LSPP (dashed orange line) in comparison to the ‘light line’ (black) for photons in free space, with their corresponding equations. SPP asymptote shown in grey.

direction (z), but which can propagate in the x direction along the interface for macroscopic distances [22] (Figure 2.2a).

The dispersion relation for propagation of SPPs at an interface is given by

$$\frac{\omega^2}{c^2} = \frac{k^2}{\epsilon}, \quad (2.9)$$

where $1/\epsilon = 1/\epsilon_m(\omega) + 1/\epsilon_d$ and $\epsilon_m(\omega)$, ϵ_d are the dielectric functions of the metal and dielectric, respectively. Rearranging this for ω gives

$$\omega = \sqrt{\frac{\epsilon_m(\omega) + \epsilon_d}{\epsilon_m(\omega)\epsilon_d}} ck_x. \quad (2.10)$$

This dispersion relation (orange, solid line) is plotted in Figure 2.2c for a gold-air interface, alongside the ‘light line’ for photons in free space (black). At low frequencies SPPs behave similarly to photons with near-linear dispersion, whereas at high frequencies the dispersion relation asymptotically approaches $\omega/\omega_p = 1/\sqrt{1+\epsilon_d} = 1/\sqrt{2}$ (taking $\epsilon_d \approx 1$ for air). The SPP dispersion relation never crosses that of photons, therefore SPPs cannot be directly excited by free propagating light, instead requiring specific geometries such as a Kretschmann prism [13] to couple to incoming light.

Localised Surface Plasmon Polaritons

Localised Surface Plasmon Polaritons (LSPPs) occur when the free electrons in a sub-wavelength metal nanostructure collectively oscillate across it as a result of the incident EM field (Figure 2.2b). This collective oscillation results in a dipole, as an excess of negative charge builds up on one side of the nanostructure, leaving a positive charge on the other. In contrast to SPPs, direct excitation of LSPPs in nanostructures smaller than the wavelength of incident light is possible due to the curvature of the structures.

The dispersion relation of an LSPP is shown as a dashed line in Figure 2.2c for $\omega_p = \omega_{LSPP}$. Unlike SPPs, which display a range of frequencies, LSPPs have no dispersion in k and exist only at a well-defined singular frequency. Their dispersion relation is therefore a flat horizontal line. This line will always cross the light line at some point, demonstrating why LSPPs can be excited by freely propagating light. The resonance frequency of an LSPP is determined by a number of factors including shape, size, and material of the nanoparticle, as well as the surrounding refractive index [3, 4, 23]. This will be discussed further in the next section.

Figure 2.3a shows the LSPP field lines and resulting dipole induced across a nanoparticle. The high density of field lines at the poles leads to an increased near-field at these points, as demonstrated by the Finite-Difference Time-Domain (FDTD) simulations shown in Figure 2.3c (the slight asymmetry is a computational effect arising from the incident light direction). FDTD simulations solve Maxwell’s Equations to calculate the field intensity at each point on a grid¹. Typical field enhancements are on the order of $|E/E_0| = 10$, where E_0 is the incident field. These highly confined fields occupy volumes below the diffraction limit, therefore breaking the diffraction limit and making LSPPs a highly useful tool across many sensing fields [24].

In the quasistatic approximation (considering a particle experiencing a constant electric field at time t) the scattering and absorption cross-sections of a nanoparticle of radius r can

¹The FDTD simulations in Figure 2.3c,d were carried out by Dr Rohit Chikkaraddy, Nanophotonics Centre, Cambridge.

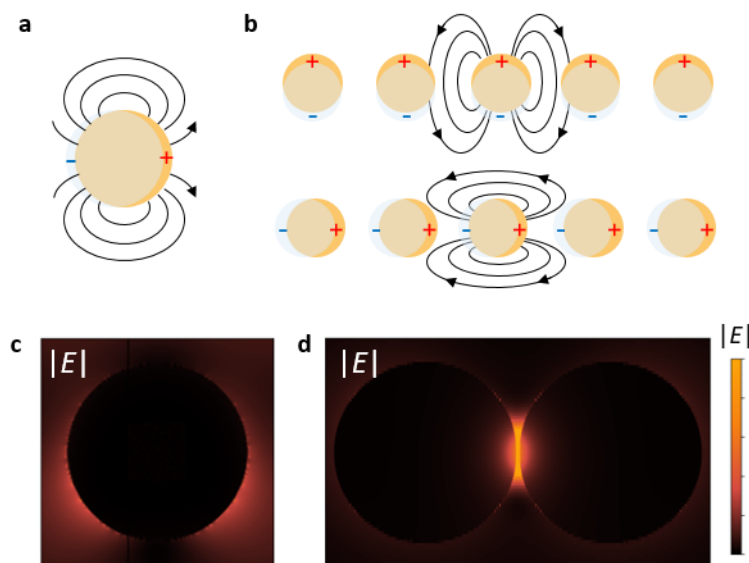


Fig. 2.3 **EM Fields Surrounding Nanoparticles.** **a** Field lines of an induced LSP on a single nanoparticle, and **b** a chain of coupled nanostructures. For the coupled chain, both perpendicular and parallel polarisations are shown. **c** FDTD simulations showing the EM field surrounding a single nanoparticle, and **d** a coupled nanoparticle-nanoparticle dimer. Nanoparticle diameter = 160 nm, gap distance = 1.5 nm.

be calculated [25, 26]:

$$\sigma_{abs} = 4\pi kr^3 \text{Im} \left[\frac{\epsilon_m(\omega) - \epsilon_d}{\epsilon_m(\omega) + 2\epsilon_d} \right] \quad (2.11)$$

$$\sigma_{scat} = \frac{8}{3} \pi k^4 r^6 \left| \frac{\epsilon_m(\omega) - \epsilon_d}{\epsilon_m(\omega) + 2\epsilon_d} \right|^2. \quad (2.12)$$

Since $\sigma_{abs} \propto r^3$ and $\sigma_{scat} \propto r^6$, for small particles absorption dominates, and for large particles it is scattering that is the dominant process. These proportionalities can be manipulated for desired use, for instance if heating effects are required, smaller particles will be utilised. However for the research carried out in this thesis it is scattering effects we wish to enhance, and so ‘large’ nanoparticles (40 – 100 nm) are used.

2.2 Coupled Nanostructures

2.2.1 Coupled Plasmons

Plasmonic coupling occurs when the near-fields of neighbouring nanoparticles interact with each other. This leads to a new set of modes as the dipoles in the two structures couple. These coupled modes lead to an even larger field enhancement than the single particle case (Figure 2.3d). This enhancement is localised in the gap between the nanoparticles, and is often referred to as a ‘hot-spot’. Field enhancements surrounding coupled nanostructures are even larger than their single counterparts and often reach values of $|E/E_0| > 100$.

The high field enhancement produced in these hot-spots can be used to enhance processes occurring in the gap region, a particularly effective technique when looking at non-linear effects such as Raman scattering. Mode volumes of coupled plasmons are typically very small; on the order of \sqrt{rd}^3 , where r is the nanoparticle radius and d the distance between nanoparticles. This enables the hot-spot to be utilised in multiple applications, in particular when pushing the detection limit to the single-molecule level [27–30].

2.2.2 Fabrication of Coupled Nanostructures

In order to make use of the high field enhancement produced in the gap between nanoparticles, coupled nanostructures must be fabricated. This next section looks at the variety of methods employed in the literature for this purpose, with focus on the nanoparticle-on-mirror (NPoM) system and long-chain aggregates, as these form the basis of the work done in this thesis.

Broadly speaking, fabrication of coupled nanostructures can be classed into one of two categories. *Top-down* techniques refer to those in which you start with a larger material and remove pieces to achieve your desired structure. In contrast *bottom-up* techniques take smaller pieces and build them up to make the final structure. Different design techniques have different benefits and pitfalls, and when choosing a coupled system and fabrication method ultimately it has to be decided which factors are more important for the experimental system. Factors to weigh under consideration include reproducibility, size and gap limitations, complexity of shape, scalability and cost, as well as many others.

A range of examples of different possible structures are shown in Figure 2.4. Figures 2.4a,b show structures produced using Electron-Beam Lithography (EBL). This involves scanning an electron beam across a sensitive resist, in order to create the desired shape. The benefits of EBL mainly come from the ability to create whatever shape is wanted (although usually in 2D), enabling focused shapes such as bow-tie antennas (Figure 2.4 b [32]) as well as many others with more complicated geometries. However the downside of top-down

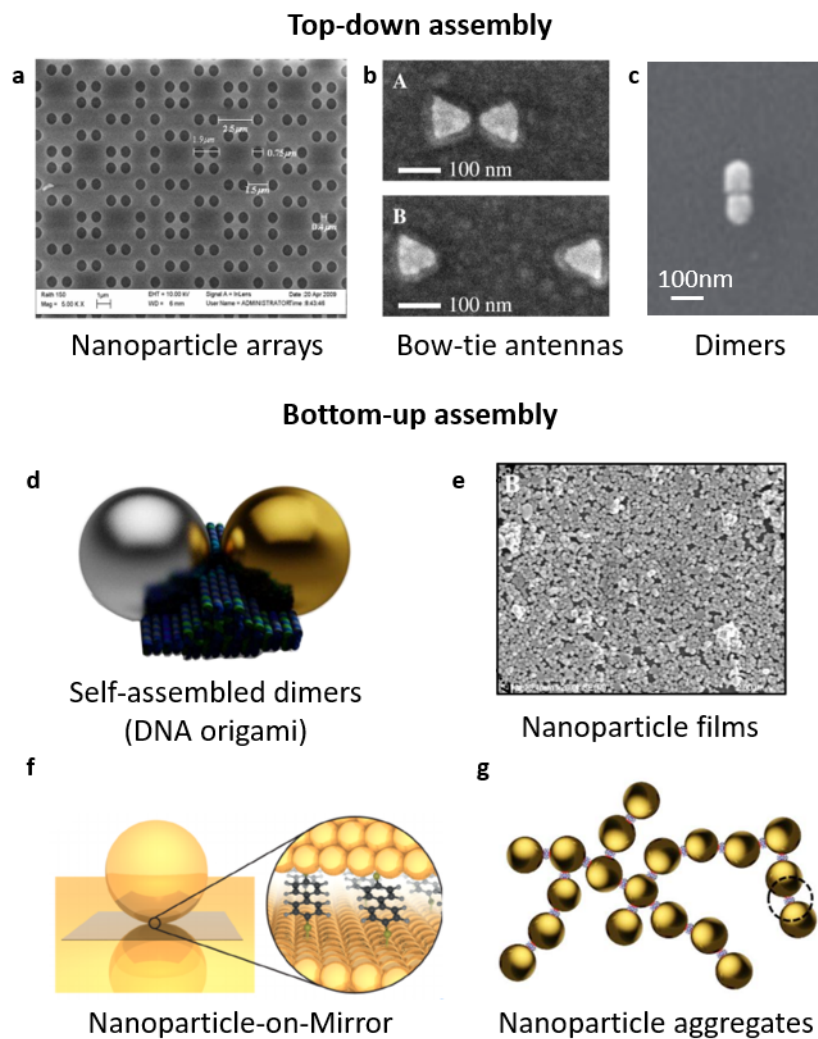


Fig. 2.4 Techniques for the Fabrication of Coupled Nanostructures. Top-down fabrication techniques include Electron-Beam Lithography (EBL) to form **a** nanoparticle arrays [31], **b** bow-tie antennas [32] and **c** dimers [33]. Example bottom-up assembly techniques including **d** self-assembly of dimers by DNA origami [34], **e** nanoparticle films [35], **f** nanoparticle-on-mirror geometry [36], **g** self-assembly of long-chain nanoparticle aggregates by organic cucurbit[n]uril molecules [37]

techniques such as EBL is that the resolution is limited by the size of the electron beam or the resist properties. This means that structures produced in this way struggle to form gap distances < 10 nm, putting a limit on the confined mode volumes and therefore field enhancement possible. The reproducibility can also be poor for structures < 100 nm due to the stability of the system in relation to the size of the structure. This can be seen in the non-straight edges and blunted tips of the bow-tie antennas in Figure 2.4b and the uneven

shapes in Figure 2.4c. Although arrays are often formed using top-down techniques, this is an expensive and time-consuming process since each structure needs to be drawn individually. As such these methods are not highly scalable.

The majority of bottom-up techniques rely on electrostatic forces and molecular bonds driving self-assembly of individual nanoparticles. Salts such as NaCl can also be used to overcome van der Waals forces and form nanoparticle films such as those seen in Figure 2.4e [35]. These films are cheap and effective, however they are highly non-uniform and the gap distance between adjacent nanoparticles is highly varied. Dimers can be formed, among other techniques, via attachment to a raft of DNA origami [34]. DNA origami uses ‘staples’ of base pairs to control the folding of the long strand DNA to the geometry of choice. In the example shown in Figure 2.4d it forms a scaffold in which the nanoparticles attach in close proximity to form a dimer.

The work described in this thesis concentrates on hotspots created by formation of nanoparticle aggregates and nanoparticle-on-mirror structures (Figure 2.4f,g). Long-chain nanoparticle aggregates can be formed under self-assembly of solution-based nanoparticles with an aggregating agent. This can be either a salt [38], used to destabilise the individual nanoparticles out of solution, or a molecular spacer [37, 39], depending on the degree of gap-distance control required. Various molecular spacers will be discussed in Section 2.4, and the field enhancements created by these aggregates as well as their plasmonic modes will be discussed in detail in Chapter 4. Another consideration to be taken into account is the number of hotspots to be probed. If the aim is to produce as high a signal as possible for whatever measurement you are taking, then structures with multiple hot-spots such as arrays, aggregates and films are ideal. If however, you wish to have a small mode volume and probe just one hotspot, for instance for single-molecule sensing [40, 41], a dimer system must be considered. In the next section the single-junction dimer-like nanoparticle-on-mirror geometry will be discussed. In this work, chain aggregates are used over films for bulk measurements due to the reproducibility of hotspot conditions across the sample. For single junction measurements, NPoM are used over dimers due to the simplicity of fabrication and the ease at which different spacer layers can be used for comparisons. Additionally the gap sizes can be made much smaller, as they are not limited by the size of the DNA strands. However, DNA has been shown to well-form dimers for plasmonic measurements, as shown in [34].

2.2.3 The Nanoparticle-on-Mirror Geometry

The nanoparticle-on-mirror (NPoM) geometry is a useful system for self-assembling a single hot-spot. It consists of a single nanoparticle spaced above a flat film, with a thin spacer layer

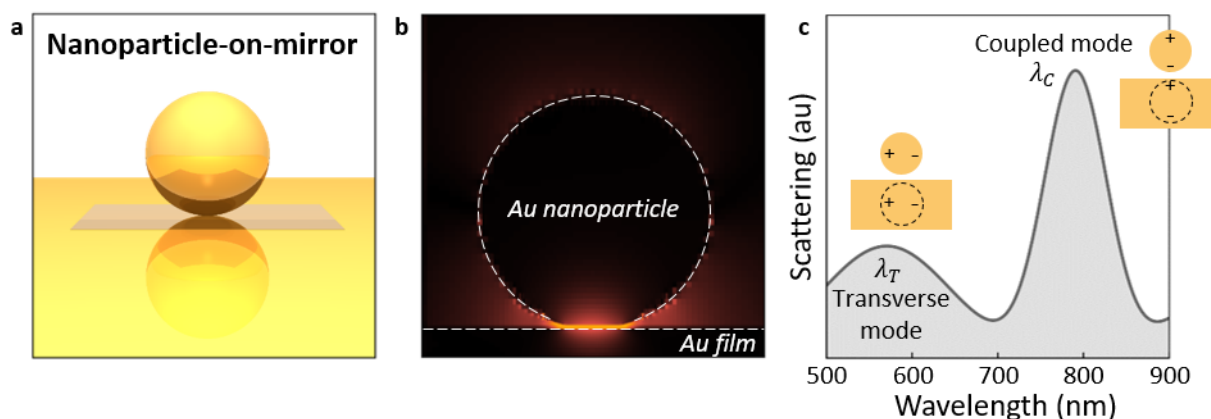


Fig. 2.5 The Nanoparticle-on-Mirror (NPoM) Geometry. **a** Illustration of a single NPoM, showing a nanoparticle spaced above a flat gold film by a thin spacer layer. **b** FDTD simulation mapping the field intensity surrounding an NPoM structure, showing the high field intensity in the gap between nanoparticle and film. **c** Representative dark-field scattering spectrum from a 80 nm gold nanoparticle with a thin molecular spacer. Transverse and coupled modes are labelled, alongside their corresponding dipole charge configurations.

preventing direct contact. The structure is self-assembled by first forming the desired spacer layer on top of the film, before drop-casting nanoparticles on top of this layer (full details in Chapter 3). For the work undertaken using NPoM in this thesis (Chapters 5-7) both the nanoparticle and film are gold, however it is entirely possible to recreate the system with other plasmonic metals such as silver, copper or platinum [42], although these are not used here due to issues with oxidation.

The NPoM structure can be thought of as a dimer-like system since the charges in the nanoparticle induce ‘mirror-charges’ in the gold film below. These then couple together, analogous to the coupling of charges in adjacent gold nanoparticles. This dimer-like coupling therefore also produces a large field enhancement in the gap region. This hot-spot of high field intensity can be seen by the FDTD simulations of the system in Figure 2.5b. This high field intensity in the gap between nanoparticle and film can be used to enhance scattering signals and other processes, with the added utility that the molecules of interest can be used as spacer materials and therefore directly placed in the gap region.

The NPoM geometry has a number of benefits. Firstly, as mentioned above it is relatively straightforward to place the molecules of interest in the gap region. Secondly, as long as the concentration of nanoparticles and deposition time is carefully controlled, millions of

near-identical systems² can be formed across a macroscopic substrate, spaced far enough apart from each other that there is no interaction between them. This makes the system highly scalable and time-efficient as well as fairly reliable. Another advantage is the tiny mode volumes it is possible to produce. The gap distance between nanoparticle and mirror is restricted only by the dimensions of the spacer layer, and so distances < 1 nm are easily and reliably formed. This corresponds to mode volumes of < 40 nm³, pushing the limits of plasmonics towards the sub-nm³ regime.

Dark-field Rayleigh scattering spectra are often used to characterise the NPoM system. An representative example can be seen in Figure 2.5c. Ignoring higher order and more complicated gap waveguide modes which arise from a flat bottom facet, there are two distinct plasmonic resonant modes: the transverse and the coupled modes. The corresponding dipole charge configurations are shown on the spectrum for each of these modes. The transverse mode, λ_T , falls in the region 500 – 600 nm. This is also known as the ‘single-particle mode’ since there is little coupling between the dipoles in the nanoparticle and mirror. The spectral position of this mode tells us about the size of the nanoparticle, but is not very sensitive to gap conditions. In contrast, the higher wavelength coupled mode (λ_C) involves a coupling of the dipole in the nanoparticle with that in the mirror, as its name suggests. The coupled mode of the system is very sensitive to the gap parameters and can vary in spectral position depending on the refractive index and size of the gap, as well as the size of the nanoparticle itself. There is a corresponding ‘dark mode’ to this coupled mode, whereby the dipole charges cancel out, but this does not emit to the far-field and so is not considered here.

As mentioned previously, the wavelength of an LSPP is extremely sensitive to its environment. In the case of a nanoparticle-on-mirror system, an analytical model can be employed to describe coupled plasmonic modes of the system, detailed in [43]. In this model the coupled plasmon has a resonance wavelength which varies depending on three variables: the size of the nanoparticle, r ; the distance between them, d ; and the refractive index of the material in the gap region, n_g . The main coupled-mode resonance wavelength, λ_C is then calculated using a gap capacitance model by:

$$\lambda_C = \lambda_p \sqrt{2\varepsilon_m + \varepsilon_\infty + 4\varepsilon_m \eta} \quad (2.13)$$

where

$$\eta = n_g^{1.14} \ln \left(1 + \frac{r}{2d} \theta^2 \right), \quad (2.14)$$

²The differences between NPoM structures measured in experiments arise mainly from the differences in starting nanoparticles, such as the various crystal geometries detailed in Section 2.2.4.

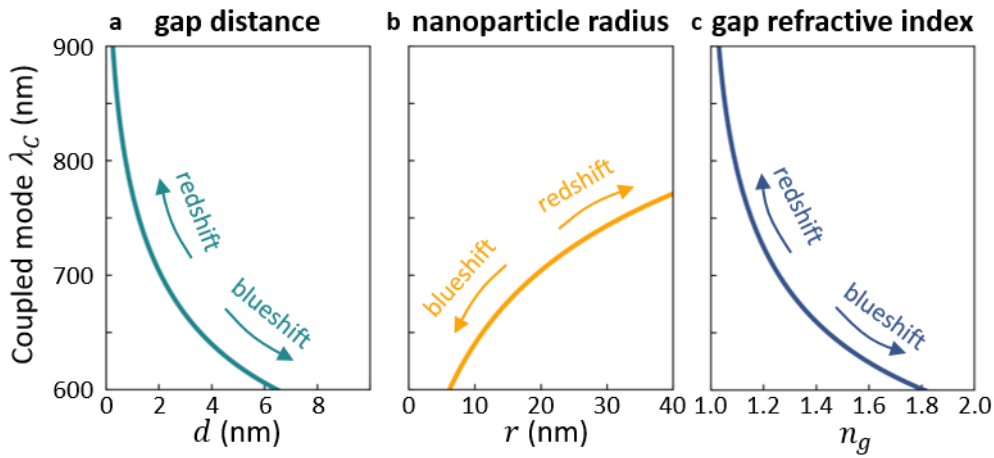


Fig. 2.6 **Analytical Model for Coupled Mode Resonance Position of a Dimer-like System.** Analytical model plotted for varying **a** gap distance d , nanoparticle radius r , and refractive index of the gap n_g . Each parameter is varied in turn, with the other two kept constant. Fixed parameters are: $n_g = 1.5$, $d = 1$ nm, $r = 40$ nm.

$\lambda_p = 2\pi c/\omega_p$ is the plasma wavelength of the nanoparticle, ϵ_m is the refractive index of the metal and θ describes the segment of the sphere influenced by the fields in the gap.

Figure 2.6 shows how varying each of these parameters in turn (for fixed values of the other two) shifts the position of the coupled resonance mode, λ_C . Decreasing the gap distance, d , between the two nanostructures leads to more efficient coupling and so can be seen to red-shift the coupled mode, (Figure 2.6a). However it should be noted that this red-shift has been shown to have a limit, as at distances $\ll 1$ nm this simplified model breaks down and blue-shifts occur due to tunnelling currents [44]. The high sensitivity of mode position to gap distance means that coupled systems can be used as so called ‘plasmonic rulers’ on the nanoscale [45].

Increasing the size of the nanoparticle will also red-shift the coupled mode position due to the higher charge on each nanostructure also leading to more efficient coupling. In contrast, increasing the refractive index of the gap medium *blue-shifts* the coupled mode as the fields in each nanostructure are more screened from each other.

Nanostructures have thus been utilised as sensors for $< 5\%$ changes in refractive index of their surroundings [23]. As well as using these changes in coupled mode spectral position to sense changes in the local environment, this can be reversed and the local environment altered to tune the plasmonic resonance to its desired position. This has been used to demonstrate strong light-matter coupling in plasmonic hotspots [46].

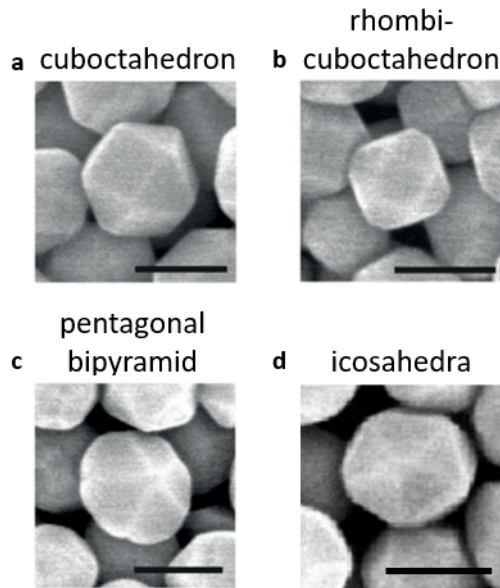


Fig. 2.7 **Geometries of Commercial ‘Spherical’ Nanoparticles.** SEM images show nanoparticles of geometries **a** cuboctahedron, **b** rhombi-cuboctahedron, **c** pentagonal bipyramid, and **d** icosahedra geometries. Scale bars are 70 nm. This figure is adapted from [47].

2.2.4 Facets on ‘Spherical’ Commercial Nanoparticles

Although the analytical model described in Equation 2.13 is useful for describing the general trends in coupled mode wavelength, it describes a fully idealised, simplified system consisting of perfectly spherical nanoparticles. It has been found experimentally that an important feature is the role of nanoparticle facets. Due to crystallinity constraints, metallic nanoparticles are in reality highly faceted [47]. The alignment and size of facets in the hotspot can affect the field enhancement as well as coupled mode resonance [48, 49].

For the experiments undertaken in this thesis, commercially produced nanoparticles from BBI Solutions were used. Although nominally spherical, it has been shown via scanning electron microscopy (SEM) images that the nanoparticles are highly faceted. Example SEM images can be seen in Figure 2.7, showing four of the most common geometries. These are labelled as cuboctahedron (a), rhombi-cuboctahedron (b), pentagonal bipyramid (c), and icosahedra (d). These geometries arise from the citrate reduction method, a widely used method for the fabrication of gold or silver nanoparticles whereby a gold salt is reduced by citrate under UV irradiation [50, 51]. It is possible to create ‘perfectly’ spherical nanoparticles, but this requires an extra etching step to remove the sharp edges [52].

Theoretical simulations have shown how the orientation of facets can drastically affect the field enhancement in the gap. The existence of an atomic-scale lightning-rod effect has

been shown theoretically by Urbietta et al. [49], who demonstrate that the field enhancement between dimers can be further enhanced at the pointed edges of nanostructures. This suggests that the non-spherical nature of nanoparticles could in fact be used to our advantage.

The nanoparticle geometries demonstrated in Figure 2.7 display a variety of facet shapes and areas; therefore, each NPoM cavity created using these nanoparticles has a different contact geometry. Polarimetry measurements by Kleemann et al. [53] suggest that it is possible to deduce the order of symmetry (and therefore infer the shape) of the gap-facing facet from the polarisation splittings observed, however it is difficult to directly confirm this without damaging the system.

These studies, as well as others [54, 55, 48] demonstrate the important role the nanoparticle geometries play, especially the shape and size of the gap-facing facet. These variables can greatly effect experimental measurements, in particular influencing the plasmonic resonances of the resulting nanoparticle-on-mirror.

2.3 Surface-Enhanced Raman Scattering

2.3.1 The Raman Scattering Process

Raman scattering was discovered in 1921 by C.V. Raman [5], as an inelastic light-scattering process to complement Lord Rayleigh's classical theory of light, which described only the elastic scattering process. Raman won the Nobel prize for his discovery in 1930 and Raman scattering went on to become one of the most widely used spectroscopic techniques, with applications in archaeology [56], medicine [57], drug detection [58] and chemical sensing [59]. Inelastic scattering processes including Raman scattering form the basis of much of this thesis.

Raman scattering investigates the vibrational energy states of a molecule, ν_m . These energy levels are quantised, meaning the resulting scattering spectrum consists of discrete lines. Figure 2.8a shows the main molecular scattering processes to be considered. The simplest form of scattering is the elastic process known as Rayleigh scattering, shown on the left-hand side of the figure. In this process the incident photon of energy $h\nu_0$ excites the molecule from the vibrational ground state (E_0) to a virtual state, so-called since the molecule spends no time in this state. The molecule then relaxes back into the initial ground state and a photon of the same energy is emitted.

In contrast, Raman scattering is an inelastic scattering process where the emitted photon has a different energy to that of the incident photon. Most commonly considered is Stokes-Raman scattering, shown in the middle panel of Figure 2.8a. In Stokes scattering the incident

photon again excites the molecule from the ground state to a virtual state, but this time it relaxes to an excited state of energy $E_0 + h\nu_m$. Energy conservation laws therefore mean give an emitted photon of energy $h\nu_0 - h\nu_m$, i.e. it has *lost* energy compared to the incident photon.

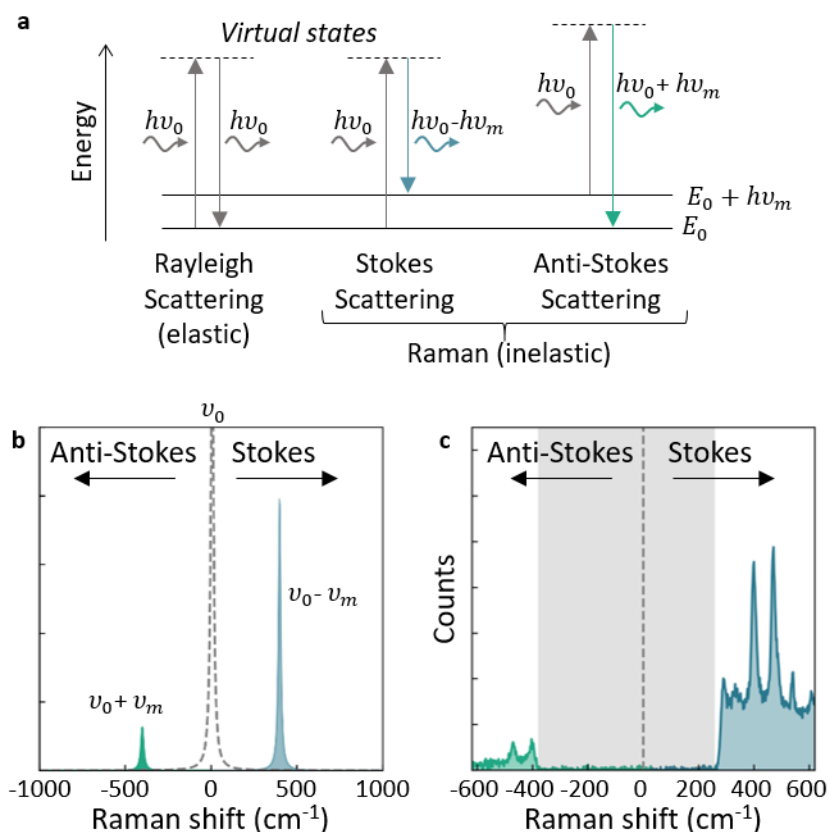


Fig. 2.8 The Raman Scattering Process. **a** Energy-level diagrams for the relevant molecular scattering processes. From left to right: Rayleigh scattering, Raman (Stokes, and anti-Stokes) scattering. **b** Corresponding energy spectrum for photons emitted in processes in (a): Rayleigh scattering (grey, dashed), Stokes scattering (blue), anti-Stokes scattering (green). **c** Experimental spectrum showing multiple molecular vibrations. Grey shaded region covers laser filter region.

The third process described here is also a form of Raman scattering, known as anti-Stokes scattering. In this process the molecule starts in an excited state of energy $E_0 + h\nu_m$. Therefore when it is excited by the incident photon it has the possibility to relax to a state of lower energy, the ground state E_0 . The emitted photon is then of higher energy than the incident photon ($h\nu_0 + h\nu_m$).

The excitation of vibrational modes via the Raman mechanism means that the difference in energy of the scattered light from the incident light corresponds to the difference in

vibrational energy levels of the molecule. A simplified energy spectrum for one vibration is shown in Figure 2.8b. These are typically plotted with an x -axis of ‘Raman shift (cm^{-1})’ calculated as $1/\lambda_0 - 1/\lambda_{\text{Raman}}$ where λ_0 is the wavelength of the incident light and λ_{Raman} the wavelength of the emitted Raman light. A molecule of interest will have multiple vibrational modes, each undergoing the Raman scattering process, and the spectrum will look more like the example in Figure 2.8c. The resulting spectrum can therefore be used to identify vibrational modes and functional groups within a molecule, building up a picture of the overall chemical structure. This is often called the ‘vibrational fingerprint’ of a molecule.

The spectral position of the Stokes light is mirrored around 0 cm^{-1} to give the anti-Stokes light. Since anti-Stokes scattering requires the molecule to already be in an excited state, the Stokes:anti-Stokes ratio can be used to measure the temperature of the molecule, assuming a Bose-Einstein distribution of energies. At room temperature Stokes scattering typically dominates, demonstrated by the higher peak intensities on the right-hand side of the spectrum. An additional feature observed is the inelastic light scattering from the electrons in the metal [60, 61], which contributes to the background signal, seen in Figure 2.8c, and discussed in Chapter 7.

Raman and Infrared Activity

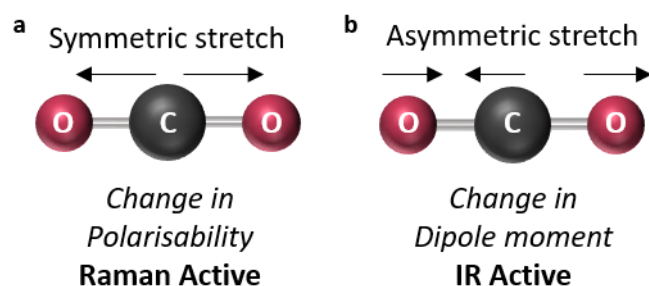


Fig. 2.9 **Raman and Infrared Activity.** Example of an **a** Raman-active (IR inactive) and a **b** IR active (Raman-inactive) mode for the simple CO₂ molecule.

The success of Raman scattering as a spectroscopic technique relies on the chemical ‘finger-print’ of each molecule being represented in the spectrum, with peaks at different spectral positions corresponding to different molecular bonds, thus enabling a picture of the molecule to be built up. However Raman spectroscopy is not a universally appropriate technique, as it in fact relies on the vibrational modes being *Raman active*. A simple CO₂ molecule, such as that shown in Figure 2.9 can be used to demonstrate what is meant by this.

For a vibration to be Raman active it must involve a change in *polarisability*. This occurs when the oscillation is *symmetric* around its equilibrium position, such as the example in Figure 2.9a. If instead the vibration involves a change in dipole moment, such as with the *asymmetric* stretch in Figure 2.9b, then its modes will then be Infrared (IR) active. Typical IR spectroscopy involves absorption of light by the IR active modes and is not a scattering process. In molecular spectroscopic theory the mutual exclusion principle states that a molecule that possesses a centre of symmetry cannot have modes that are both IR and Raman active. This is a direct consequence of the symmetry [62]. However for more complex molecules, these selection rules do not hold so completely and both conditions can be filled to a certain extent.

2.3.2 Raman Enhancement

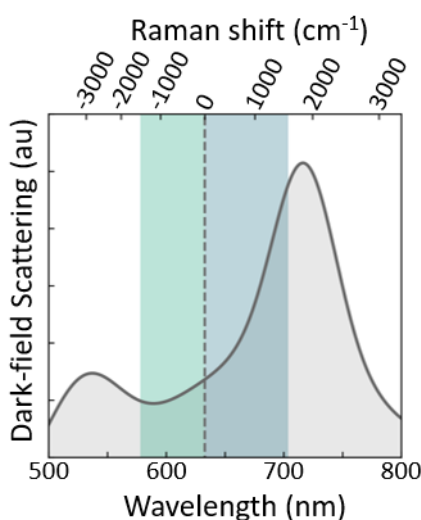


Fig. 2.10 **Raman Enhancement.** Example dark-field scattering spectrum for an 80 nm Au nanoparticle-on-mirror. Top axis shows x -axis converted to Raman shift. Overlaid is the laser wavelength used (633 nm, dashed line), and the typical region of interest for Raman scattered light (anti-Stokes: green, Stokes: blue).

The probability of an incident photon undergoing a Raman scattering event is given by the Raman cross-section, calculated as the ratio between the scattered power of Raman photons and the intensity of the incident light. The Raman cross-section is in general very small, with typical Raman cross-sections having values often $\ll 10^{-28} \text{ m}^2$. In order to improve the viability of Raman scattering in spectroscopic techniques it is often necessary to enhance it via plasmonic processes, a technique known as Surface-enhanced Raman Scattering (SERS).

Plasmonic fields can be used to greatly enhance scattering processes such as Raman scattering, as they augment both the incoming and outgoing light, leading to an enhancement proportional to the 4th power of the light intensity:

$$Enhancement_{SERS} \propto I_{inc} \times I_{Raman} \propto E_{inc}^2 \times E_{Raman}^2 \approx E_{inc}^4 \quad (2.15)$$

Where $I_{inc,Raman}$ are the intensities of the incoming and Raman scattered light fields respectively, and $E_{inc,Raman}$ are the corresponding field strengths. This can lead to SERS enhancement factors of up to 10^{10} , however in practice enhancement factors are a couple of orders of magnitude lower.

For the plasmonic coupled systems studied in this thesis, the E-field enhancement varies at different wavelengths across the visible spectrum due to the different modes excited within the system. To demonstrate this, a typical NPoM scattering spectrum is shown in Figure 2.10, a close representation of the near-field experienced by molecules of interest in the gap region³. Here the dashed line shows the spectral position of the ingoing laser and the shaded area shows the spectral region over which Raman scattered light is measured (green shows anti-Stokes region, blue show Stokes region). It can be clearly seen that different field strengths are experienced and that the choice of laser wavelength alongside tuning of plasmonic resonances (as shown in Figure 2.6) is important to ensure the incoming and scattered light are emitted close to the plasmon resonance⁴.

2.3.3 Picocavities and the Optomechanical Description of SERS

For extremely high field enhancements, the interaction of Raman vibrational modes of a molecule with the plasmonic cavity can also be thought of in terms of an optomechanical model, as detailed in the full quantum-mechanical picture of the Raman process by Schmidt et al. [64] and Roelli et al. [65]. The full theoretical description is outside the scope of this thesis, but the system can be pictured by imagining a typical Fabry-Perot cavity of two mirrors, with one mirror coupled to a mechanical oscillator (Figure 2.11a). In this picture the laser drives the light into the cavity. The radiation pressure of the photons causes a movement in the mechanical oscillator, which therefore alters the distance between the two mirrors. In our SERS picture the radiation pressure from an intensely confined plasmon acts as the back-action to change the polarisability of the mode.

³Lombardi et al. [63] have shown that in fact there is a small spectral blueshift between near- and far-fields, but this effect is minimal for the work considered here.

⁴Although there is a difference in field enhancement between the incoming laser and outgoing Raman light, the percentage difference is still small and Equation 2.15 still holds.

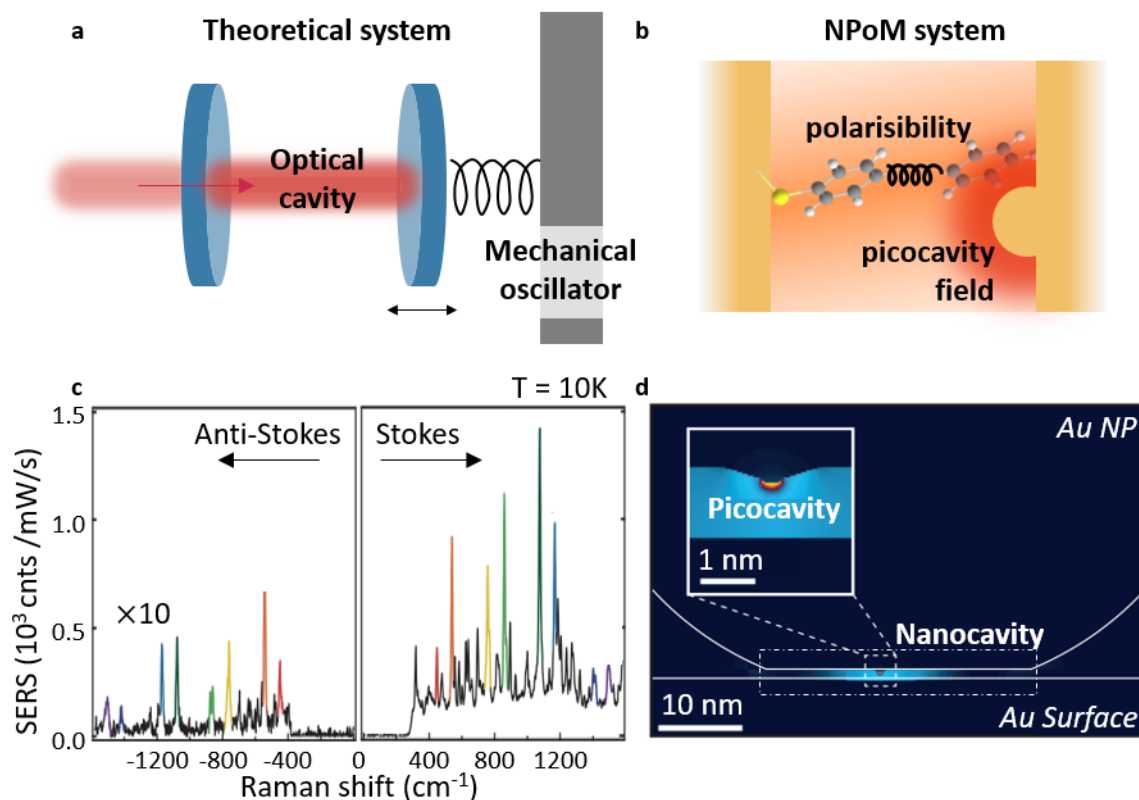


Fig. 2.11 **Optomechanical Descriptions of SERS Emitted from Picocavities.** **a** Analogy to optomechanical system: two mirrors form a Fabry-Perot cavity, with one mirror attached to a mechanical oscillator and the other fixed. Photons from an incoming laser produce the radiation pressure to move the mirror and drive an oscillation. **b** Illustration of optomechanics in a NPoM system. Picocavity adatom results in high field enhancement and resulting high radiation pressure. This acts as back-action to change the polarisability of the molecule in the gap. **c** Experimental SERS spectra taken at 10 K showing additional spectral features on both the Stokes and anti-Stokes sides, evidencing the existence of picocavities. **d** Simulation of near-field in gap region of a NPoM containing a picocavity. The overall nanocavity hot-spot is marked. Inset shows zoomed-in region of picocavity formed by an adatom, with even higher field intensity. a,b are adapted from [18].

The optomechanical process can act to amplify the mechanical oscillator. This optomechanical coupling of the vibrational mode to the plasmonic cavity leads to an amplification of the population in the excited state; a process called *vibrational pumping*. In 2016 Benz et al [18] showed experimental results demonstrating this theory of optomechanical coupling in practice. It was shown that an atomic-scale lightning-rod effect could be realised by spontaneously forming a single gold adatom on the bottom surface of a gold nanoparticle in NPoM configuration under irradiation with a laser (see Figure 2.11b,d). These ‘picocavities’

produce the extremely high field enhancements required to vibrationally pump the system. The back action exerted on the cavity is the change in polarisability of the vibrational mode. A more intuitive way of thinking of this is to consider that the size of the adatom-formed picocavity (with respect to a single molecule in its hotspot) means that the molecule will now feel a field gradient across it. This alters the selection rules and transforms IR modes, which were previously Raman-inactive, to now be visible in the Raman spectra. These additional modes are highlighted in colour in Figure 2.11c, and hereafter termed ‘picocavity lines’ to distinguish from the standard SERS spectral lines usually seen (termed ‘nanocavity lines’).

Alongside the additional lines observed in the spectra, another consequence of this vibrational pumping is the additional population in the vibrationally excited state. As mentioned in Section 2.3.1, the population of the excited state is directly linked to the amount of anti-Stokes scattering observed. As these experiments were carried out at 10 K the thermal population of the excited state is expected to be negligible. However anti-Stokes counterparts of the picocavity lines can clearly be seen in the left-hand panel of Figure 2.11b, showing that the optomechanical pumping is occurring. It should be noted that nanocavity lines from the surrounding nanocavity hot-spot are not present in the anti-Stokes spectrum, as the field confinement away from the picocavity is not high enough to enable this pumping.

Other Observed Spectral Features

As well as the additional sharp peaks observed when a picocavity is formed, there are additional anomalous spectral features sometimes observed which can give clues to processes happening on the nanoscale. Broad background increases occurring on a very short timescale have been observed a number of times in the literature [27–30, 66]. Weiss et al. [30] attribute their observations of this to motion of the adsorbed molecule on the surface, triggered by photodesorption events that are mediated by electron tunnelling between the molecule and surface. Cheng et al. [66] instead attribute the increased background they observe to an induced field of the molecules, which increased the local field felt by the surrounding nanostructures. However the systems used in these experiments were quite different to those used in this thesis, with Weiss et al. utilising dye molecules alongside nano-crystals and Cheng et al. using a large aggregate of nano-flowers. Both of these lead to additional contributions and instabilities to the systems, making it harder to isolate the background increases. In Chapters 6 and 7 I will discuss these observations further.

2.4 Spacers for Coupled Plasmonic Systems

For most bottom-up techniques for forming gap plasmons involving self-assembly, a spacer material is required. This has multiple uses. Firstly, it is necessary to prevent direct contact between the two nanostructures, as previously discussed. Secondly, the spacers themselves can be used as aggregating agents to bring the two objects of interest together. A careful choice of spacer can be utilised in order to achieve the best gap parameters and conditions needed for the relevant experiment. Although (as mentioned in Section 2.2.2) salts can be used to aggregate nanoparticles, this leads to non-uniform gap distances and hard to control geometries with many overlapping spectral resonances. In the work detailed in this thesis, we will focus on more controllable systems such as molecular spacers and other materials.

2.4.1 Cucurbit[n]urils

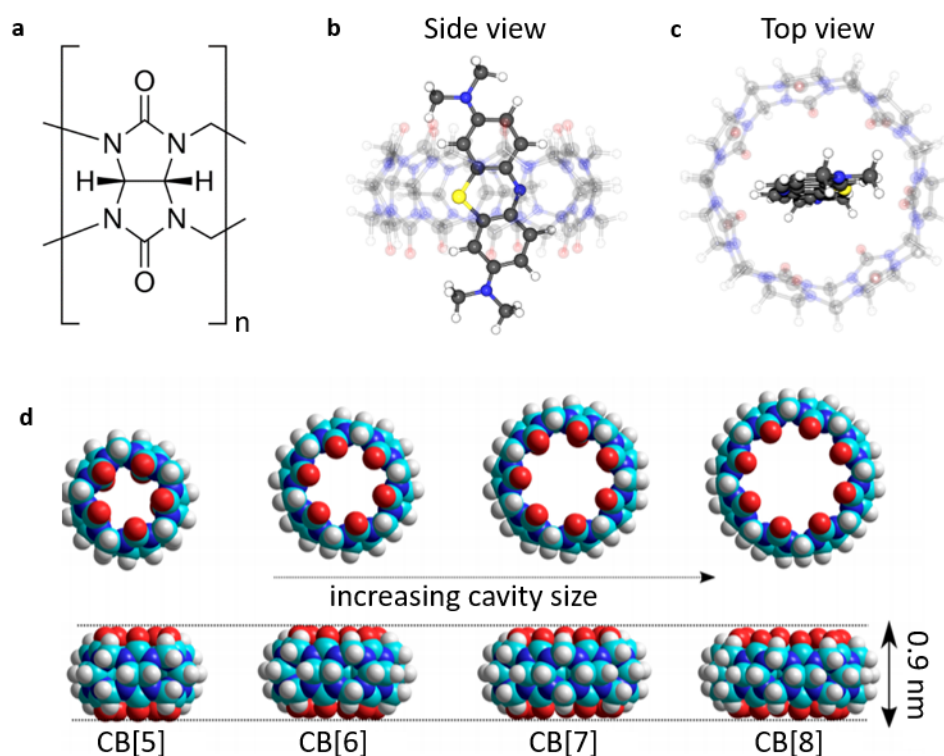


Fig. 2.12 **Cucurbit[n]urils.** **a** Single repeating unit which makes up all CB[n] molecules [67]. **b** Side and **c** Top view of an analyte molecule (here methylene blue) encapsulated inside a CB[7] molecule. **d** Top and side views of CB[5-8] molecules, showing the increasing portal size but constant height. Adapted from [68].

One useful group of molecular spacers used in forming both nanoparticle aggregates and NPoM structures are cucurbit[n]urils (CB[n]s). These are a series of rigid, barrel-shaped molecules with hydrophobic cavities and hydrophilic carbonyl portals that bind strongly to gold [68, 39], functionalising them as ideal candidates for molecular spacers. The n -number corresponds to the number of units from Figure 2.12a that make up the molecule. This affects the lateral width but the height remains identical (Figure 2.12d), meaning the portal size can be changed without changing the gap distance, therefore ensuring the plasmonic mode position is kept constant. The barrel-shaped geometry of the molecules gives them the unique ability to encapsulate analyte molecules of interest, with different numbers of host molecules trapped in the centre depending on the size of CB[n] chosen. The dual function of CB[n] as a spacer molecule and an analyte host leads to a system whereby the analyte molecule is placed exactly in the centre of the plasmonic hotspot, rendering it extremely useful for sensing techniques such as SERS.

The suitability of CB[n]s as both a nanoparticle spacer and a host cavity for analytes of choice has been shown in [69]. Here the authors demonstrate how CB[n]s can be used as a ‘glue’ in nanoparticle aggregates, leading to a robust system for SERS sensing. It is also shown how the CB[n] molecules themselves can directly report the near-field intensity in the gap, via measurement of their own SERS signals.

2.4.2 Self-Assembled Monolayers

As the name suggests, self-assembled monolayers (SAMs) are made up of organic molecules which form highly ordered super-structures through self-assembly. This ordered, strong monolayer lends itself well to NPoM structures. A SAM can be formed on the underlying gold mirror, before depositing a nanoparticle on top to easily form the desired structure. Most molecules that form SAMs have a ‘head’ group, which has an affinity for the surface, and a tail which subsequently stacks together with adjacent molecules. The most stable SAMs have strong interactions between the head group and the metal surface to which they attach. To this end, ideal molecules commonly have head groups which consist of thiols, amines, and silanes.

Interactions between adjacent molecules are central to forming SAMs with high stability and reproducibility. Because of this, a large fraction of SAMs have tail groups which include phenyl rings, such as the example shown in Figure 2.13. When two phenyl rings are in close proximity, the delocalised electrons in their π -orbitals overlap. This is known as π – π stacking and leads to a strong quasi-bonding interaction between the two molecules. The π – π stacking affects the tilt angle, α , of the molecules in the SAM, a value which is usually in the region of 10–30°. The high density of delocalised electrons in the rings

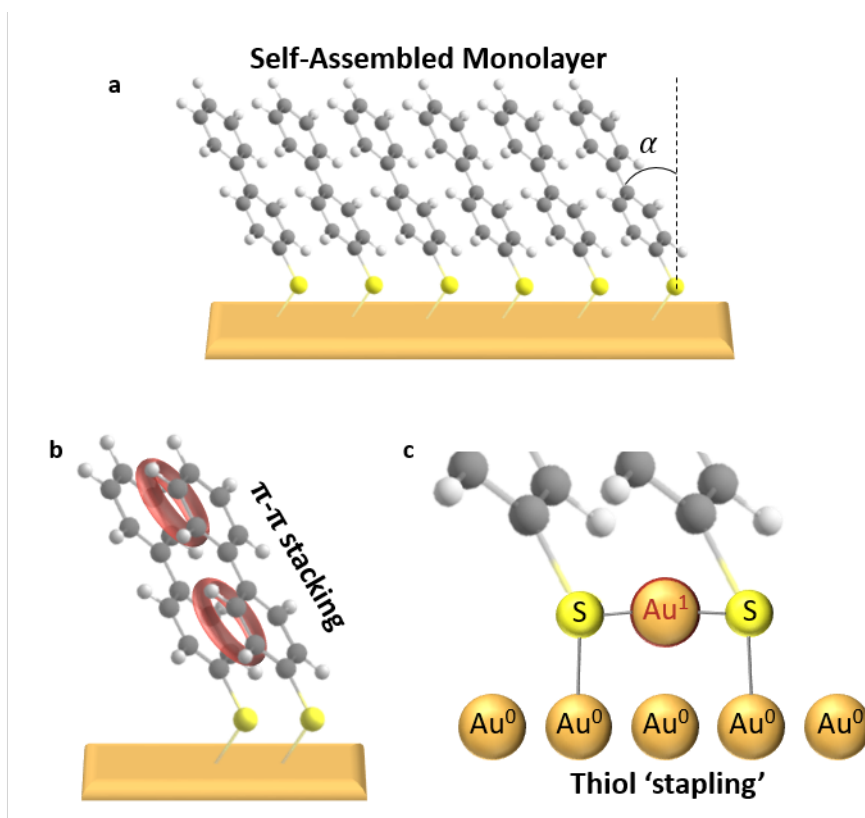


Fig. 2.13 **Self-Assembled Monolayers.** **a** Schematic of a biphenyl-4-thiol (BPT) self-assembled monolayer. α is tilt angle. **b** Depiction of $\pi - \pi$ stacking between phenyl rings of adjacent BPT molecules. **c** Representation of the thiol stapling structure, formed when thiol bonds attach to a gold surface (adapted from [70]).

mean these sorts of molecules are highly polarisable and therefore highly Raman active (see Section 2.3.1). Another useful consequence of using molecules that undergo $\pi - \pi$ stacking is that the resulting SAMs have a very high packing density. This means impurities such as water molecules and other ions are excluded from the gap region. Self-assembled monolayers are not perfectly consistent across the entire sample surface, but instead form domains of consistent molecular orientation with grain boundaries separating adjacent domains. However, the high packing density resulting from molecules with $\pi - \pi$ stacking ensures the domains are large in these cases.

To form SAMs on gold surfaces, molecules with thiol head groups ($R - \text{SH}$) are often utilised as these form strong bonds to the gold. For years it was thought that the sulphur atom simply formed covalent bonds with two Au atoms from the gold surface. However it is now widely accepted that thiol 'stapling' occurs along the surface [71]. This is the name given to the configuration formed when an Au atom is 'plucked' from the metallic surface, as illustrated in Figure 2.13c. It is suggested that this effect or similar could potentially be

a factor in what is driving experimental results of picocavity adatoms to extrude from the metal surface, but this is not yet understood.

2.4.3 Other Spacer Materials

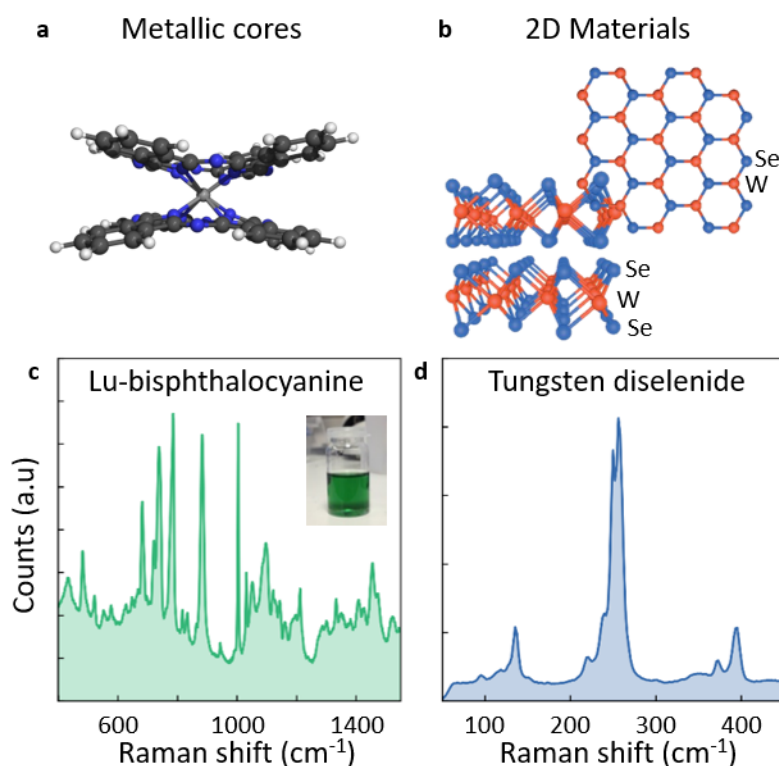


Fig. 2.14 **Other Nanoparticle Spacers.** **a** Molecular structure and **c** corresponding SERS spectrum of Lu-bisphthalocyanine. Inset shows green colour of molecule in solution, showing its absorption. **b** 3D Molecular structure [72] and **d** SERS spectrum of tungsten diselenide, an example of a 2D material that can be used in plasmonic systems.

Although not used in the core research of this thesis, I will briefly touch on other classes of spacers and what this means for their Raman signatures.

Organic spacers that incorporate metallic cores, such as bisphthalocyanines, can be synthesised for use as nanoparticle spacers in aggregates or NPoM structures [73]. This introduces questions on how addition of an electronically-active molecules can affect the plasmonic hotspot. The phthalocyanine rings have high absorption at 600-700 nm, demonstrated by the green colour of the liquid (Figure 2.14c, inset). Therefore they can undergo surface-enhanced resonant Raman scattering (SERRS), a process which will further enhance SERS signals.

2D materials can be used as ‘hard’ spacers in plasmonic NPoM systems. This introduces the opportunity to observe strong coupling [46], as well as to use surface-enhanced Raman spectroscopies to observe defects [74]. It is also interesting to note that 2D materials often have lower Raman shift (lower energy) vibrational modes, as shown in Figure 2.14d. This can be difficult to measure experimentally due to the limited availability of narrow-band laser filters, but opens up the possibility for interesting physics, as the van der Waals forces between layers can be measured, as well as defects and interlayer coupling.

2.5 Grain Boundaries in Metals

As well as nanoparticles not being fully symmetrical (as detailed in Section 2.2.4), we will also have to consider crystalline defects in the metal nanoparticle and film. The nanoparticles used in this thesis are often made up of multiple crystal domains. At the intersection between two crystal planes there can be a 2D or 3D defect plane, known as a grain boundary. Although well studied using electron microscopy methods [75, 76], and shown to occur in nanoparticles (Figure 2.15d) grain boundaries have not yet been studied in the context of effects on the plasmonic resonance.

There are a number of different types of grain boundary, with the most simplistic categorisations shown in Figure 2.15a-c [77]. The main distinction highlighted here is between low-angle and high-angle grain boundaries. Here we consider only lattice planes in 2D. At a grain boundary the lattice planes are offset to each other by a certain angle. If this angle is $< 15^\circ$ it is classed as a low-angle boundary, whereas if the angle is $> 15^\circ$ it is instead classed as a high-angle grain boundary. It has been reported by Alekseeva et al. [75] that in nanoparticles of diameter ~ 100 nm, high angles outnumber low angles by 100 : 1, however the nanoparticles studied there were palladium rather than gold, and formed via hole-mask colloidal lithography.

The amount of disorder and reduction in number density of metallic atoms depends on the angle between lattice planes. Twinning plane defects, such as that shown in Figure 2.15c, are a special case in that the adjoining planes are exactly mirrored, so the crystal pattern continues and there is no reduction in number density.

Theoretical models look at the effect of varying this angle, known as the misorientation angle. In the example in Figure 2.15e the energy of the grain boundary has a maximum at 45° . 0° is the initial position with no misalignment and for this particular lattice there is a 90° rotational symmetry, resulting in a twinning plane and subsequent energy minima at these points.

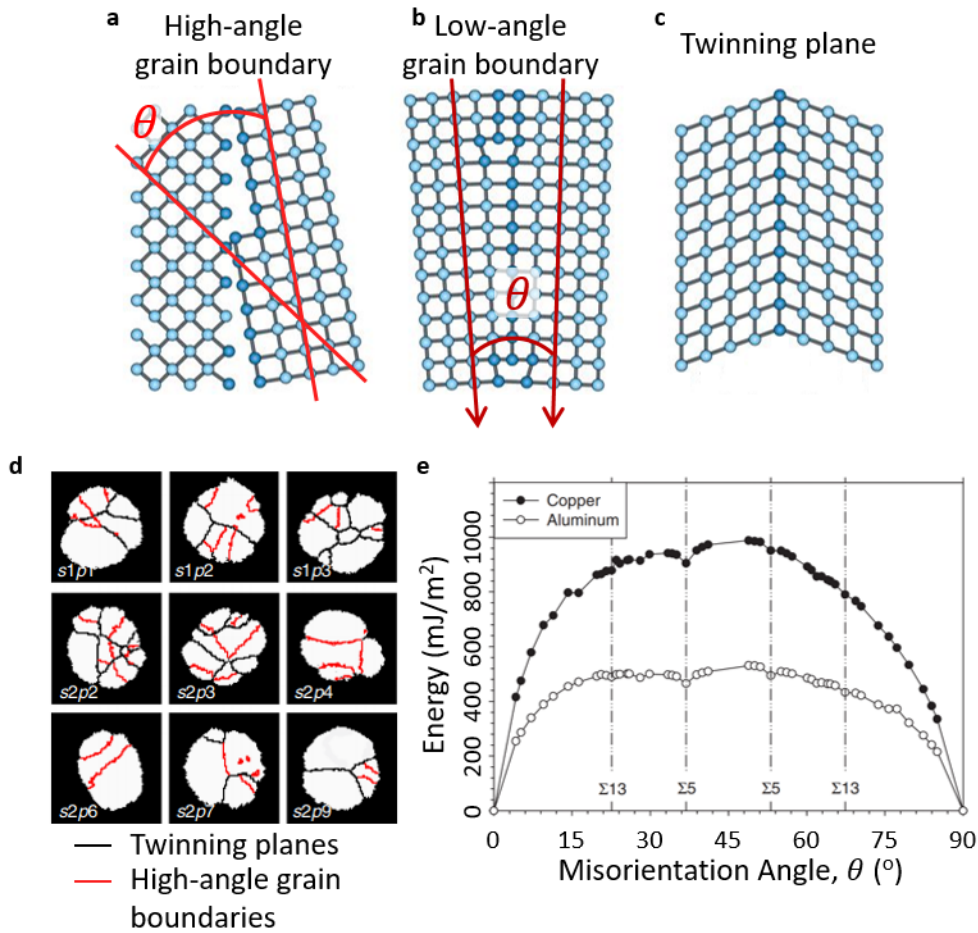


Fig. 2.15 **Grain Boundaries in Metallic Nanoparticles.** 2D depiction of **a** high-angle, **b** low-angle and **c** twin-plane grain boundaries [77]. θ is the misorientation angle. **d** Data from Alekseeva et al. [75] showing the various grain boundaries measured in 100 nm Pd nanoparticles. **e** Simulations from Tschopp et al. [78] showing an example of the variation in grain-boundary energy with misorientation angle, θ .

When considering grain boundaries in the context of plasmonics, consideration of the exact lattice structure of the grain boundary can be neglected, and the boundary considered only by its effect on the local plasma frequency, ω_p . This was defined in Section 2.1.1 as

$$\omega_p^2 = \frac{ne^2}{\epsilon_0 m^*}. \quad (2.16)$$

Since the local number density is altered at a high- or low-angle grain boundary, it is clear the local plasma frequency will also be affected. Although across a twinning plane there is no change in number density (by definition), the bandstructure is altered, which alters

the effective mass term, m^* [79], and therefore the plasma frequency also changes in this situation. The effect this change in plasma frequency has on the plasmonic resonance modes of a nanoparticle will be considered in more detail in Chapters 6 & 7.

Chapter 3

Experimental Details

3.1 Spectroscopic Techniques

In this section the experimental details of work carried out in this thesis will be described. The first part of this chapter details the spectroscopic techniques used, in particular dark-field and surface-enhanced Raman spectroscopy, alongside the microscope set-up and particle-tracking software used to integrate the two techniques. This includes a summary of the auto-detection methods developed to deal with the large datasets of several million spectra produced and pick out both broad-band emission and extra picocavity lines from kinetic SERS spectra. The second part gives a brief introduction to some of the theoretical simulations used to compare to experimental results, namely Finite-Difference Time-Domain (FDTD) and Boundary Element Method (BEM). The third part of this chapter gives details for the experimental protocol developed in sample fabrication of nanoparticle-on-mirror and nanoparticle aggregates.

3.1.1 Dark-Field Spectroscopy

Dark-field (DF) scattering is used repeatedly throughout this thesis to ascertain the resonant plasmonic modes of the cavity, and is therefore a very useful way to characterise the system. Dark-field scattering differs from standard bright-field (BF) scattering spectroscopy, as only the Rayleigh scattered light is collected, with reflected light blocked. This is done by using a beam block in conjunction with a circular mirror to ensure that only a ring of light is incident on the back-aperture of the objective, creating high-angle illumination. The light scattered from the nanostructure is then collected from the remaining area (as demonstrated in Figure 3.1a,b). The angle of incident and collected light is set by the numerical aperture (NA) of the objective. The light source (bulb: Phillips 7023) is incoherent and broad-band, covering

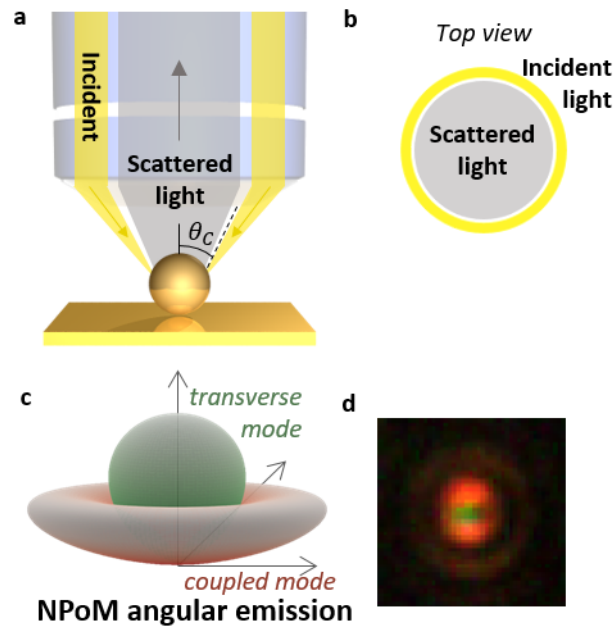


Fig. 3.1 **Dark-Field Spectroscopy.** **a** Schematic of the incident (shaded yellow) and collected scattered light (shaded grey) in dark-field configuration. Light is incident at high angle (θ_C) and is collected at all angles below this, with an angle set by the numerical aperture of the objective. **b** Top view of (a), showing the incident and collected light on the back-aperture of the objective. **c** The simulated angular emission of the coupled mode (red) and transverse mode (green) from an NPoM structure. Adapted from [80]. **d** The characteristic real-space image of a NPoM viewed under dark-field illumination, showing the coupled mode as a red ring surrounding the green transverse mode.

the visible spectral range, therefore throughout this thesis it will be termed a ‘white-light’ (WL) source.

A Lumenera Infinity 3 camera is used to view the nanostructures in real time¹ and an Ocean Optics Seabreeze spectrometer is used to collect spectra of the scattered light. The angular scattering profile of a typical NPoM structure is shown in Figure 3.1c. It can be seen from this that the coupled mode (red) scatters at high angles and the transverse mode (green) scatters directly upwards. Therefore when an NPoM structure is viewed through the Infinity camera in a dark-field configuration it is easily recognisable as a red ring surrounding a green dot (Figure 3.1d). The high angle of emission of the coupled mode means objectives with high numerical aperture (NA) are needed, with achromaticity as far into the near-infrared as possible. For the measurements here, an Olympus 0.8 NA long working-distance objective is used.

¹The IR filter is removed from the camera in order to maximise visibility of NPoM coupled modes.

3.1.2 Integrating Dark-Field with Surface-Enhanced Raman Spectroscopy

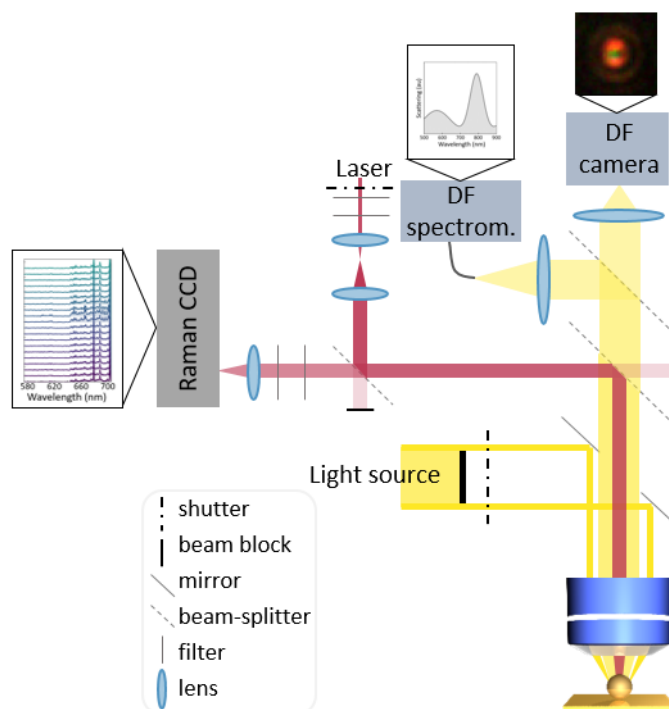


Fig. 3.2 **Integrated Raman and Dark-Field Spectroscopy.** Simplified optical diagram of custom-built integrated Raman and dark-field set-up.

For the experiments undertaken in this thesis, two Raman set-ups are used. For the experiments involving nanoparticle aggregates (Chapter 4), a commercial Raman microscope is used (Renishaw inVia Raman spectrometer). For the experiments involving NPoM structures, a custom-built integrated dark-field and Raman microscope is used.

The commercial Renishaw Raman microscope has both a 633 nm HeNe laser and a 785 nm diode laser, with a flipper mirror to move between the two. Both lasers are utilised in confocal mode, and power is controlled by a set of neutral density filters to give an input power of up to $650 \mu\text{W}/\mu\text{m}^2$ giving an equal power on sample for both laser wavelengths. The grating is 1200 lines/mm. The stage is computer controlled via Renishaw software, and can be rastered across a specified region to create a map of Raman signal.

The custom-built microscope integrates an Olympus BX51 dark-field microscope (described in Section 3.1.1) with a 633 nm HeNe laser and Andor Shamrock i303 spectrograph and Andor Newton EMCCD, cooled to -90°C . The grating used is 600 lines/mm. The set-up can be seen in Figure 3.2. A beamsplitter is used to couple the laser and white-light into the same beam path, with a white-light shutter utilised to block white-light while Raman measurements are being taken. The scattered white-light is directed partly to the dark-field

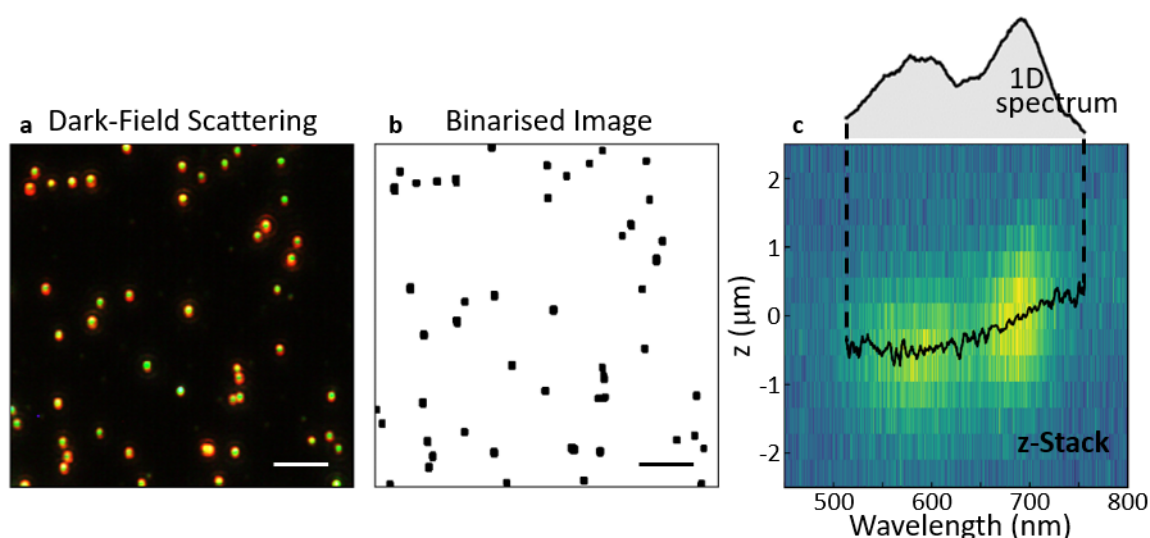


Fig. 3.3 Dark-Field Images and Spectra. **a** Example of single field of view of multiple NPoM structures viewed in a dark-field configuration. Scale bar is $10\ \mu\text{m}$. **b** Binarised version of (a), showing black at the points in which NPoM are detected. **c** Example z-stack of dark-field spectra collected for different heights on a single NPoM structure, demonstrating the chromatic aberration. Black line shows focus height for each wavelength, used to create the aberration-corrected 1D spectrum (top).

spectrometer (cooled to $-22\ ^\circ\text{C}$) for spectral information and partly to the dark-field camera for real-time observation of the position on the sample. Reference and background measurements are required to remove spectral features of the white-light source and are taken using a diffuse scatterer.

The laser first passes through a laser shutter and is then spectrally filtered using a clean-up filter, before passing through an adjustable set of neutral density (ND) filters used to vary the power on the sample. Maximum laser power on the sample is $709\ \mu\text{W}/\mu\text{m}^2$. Scattered Raman light from the nanostructures is directed to the Andor Shamrock and Newton CCD. The elastically scattered laser light is removed using two notch filters. The spectrometer disperses the light spectrally in order to be recorded by the CCD. The sample is placed on a fine-movement xyz stage. The stage, white-light shutter, laser shutter and cameras are all computer controlled. This enables experiments to be automated, as will be discussed in the next section.

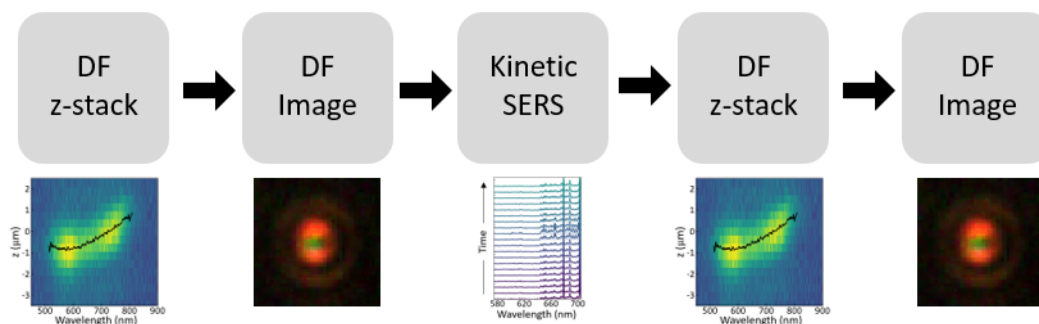


Fig. 3.4 **Automated Experimental Protocol.** Flow-chart showing order of measurements for each NPoM structure detected

Automated Particle Tracking

The time-dependent experiments described in Chapters 4-7 make use of particle-tracking software developed by Dr Richard Bowman and William M Deacon². This code has its basis in a function called ‘CameraWithLocation’, which essentially calibrates the image from the dark-field camera with movements of the stage, meaning that any point visible on the sample can be moved to via computer control of the stage. This is used in conjunction with a binarisation of the image (as shown in Figure 3.3a,b) to automatically move to every position deemed to be a NPoM structure. Multiple tiles of view can be stitched together to measure thousands of nanoparticle structures in a single experiment. Once an NPoM is located, a z -scan of dark-field spectra is taken over a range of objective lens heights. This can additionally be used to auto-focus the stage to correct for any slight drift over time.

To collect time-dependent information on various NPoM structures, I then integrated collection of kinetic SERS spectra with this software. A flow chart of the experimental protocol followed when each NPoM structure is identified is shown in Figure 3.4. First of all a z -stack, such as that shown in Figure 3.3c, is taken. As well as focusing the sample, it is used to correct for chromatic aberration arising from the objective used. This is the name given to the effect in which different wavelengths in the spectrum have different focal heights. An aberration-corrected 1D spectrum pulling together the maximal signal for each wavelength can then be extracted from this z -stack (Figure 3.3c, top). The point at which each wavelength value is taken is indicated by the black line.

A dark-field image of the nanostructure is then taken on the dark-field camera. This can be used to refer back to, and ensures there are no other nanoparticles or debris in too close proximity.

²Nanophotonics Centre, Cambridge, UK. This software is open source and can be found at: <https://github.com/nanophotonics/nplab>

The kinetic SERS spectrum is then taken of 1000 SERS spectra in quick succession. In order to measure high-speed dynamics, the CCD is set to read out in full vertical binning mode in conjunction with a 50 kHz readout rate. This allows us to decrease the integration time to 0.01 s with a 0.003 s dead time between spectra. The CCD has the capability to increase the readout rate to 3 MHz, which would decrease the deadtime even further. However this also drastically reduces the signal-to-noise, to a point where the low integration time cannot be used, as no discernible signal is visible above the noise. Therefore a readout rate of 50 kHz is a good compromise, enabling high enough signal-to-noise without a too significant percentage dead time.

After collection of the kinetic SERS spectrum, a second set of dark-field spectra and images is taken. This enables us to measure how the NPoM system might have structurally changed under laser irradiation.

3.2 Auto-Detection Methods

Although mostly temporally consistent, the kinetic SERS spectra from nanoparticle-on-mirror structures contain occasional anomalous spectral features, which will be discussed in detail in Chapters 5-7. In order to analyse large datasets of millions of spectra from thousands of NPoM structures it is necessary to develop techniques for auto-detection of such features for further analysis. The spectral features requiring auto-detection both show large increases in light emission, but are very different in spectral shape. Picocavity spectra, which will be discussed in Chapter 5, show unchanging BPT SERS lines, with additional sharp spectral lines appearing in between, as well as peaks on the anti-Stokes (left) side of the spectra. They typically last for between 3-10 spectra, but can transiently change within this time, as shown in Figure 3.5b. In comparison, flare spectra show broad-band Gaussian line-shapes, reaching across both the Stokes (right) and anti-Stokes (left) side of the spectra (Figure 3.5b), on top of which the original SERS peaks can be seen. These events are much more fleeting, often lasting for only the course of one spectrum. They will be discussed in Chapters 6 & 7.

Although very different in appearance, the common feature of intensity increase means that there are subtle difficulties in detecting each effect separately. The full details of the developed code are not described here, but in essence the flare events can be detected simply by integrating across all wavelengths and thresholding the subsequent values. Since the summed counts are always higher for flares than for picocavities, this is relatively straightforward. A binary value is then assigned to each spectrum, denoting whether it contains a flare event or not. This is shown by the grey bar in the right-hand panel of Figure 3.5a.

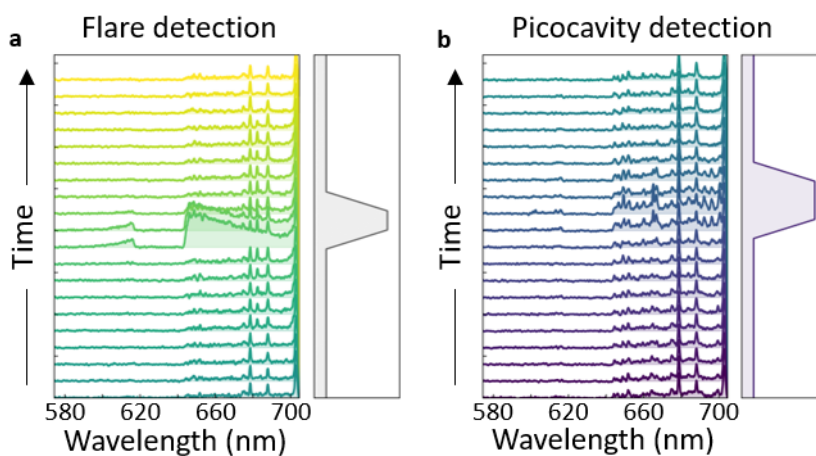


Fig. 3.5 **Auto-Detection Methods.** Example kinetic spectra sample showing **a** Flare event, and **b** Picocavity event. Right-hand panels show binary labelling giving time-stamps of events.

In comparison, picocavity events cannot be detected with thresholding since the additional counts observed are not larger than the variation between NPoMs in BPT SERS signal intensity. Instead the spectra are differentiated with respect to wavelength, in order to smooth out any flare events. Next peak-finding algorithms are run, and any spectra showing more than three large peaks highlighted as a picocavity event. In this way a binary value can similarly be assigned, shown by the purple bar on the right-hand panel of Figure 3.5.

It should be noted that the success of these autodetection methods relies on the consistency of kinetic spectra outside of these two anomalous features, hence BPT is used as a spacer whenever possible due to its relatively stable SERS lines. However, it is often useful to compare to other molecular spacers that are less temporally consistent. The variation in spectra over time is often due to the varied packing densities of different monolayers meaning exclusion of impurities from the hot-spot is more challenging. When impurities are present in the hot-spot this can lead to additional Raman lines which are neither picocavities nor flares, but may be flagged as either. The autodetection methods described here still work in these cases, but the errors involved are higher.

3.3 Theoretical Simulations

It is often beneficial to use theoretical modelling packages in order to simulate the near- and far-fields from a nanostructure. This can then be compared with experimentally observed

results and evaluated based on their similarity. In this thesis, I make use of both Finite-Difference Time-Domain and Boundary Element Method simulations.

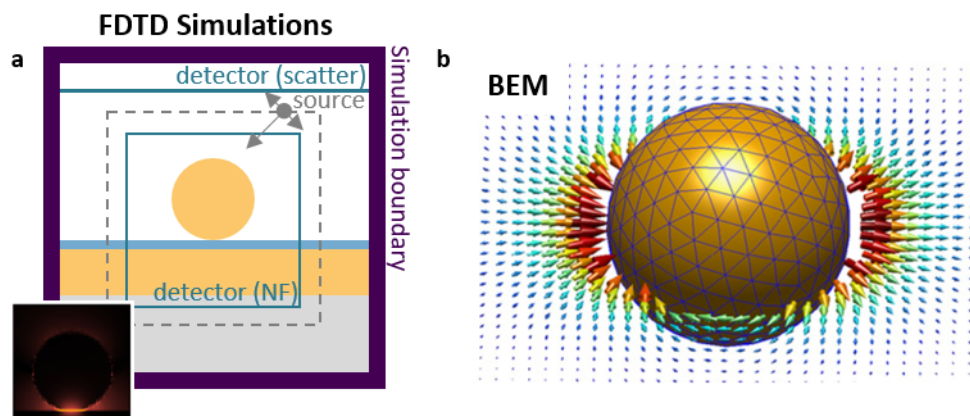


Fig. 3.6 **Theoretical Methods.** **a** Simulation geometry for a finite-difference time-domain (FDTD) simulation of a nanoparticle-on-mirror structure. Inset shows calculated field intensity. **b** Simulated electric field surrounding a nanoparticle, calculated via boundary element method (BEM). Taken from [81]

3.3.1 Finite-Difference Time-Domain Simulations

Finite-Difference Time-Domain (FDTD) simulations are used to simulate the field around a nanostructure as well as the absorption and scattering cross sections as a function of wavelength. The FDTD method involves creating a mesh grid across the system and solving the time-dependent Maxwell equations for each cell. In this thesis I use the commercial software Lumerical FDTD Solutions v8.12. A typical simulation geometry is shown in Figure 3.6a, showing how the source, detectors and boundaries are positioned. The lower inset shows a resultant field-intensity distribution. Dielectric functions for gold, silicon and glass are taken from Johnson & Christy [19] and Palik [82].

3.3.2 Boundary Element Method

In Chapters 6-7, more complex theoretical structures are analysed. Simulations of these structures are carried out using the Boundary Element Method (BEM) due to its higher computational efficiency. In BEM, the surface is discretised and Green's functions are calculated from each discretisation element to the rest, giving a matrix. Solving boundary conditions enables surface charge and current densities to be calculated, from which near-

and far-fields can also be calculated. An example showing the electric field surrounding a single gold nanoparticle is shown in Figure 3.6b [81].

3.4 Sample Fabrication

3.4.1 Nanoparticle Aggregates

Aggregates in Solution

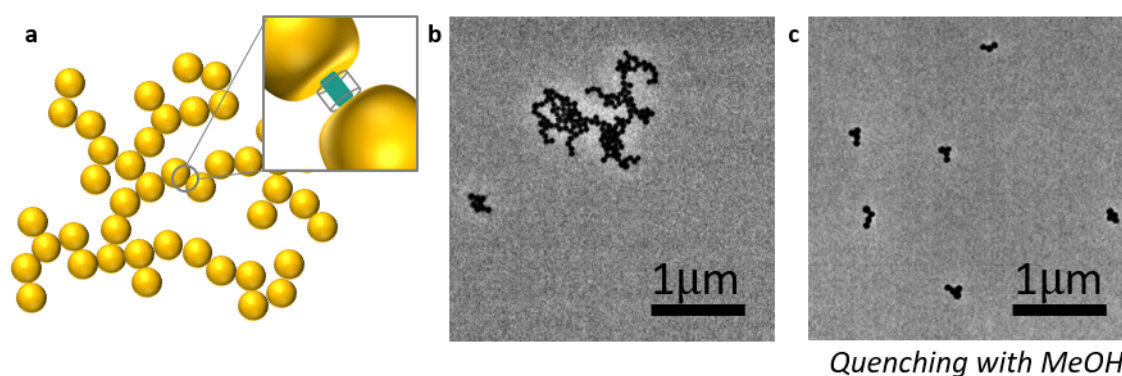


Fig. 3.7 **Nanoparticle Aggregates.** **a** Schematic of a nano-aggregate. Inset shows CB[n] host-guest chemistry within the gap. Scanning electron microscope images showing aggregates form **b** without, and **c** with quenching by addition of methanol.

To form long-chain aggregates, commercially purchased nanoparticles are mixed with 1 mmol CB[n] in a 15:1 volume ratio. It is important not to add too much CB[n]. If this is the case the aggregation will not proceed since each individual nanoparticle will be fully covered and CB[n] is not able to bind to itself.

Under the correct conditions long-chain fractal aggregates such as those shown in Figure 3.7b are formed. The completion of the aggregation process is easily confirmed by the change in colour of solution from red-pink to a dark purple, demonstrating the shift in plasmonic resonance modes. The length of aggregate can be changed by adding methanol at different stages of the aggregation process to quench further aggregation. This is shown by the shorter aggregates observed in Figure 3.7c, where methanol was added after 5 s of aggregation, compared to Figure 3.7b in which no methanol was added. It is thought that this is due to a conjugation of methanol with the citrate buffer, which prevents the citrate from being displaced by CB[n] [59]. However the aggregation process is relatively fast, with close to full aggregation shown after 60 s, therefore reliability of quenching at the exact same point in time is low and this method is hard to reproduce.

When aggregates are formed for sensing purposes, the CB[n] is premixed with the analyte solution in the desired molar ratio. For analytes which fit sterically inside the particular CB[n] used, this leads to neat host-guest chemistry, illustrated in Figure 3.7a, inset (not to scale). Larger analytes, unable to fit entirely inside CB[n], can still be shown to experience similar field enhancements. Therefore it is thought that they either fit partially in or else sequester in the gaps surrounding the CB[n], but still in the hotspot. This is discussed in later chapters. However it should be noted that in order to utilise this system with larger analytes, the analyte must be added after CB[n] is added to the nanoparticle solution, otherwise it can prevent aggregation.

Dried Aggregates

Single gold aggregates can be analysed by drying them down onto various substrates. Smooth gold substrates are formed using the same method described in Section 3.4.2. Silicon wafers are purchased from Si-Mat and cut to size. SiO₂ (glass) coverslips of 50 μm thickness are purchased from Thermo Scientific.

The aggregates are formed under the same conditions as in solution, and left for 15 min to ensure full aggregation. They are then drop-cast onto the desired substrate and left to dry fully, before being rinsed thoroughly with dionised water. Previous studies have shown that drop-casting aggregates onto a substrate does not markedly affect the 3D structure [83], due to the strong CB[n]-nanoparticle binding.

3.4.2 Nanoparticle-on-Mirror

The fabrication of NPoM samples is a three-step process, involving the fabrication of the gold film, the formation of a spacer (here we focus on self-assembled monolayers), and the drop-casting of nanoparticles.

Gold films are fabricated via a template-stripping method. This involves evaporating 100 nm of gold onto a large silicon wafer (Si-Mat). Another silicon wafer is cut into $\sim 1 \times 1$ cm pieces using a diamond pen. These pieces are glued to the larger wafer using Epo-Tek 377 epoxy glue and the wafer cooled from 150 $^{\circ}\text{C}$ to room temperature over the course of a couple of hours. Once cooled, the small pieces can be peeled off to reveal an atomically smooth gold surface, mimicking the structure of the silicon surface.

Self-assembled molecular monolayers are formed on the surface by immersing a small piece of this template-stripped gold in a solution of the desired molecule for a set amount of time. The self-assembly process is shown in Figure 3.8a i-iii. The molecules are attracted to the gold surface and at first lie flat along it. After a while, the surface is covered in this way

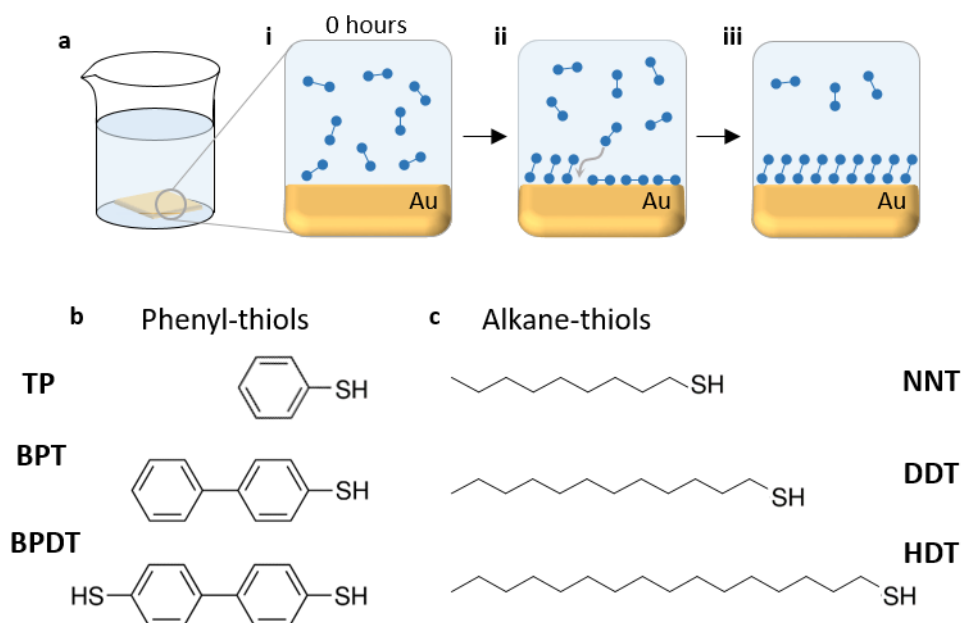


Fig. 3.8 Formation of Self-Assembled Monolayers. **a** Illustration of self-assembled-monolayer fabrication, with **i-iii** showing the various stages of formation. **b** Phenyl-thiols used as molecular spacers: thiophenol (TP; top), biphenyl-4-thiol (BPT; middle), biphenyl-4,4'-dithiol (BPDT; bottom). **c** Alkanethiols used as molecular spacers: nonanethiol (NNT; top), dodecanethiol (DDT; middle), hexadecanethiol (HDT; bottom).

and the molecules are forced into a more upright position in order to maximise the number of molecules in contact with the surface. Eventually the entirety of the surface is covered with a monolayer of the molecules.

The now-covered gold film is then removed from the solution and rinsed with fresh ethanol to remove any excess molecules. It is then dried with a nitrogen gun. Some of the SAM-forming molecules used in this thesis are shown in Figure 3.8b,c. Ideal deposition conditions vary slightly between molecules, but in general the molecules tend to be made in a 1 mmol solution of dry ethanol before being immersed for 20–22 h. It is important to use very pure, dry ethanol (200 proof, anhydrous, > 99.5%) as any impurities will disrupt the formation of the SAM. The effects of this are clearly observed, as any subsequent SERS signal is then drastically weakened. It is thought that this is due to the disruption of the $\pi - \pi$ stacking.

The deposition time and molecular concentration can be varied interchangeably, although not linearly. For some molecules, such as di-thiols, large molecular aggregates can be clearly seen in dark-field to have built up on the surface if the deposition time is too long. Therefore molecular concentration is increased ten-fold to 10 mmol and the deposition time reduced

to 1 h. Alkanethiols are used as control spacers for a non-Raman active molecular SAM of similar height to phenyl-thiol molecules. However the formation of these SAMs is often imperfect as the long carbon chains are not rigid and are therefore prone to folding over on themselves, especially since there is no $\pi - \pi$ interaction between adjacent molecules. For this reason higher concentrations are often used.

Once the SAM has been successfully formed on the gold film, nanoparticles are drop-cast on it and then the sample is rinsed with deionised water. Nanoparticles are bought from commercial supplier BBI solutions in nominal diameters 40, 60, 80 and 100 nm. They are charge stabilised in solution with a mix of trisodium citrate and citrate molecules, which are displaced from the nanoparticle surface by the SAM on contact. Drop-casting times range from 10 s–1 min, depending on factors such as the charge of the underlying SAM.

Chapter 4

Optimising SERS from Nanoparticle Aggregates

This chapter focuses on the characterisation and optimisation of nanoparticle aggregates (specifically those formed by self-assembly with cucurbit[n]urils) for molecular sensing techniques. Metal nanoparticle aggregates support a large number of plasmonic hot-spots within the inter-nanoparticle gaps, and these can be utilised to probe the molecular vibrations of analytes placed in these hot-spots through surface-enhanced Raman spectroscopy (SERS) [84, 85].

Here, I will first discuss how statistical techniques can be used to maximise the extraction of information from complex SERS spectra of aggregates and analytes in solution. Detection of synthetic cannabinoids by law enforcement currently relies on lengthy in-laboratory tests in order to correctly measure concentration. As such there is a need for simpler techniques, with the ultimate goal being roadside testing via SERS measurements. I will then look in detail at how anchoring aggregates to different substrates in a ‘dry’ environment can further affect SERS signals. This is then corroborated with a theoretical study involving finite-difference time-domain (FDTD) simulations on a simplified ‘toy model’ system. This study on dried aggregates is motivated by a need for more reliable SERS sensing substrates, for use in detecting any multitude of desired analytes. For this the CB[n] is itself measured as an analyte in order to avoid having to consider relative molecular binding in the system. The next step would be to then introduce synthetic cannabinoids into the dried aggregates system. Parts of this chapter have been published in references [58] and [39].

For the Raman measurements in this chapter a commercial Renishaw inVia microscope is used. This is due to the inbuilt mapping functions available, as well as the ability to switch between incident lasers of 633nm and 785nm wavelength. For the dark-field measurements

the Lumenera Infinity 3 camera is used in conjunction with an Ocean Optics Seabreeze spectrometer, as described in Section 3.1.1.

4.1 Aggregation Kinetics and the Formation of Chain Modes

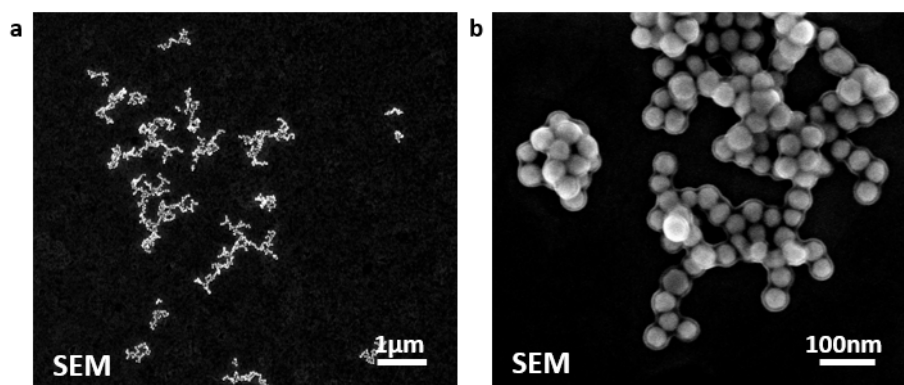


Fig. 4.1 **Scanning Electron Micrographs.** SEM images at different magnifications show the 3D fractal geometry of 40 nm aggregates self-assembled via addition of CB[7].

Colloidal nanoparticles have been used to form nano-aggregates through a variety of methods, including aggregation by DNA [86], proteins [87, 88], dyes [89], alcohols [90], polymers [91, 92], and optical fields [93]. A big issue faced when forming nanoparticle aggregates for SERS sensing is the reproducibility of inter-particle spacing distance. For typical colloidal aggregation, a variation in this gap distance across a single sample produces a broad absorption across the visible and near-infrared spectrum due to the multitude of plasmonic resonances produced (Figure 2.6 shows how sensitive the coupled plasmonic modes between nanoparticles are to gap distance). Within each hot-spot, therefore, the residing molecules will experience a different orientation, strength and resonant frequency of the plasmonic field. This means that the SERS signal measured is averaged over all field-molecule configurations, which is an undesirable situation for quantitative chemical sensing.

In contrast, aggregates formed with consistent gap spacing distances support degenerate localised plasmon modes in the gaps between nanoparticles. Charge oscillations in one nanogap mix strongly with charge oscillations in surrounding nanogaps, resulting in spatially distributed plasmonic ‘chain’ modes. Here I study aggregates formed by self-assembly of colloidal nanoparticles with CB[7], from the family of cucurbit[n]uril molecules (more details in Chapters 2 and 3). Cucurbit[n]uril (CB[n]) molecules are macromolecules with a rigid

height of 0.9 nm that defines the gap distance in the resulting aggregates. The aggregates can be described as having a near-fractal nature [69], as shown by the scanning electron micrograph (SEM) images in Figure 4.1.

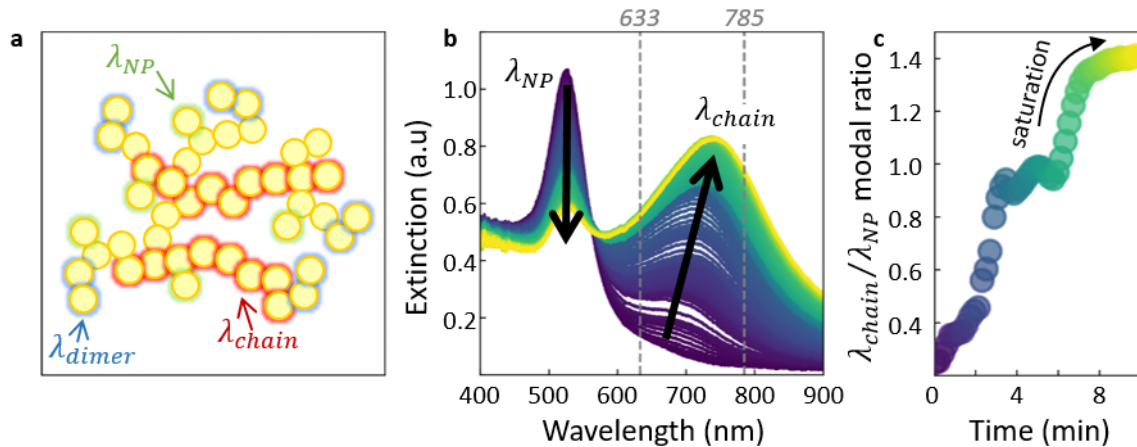


Fig. 4.2 Formation of Nanoparticle Aggregates. **a** Schematic distribution of single-nanoparticle (green), dimer (blue) and chain modes (red) across a fractal aggregate. **b** Time-resolved extinction spectra. Dashed lines show wavelengths of lasers used in this chapter. **c** Corresponding ratio of chain mode to single-nanoparticle mode intensity over a period of 10 min.

Previous studies on this CB[n] aggregate system have shown that the optical response of the aggregate can be broken down into its composite units. There are three main sets of modes observed: single-nanoparticle modes (λ_{NP}), dimer modes (λ_{dimer}), and chain modes (λ_{chain}). As illustrated by the schematic in Figure 4.2a, the single-nanoparticle and dimer modes have been shown to be situated around the peripheries of the aggregate, and have higher energies. In comparison, the lower-energy chain modes extend throughout the central axes of the aggregates [94].

The emergence of each of these modes can be observed *in situ* throughout the period of aggregation. Here this is measured by UV-vis spectroscopy, in which a broad-band light source is used to illuminate the aggregates forming in solution, and extinction spectra recorded over time. This can be seen in Figure 4.2b. The extinction spectra can be seen to vary from the initial state of colloidal nanoparticles at $t = 0$ s (purple) to the aggregated state at $t = 10$ min (yellow). Note that aggregation here is purposely slowed down by not shaking the solution. This eases observation of aggregation.

Initially the individual colloidal 40 nm diameter nanoparticles support a single-nanoparticle plasmon mode at 530 nm. The addition of CB[7] first induces dimerisation, resulting in emergence of a new mode around 640 nm with a resulting reduction in the single-particle

mode. At later times, higher-wavelength chain modes emerge as the aggregate size increases, red-shifting with increasing chain length. Although the single-particle and dimer modes are still supported around the edges of the aggregate, the optical response in large aggregates, such as those used here, is dominated by the spatially centralised chain modes.

The ratio of chain-mode intensity to single-particle mode over time (Figure 4.2c) can give some measure of the aggregation process over time. This is discussed in detail in [69]. Nanoparticle aggregates saturate in size once surface coverage of CB[7] limits the probability of further aggregation.

4.2 Plasmonic Sensing with Principal-Component-Analysis

The large enhancements provided by plasmonic hot-spots makes surface-enhanced spectroscopies such as SERS well equipped for trace-level detection of drugs and other molecules of interest. In this section I look at Δ_9 -Tetrahydrocannabinol (THC), which is the active ingredient in cannabis, as well as so-called ‘synthetic cannabinoids’. Also known as ‘legal highs’ these are synthetic analogues of THC which attempt to get around legal loopholes in drug laws by slightly changing the chemical structure to stay one step ahead of legislation. Although these loopholes have now been closed, the prevalence of legal highs is still on the rise, and in fact are much more dangerous than the THC in ‘regular’ cannabis.

SERS has previously been used in conjunction with gold-coated glass capillaries to detect THC down to 1 nmol [95]. I show here how the use of carefully controlled nanoparticle aggregates alongside the principal-component-analysis (PCA) algorithm [96] can be used to detect cannabinoids below nanomolar concentrations, opening up the possibility for trace detection in urine.

To implement chemical sensing using SERS, the molecule of interest needs to be placed in the plasmonic hotspot. Here this is done using the encapsulator molecule CB[7], as detailed in Chapters 2 & 3. Although it is debated whether THC and other synthetic moieties are encapsulated fully inside the CB[n] molecules, it is clear from experiments that they are indeed undergoing surface-enhanced scattering and so must be in some way held in the hot-spot. Density functional theory (DFT) calculations such as that shown in Figure 4.3d appear to show that THC would fit at least partially in the CB[7] cavity, however this is not proven. If this were the case it would mean that some of the CB[n] molecules are used to bind the nanoparticles together and others were used to partially encapsulate analyte molecules on the surface. However knowledge of the exact configuration requires further study.

To demonstrate the sensing capabilities of this system, a concentration series is undertaken. In this measurement, the amount of gold and CB[7] is kept constant, with the concentration

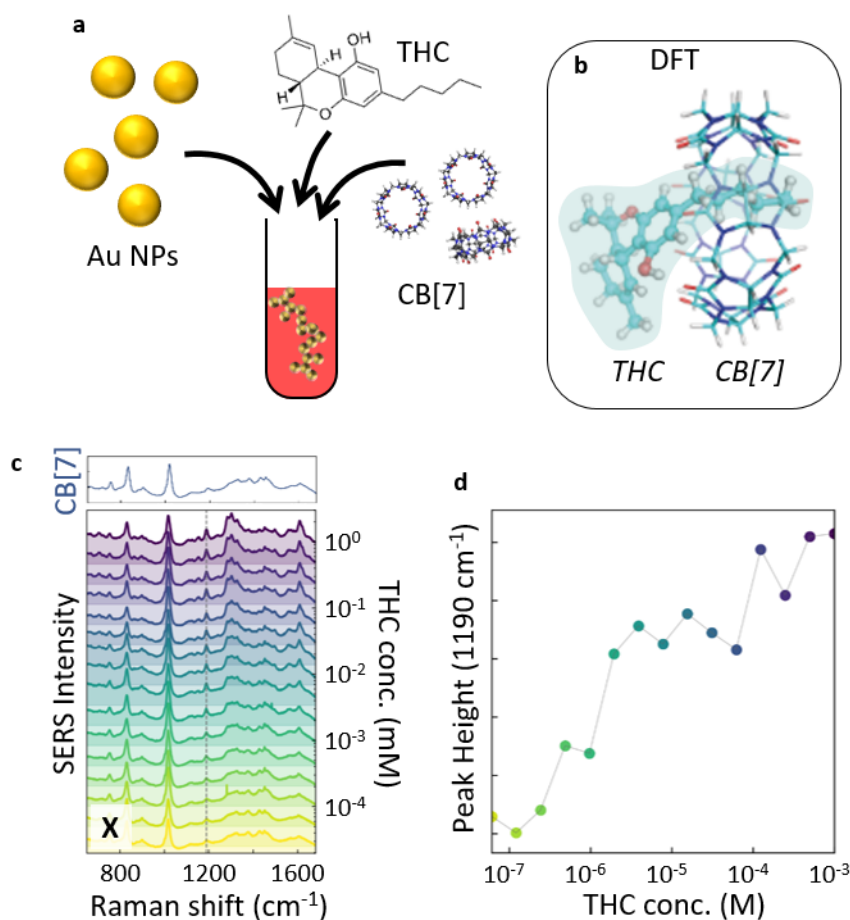


Fig. 4.3 Sensing THC Using Nano-Aggregates. **a** Schematic showing how an aggregate system is formed for plasmonic sensing of THC. **b** DFT geometry optimisation showing the simulated configuration of THC fitting partially inside the CB[7] cavity (taken from [58]). **c** SERS spectra of a concentration series of THC in methanol sequestered in CB[7]:Au nano-aggregates, offset for clarity (bottom panel). Dashed line shows 1190 cm^{-1} peak tracked in (d). X refers to this as a visualisation of matrix of raw data in Equation 4.1. Top panel shows control spectrum of CB[7] and gold with no THC present. **d** Tracking the 1190 cm^{-1} THC peak shows a decrease in peak height with concentration.

of THC in methanol halved at each point. The total volume remains constant. Since methanol is used as a solvent and has been shown to quench aggregation (Chapter 3), the THC solution is added only once aggregation has completed. The control spectrum showing an aggregate composing of only CB[7] and gold nanoparticles can be seen in the top panel of Figure 4.3c. The bottom panel shows the concentration series, with THC concentration reducing from top to bottom. In general SERS sensing either looks at the intensity of a single peak or the integrated spectrum and looks at how these change with concentration (it is also possible

to measure as a function of time or other variables of interest). However this system is complicated by the fact that both CB[7] and THC are organic molecules and so share a lot of the same chemical groups and molecular bonds. Although the vibrational energies observed in the SERS spectra will be shifted slightly by the interaction with the rest of the molecule, there is still a large amount of overlap, meaning picking out individual peaks is difficult. Additionally the molecules interact with each other, while both interacting with both the buffer solution and nano-aggregates. This makes things even more difficult to analyse by eye.

It can be seen that all these factors lead to a large degree of uncertainty when tracking a vibrational mode over a concentration series. Even when the relatively isolated bond at 1190 cm^{-1} is tracked, there is still a large degree of noise and overlap with CB[7] vibrations leading to a fluctuating curve in Figure 4.3d. When the integrated area is tracked instead, the results are even more compromised, due to the variation in background across the mixtures and the difficulty in removing this background. The uncertainty in these trends means that were an unknown concentration tested, there would be a considerable range over which the true concentration could lie.

To attempt to improve on this situation I make use here of the unsupervised algorithm known as principal component analysis (PCA) [96]. ‘Unsupervised’ here refers to the fact that we make no pre-conditions on the code to tell it which peaks belong to which molecule (although prior knowledge of the molecular spectrum is indeed used when analysing output results).

Principal component analysis is a statistical technique which, in completely general terms, is a method whereby n -dimensional data is transformed to a reduced set of dimensions for better visualisation. This is done by removing dimensions with small variances and combining those which vary similarly. In this way the reduced set of variables still contains most of the information of the original data.

The initial dataset is made up of a large number of correlated variables. Through orthogonal transformations, PCA combines these into uncorrelated linear combinations of variables. These combinations of variables are called the *principal components*, $T_{k,l}$. This can be thought of in terms of a matrix equation

$$\mathbf{X} = \mathbf{T}\mathbf{W}^T \quad (4.1)$$

where \mathbf{X} is the matrix of raw data, \mathbf{T} is the matrix of l principal components and \mathbf{W} is the ‘projection matrix’ of weighting coefficients [97, 98]¹.

¹The projection matrix is called as such because multiplying \mathbf{X} by \mathbf{W} gives the values of the projections of observations onto the principal components.

PCA is used in fields such as ecology [99], geology [100], data science [101] and many others, primarily to find clusters and patterns in data. It is also used extensively in spectroscopy, to distinguish between polymorphic mixtures of the same drug [102], between cancerous and non-cancerous blood plasma [103], and to classify lesions on coronary arteries [104]. Here I will demonstrate how it can be used to separate out the multitude of spectral contributions in individual SERS spectra for trace detection of drugs.

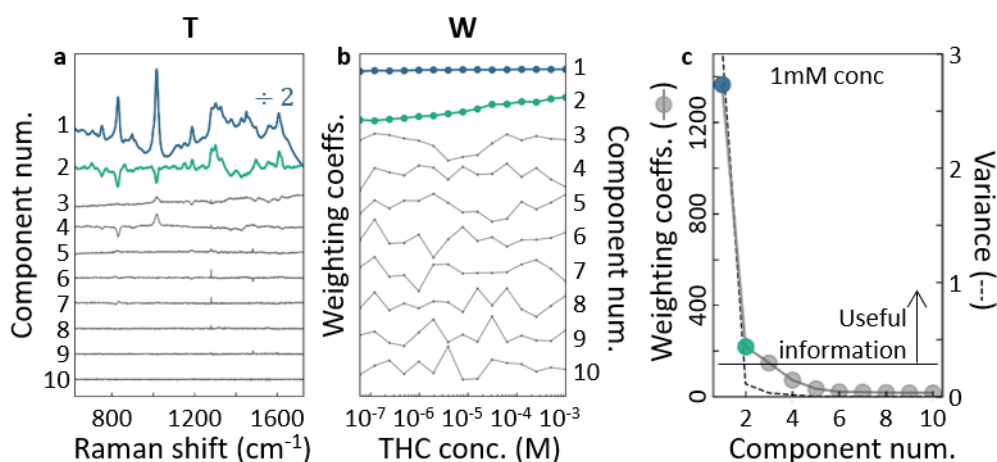


Fig. 4.4 Separation of Raw Data into Principal Components. **a** The first 10 principal components extracted from matrix of raw data, \mathbf{X} . Components are offset for clarity, and plotted against relevant Raman shift. First component (blue) corresponds to CB[7] vibrations, second component (green) corresponds to THC analyte. **b** The weighting coefficients for each component, at each value of THC concentration. Coefficients are offset for clarity and labelled by their relevant component number. **c** The weighting coefficient for each component plotted alongside equivalent variance, showing drop-off after the first couple of components (highest concentration only plotted here).

In terms of the Raman spectra problem considered here \mathbf{X} is the set of raw Raman spectra, with each column, k , corresponding to a different spectral position (these are the *variables*) and each row l an iteration of the spectrum at a different THC concentration. This can be visualised in Figure 4.4c (bottom panel). This raw data matrix is input into the PCA algorithm². From this we can extract a set of l linear combinations of variables. These linear combinations are called principal components and the matrix of linear components is given by \mathbf{T} . This is where the usefulness of PCA in analysing complicated spectra comes in. Because all the peaks related to the THC analyte (for example) will vary together with changes in concentration, they will therefore be correlated together and so combined via PCA

²The full details of how the algorithm works are not explained here, but the python package `sklearn.decomposition.PCA` is used, which draws on the method by Halko et al. (2009) [105].

into a single principal component. The same can be said for all the peaks corresponding to CB[7], and the same for the background buffer signal, the small signals from the cuvette, etc.

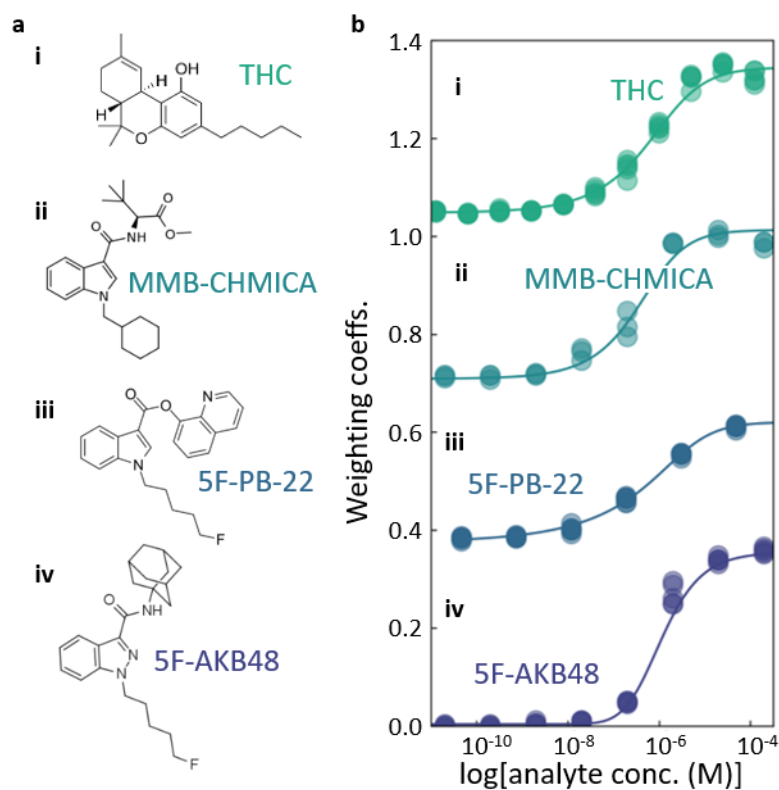


Fig. 4.5 **Sensing Synthetic Cannabinoids.** **a** Chemical structures and **b** corresponding Hill-Langmuir isotherms of weighting coefficients plotted against analyte concentration for each of the cannabinoids measured. Repeated measurements plotted on top of each other. Isotherms offset for clarity.

This matrix of principal components **T**, can be visualised in Figure 4.4a. The components are ordered from those with highest ‘variance’ to those with lowest³. The first component (blue) is recognisable as the spectrum relating to the CB[7] molecules, with some contribution from the cuvette (peak at 1000cm^{-1}). Since both these factors are kept constant throughout the concentration series, it is rational that they are combined into one component. The second component (green) then contains the contribution corresponding to the THC analyte. The subsequent components with reducing variance (grey) make up the contributions from the background signals including buffer solution as well as accounting for any interaction

³The ‘variance’ used to order the principal components refers to the distance from the rotated axes, not the variation in signal throughout the concentration series. Hence although the CB[7] signal does not vary throughout the concentration series, it is ordered first since it makes up most of the SERS spectrum due to its comparatively high Raman activity.

between molecules. The small negative peaks visible demonstrate this interaction, illustrating for example that molecule *A* will lead to a decrease in signal from molecule *B* peaks. A huge benefit of using PCA to analyse spectra is that minute spectral differences do not need to be pored over, and instead only a brief initial study is required to identify which component represents the analyte signal. In the system studied here, it is always the second component, due to the slightly reduced Raman activity of cannabinoids compared to CB[*n*].

The magnitude of each component in Figure 4.4a, known as the weighting coefficients, at each concentration in the series can then be extracted. This corresponds to \mathbf{W} in Equation 4.1 and can be visualised in Figure 4.4b. It can be seen that the weighting of component 1 is constant across the concentration series, as expected. In comparison the weighting of component 2, which corresponds to the signal from the analyte molecule, can be seen to steadily increase with increasing concentration, thus evidencing the efficacy of this method to correlate to analyte concentration. The remaining components are dramatically decreased in weighting, as is expected and designed by the algorithm. This exponential decrease with subsequent components can be visualised in Figure 4.4c, where the weighting of each component (for the highest concentration) is shown alongside the corresponding variance. Since PCA is a dimension-reduction algorithm, not all the principal components need to be kept. Instead only the first l components need be produced from the first l eigenvectors, where it is generally accepted that for $l \gg 3 - 4$ the components reduce to noise and contain no further useful information (Figure 4.4c). As such Equation 4.1 reduces to $\mathbf{X} = \mathbf{T}_l \mathbf{W}_l^T$.

The experiment is repeated 3 times and the second component (relating to the THC analyte) is shown here in Figure 4.5b,i, with the repetitions shown overlaid demonstrating the high degree of reproducibility of this technique. The experiment is then repeated for a range of cannabinol synthetic analogues (Figure 4.5a,b ii-iv). The component weighting is plotted as a function of concentration for each analogue. Each concentration series is again also repeated 3 times and a Hill-Langmuir isotherm is fitted to the results. The Hill-Langmuir isotherm is commonly used to describe the interaction between an analyte and a macromolecule by considering the number of binding sites available.

This can be compared with Figure 4.3c,d. It is clear that calculating the principal components and considering a Hill-Langmuir isotherm of their weighting factors is a much more reliable method for estimating concentration of analyte in solution than looking at the raw variation in peak heights. The relatively good fit of the Hill-Langmuir isotherm means that for a given value of component weighting factor, a concentration of analyte can be extracted with a much larger degree of certainty. However there are clearly improvements to be made. It can be seen that there is up to an order of magnitude variation in detection limit as well as reproducibility between the different analogues measured here. This is likely due to

variation in solubility of the analyte in the methanol, as well as ability to fit inside the CB[7] and therefore the nano-aggregate hot-spot. These are areas in which clear improvements could be made to further develop this technique. A potential avenue of research could be to investigate the effects of different solvents.

4.3 Mapping SERS in CB: Au Plasmonic Aggregates

In this section I will move from bulk measurements of aggregates in solution to measuring individual aggregates in the dried state. I will analyse how anchoring aggregates to different substrates can further affect the plasmonic hot-spots and SERS signals produced. This is then followed by a theoretical study on a ‘toy-model’ system using finite-difference time-domain methods.

4.3.1 Experimental Results

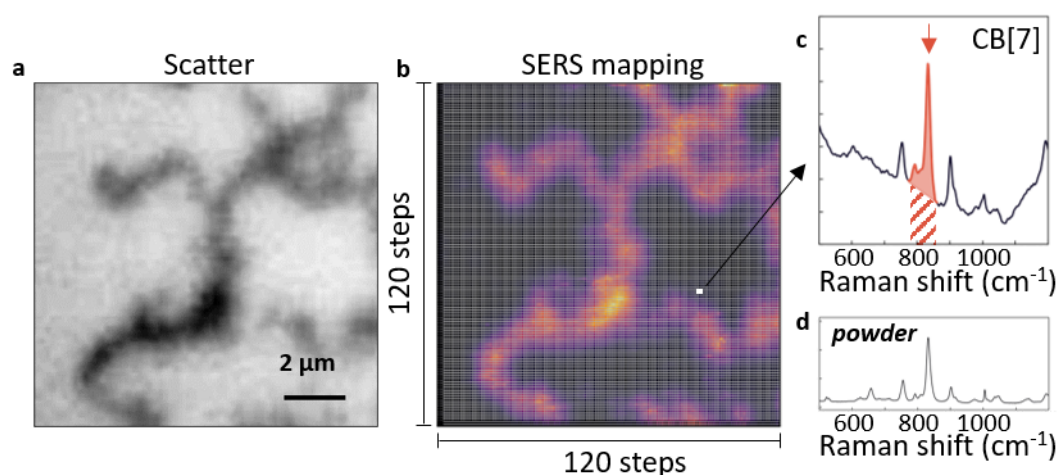


Fig. 4.6 **Mapping SERS Intensities Across Nano-Aggregates.** **a** Bright-field scattering image of nano-aggregate dried onto gold substrate. **b** SERS map of aggregate from (a), with 120×120 grid overlaid, showing the points at which a SERS spectrum is taken to make up the map. **c** Example of CB[7] spectrum taken at a point on the grid. Red highlighted region shows mode which is integrated to make up map. Hashed area shows background area. **d** CB[7] powder Raman spectrum for comparison.

The aggregates are formed in the same way as those described in Section 4.1, but here no analyte is inserted into the CB[n] cavity, and instead SERS signals from the CB[n] itself are tracked. This removes ambiguity in the positioning of the molecule with respect to

the hot-spot, since being the aggregating molecules the CB[*n*] must be in the centre of the hot-spot.

When such aggregates are observed in solution they fill only a small amount of the optical focal region, thus reducing the available SERS signal. In order to map the Raman signal from individual aggregates, I therefore anchor the aggregates onto solid substrates. This allows for tighter focusing of light with higher numerical aperture (NA) objectives, thus collecting higher SERS signals. Here once the aggregates are formed, they are drop-cast onto solid substrates at low enough concentration to image them individually. It has been shown in previous studies that since the binding between CB[*n*] and the nanoparticles is strong (~ 0.3 meV), drop-casting aggregates onto a substrate does not markedly affect the 3D structure [83]. Other methods to image individual nano-aggregates include binding them in-situ within microfluidic channels, as has been shown in [106].

Three different types of substrate are used: template-stripped gold (Au), glass cover-slides (SiO₂), and silicon wafers (Si). See Section 3.4.2 for fabrication details. SiO₂ is expected to most directly correlate to how the aggregate acts when diffusing in solution. As a plasmonic material the Au substrate is expected to augment the plasmonic enhancement, whereas Si is more absorptive [19] and so expected to damp the fields.

The aggregates imaged here are tens of microns in length, and as such are visible in standard bright-field scattering configuration (Figure 4.6a). Here I show how by rastering a computer-controlled stage across a $12 \times 12 \mu\text{m}$ area in 100 nm increments and taking a SERS spectrum with a confocal pinhole at each point, a map of the SERS intensity across the aggregate can be imaged.

At each point in the grid a single SERS spectrum is measured (Figure 4.6b,c). This shows a number of vibrational peaks corresponding to the CB[7] spacer molecule. This is confirmed via comparison to the Raman spectrum of CB[7] powder (Figure 4.6d), with some slight differences expected due to conformational hindrance by the gold nanoparticles [107]. In particular, the triplet of peaks in the $700\text{-}950\text{ cm}^{-1}$ range is a well-recognised vibrational signature of CB[7].

Here I use the Raman strength of the central 832 cm^{-1} peak corresponding to a ring-breathing mode of the CB[7] (red arrow, Figure 4.6c) in order to map the SERS activity across the aggregate. The mode is normalised to laser power and integration time before being background-subtracted and then integrated, with the integrated value at each point forming a matrix of pixel values to give the resulting SERS intensity map.

These intensity maps are constructed for gold nano-aggregates deposited on substrates of Au, Si and SiO₂ and then repeated for SERS with excitation wavelengths 633 nm and 785 nm, mapping the 832 cm^{-1} line in all cases. This is shown in Figure 4.7. It can be seen

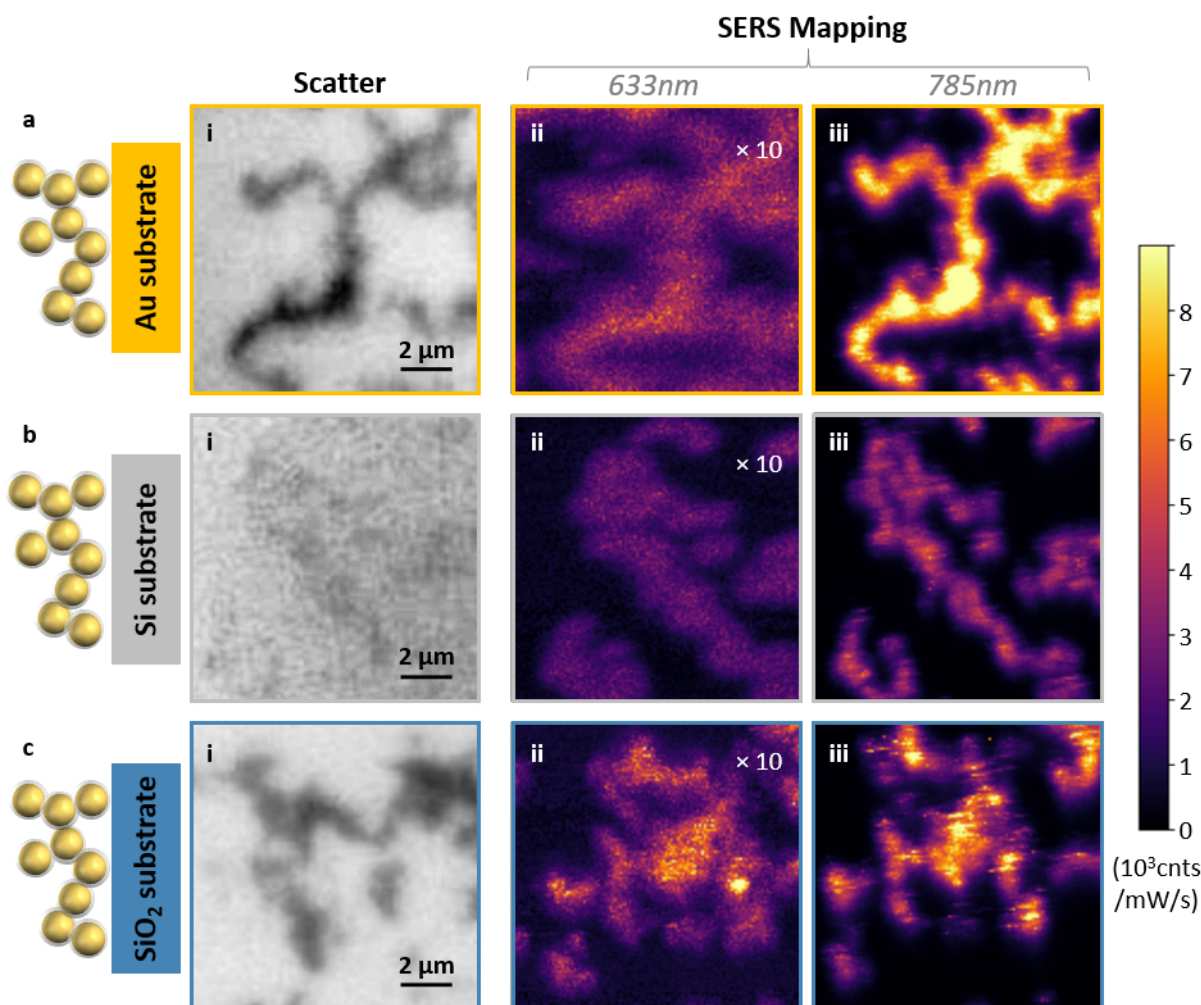


Fig. 4.7 **SERS Intensity Maps.** Aggregates dried onto **a** gold, **b** silicon and **c** silicon dioxide substrates and their corresponding **i** bright-field scatter, and **ii-iii** SERS intensity maps (excitation with either 633 nm or 785 nm respectively).

that the aggregate shape visible from the scattering images is clearly reproduced by mapping the SERS intensity, although with a variation in intensity leading to variations in resolution (this will be discussed later). Indeed there are even features which cannot be resolved in bright-field scattering experiments which are visible when characterised with SERS mapping.

As well as looking at the integrated SERS peak intensity, the integrated SERS background below the peak (hashed region, Figure 4.6c) can also be mapped across the region of interest, as shown in Figure 4.8. This is shown to also clearly map the aggregate, with direct correlations to SERS peak intensity (Pearson coefficients: 0.66-0.99). This is expected since

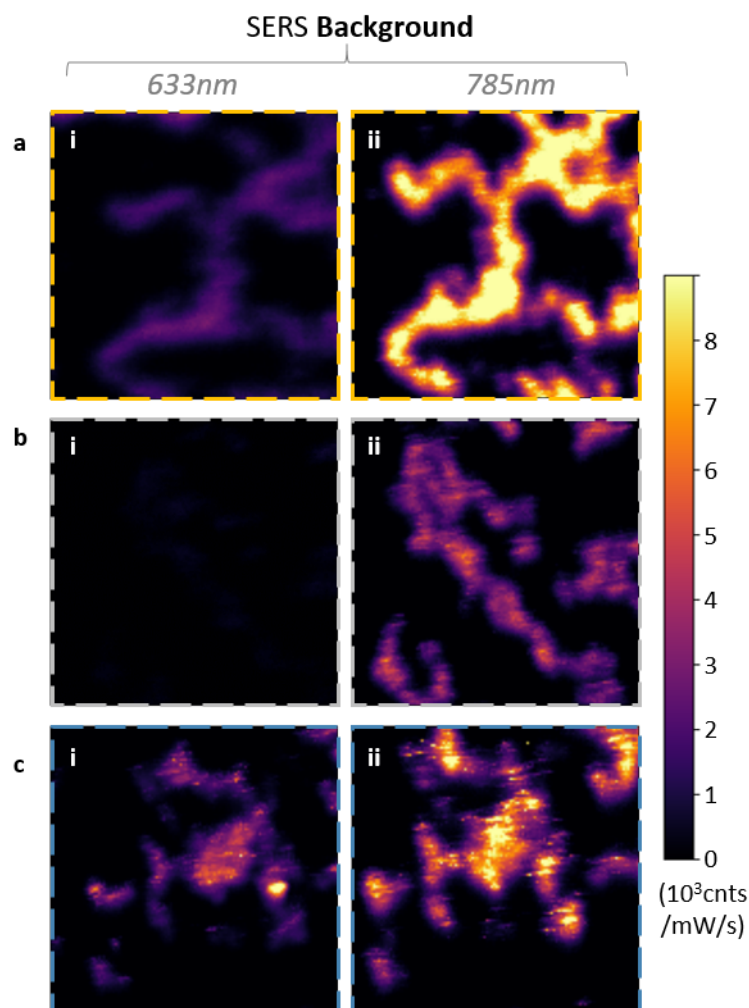


Fig. 4.8 **Plasmonic Background Maps.** Maps of the extracted SERS background for the aggregates in Figure 4.7 on **a** Gold, **b** Silicon and **c** Silicon Dioxide with **i** 633 nm, and **ii** 785 nm laser excitation.

it has previously been shown that the SERS background comes from inelastic light scattering in the metal and therefore is directly related to the plasmon [108, 60].

The results of the previous two figures are summarised in Figure 4.9a. Here the average SERS signal is shown by the filled bars, stacked on top of the average background signal, both for the area containing the aggregate only. It can be seen that depositing aggregates on Au substrates gives the strongest signals, both from SERS peaks and background. I will show in simulations in Section 4.3.2 that this is due to the plasmonic coupling of gap plasmons to image charges in the substrate, much the same as the coupling that occurs in NPoM structures (Chapter 2).

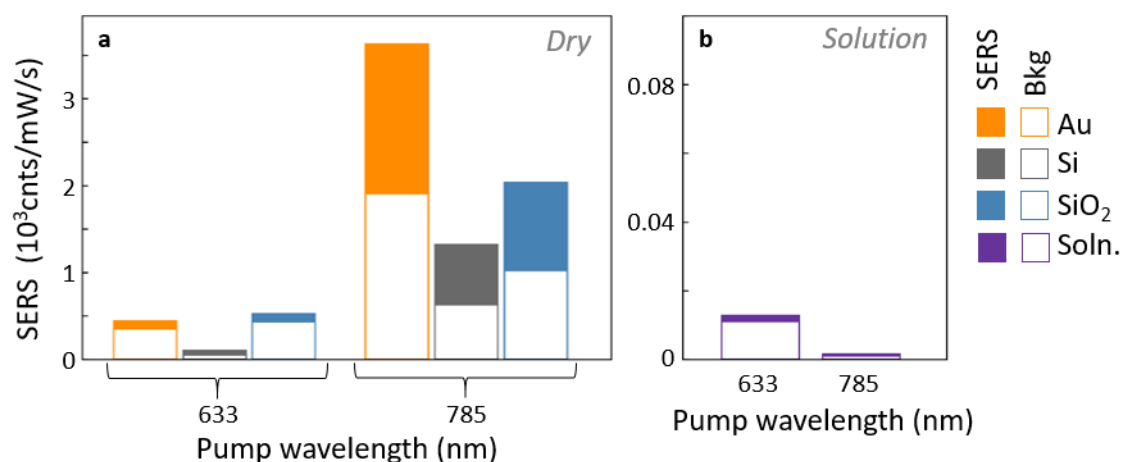


Fig. 4.9 **SERS and Background Counts.** **a** Stacked bar-chart showing averaged SERS counts (filled) and background counts (open) across the mapped aggregate image for different substrates, at excitation wavelengths of 633 nm and 785 nm. **b** Equivalent measurements for aggregates in solution.

However the SERS signal is only 2-fold weaker for aggregates deposited on SiO₂, where there is no such plasmonic coupling to the substrate. This suggests that the nanoparticle-substrate coupling is not the dominant factor for SERS enhancement, and that in fact coupling between adjacent nanoparticles in the aggregate plays more of a role. The SERS signals from aggregates on Si are significantly reduced from both other cases. This is expected due to the higher absorptive properties of Si, which dampen the plasmonic resonance and therefore reduce the SERS signals visible. The SERS background follows the same trends.

The 785 nm laser gives consistently higher signals than using a 633 nm laser, due to its resonance with the chain modes of the gold nanoparticle aggregates (Figure 4.2b, dashed lines). It is also noted that the SERS peaks are of similar strength to the background intensity for SERS measured with the 785 nm laser, while the background dominates for 633 nm. This is likely because the 785 nm laser is much closer to the chain-mode resonance and so will result in modes tightly confined to the gaps, and therefore high SERS counts from the molecules in these gaps. In comparison the 633 nm laser is likely to result in plasmon modes more distributed around the entire nanoparticle, leading to a comparatively higher SERS background, which has been shown to come from the metal [108, 60].

An estimate of the number of counts recorded per CB[7] molecule can be made by calibrating the bright-field reflectance of the aggregate on gold to known values for NPoM

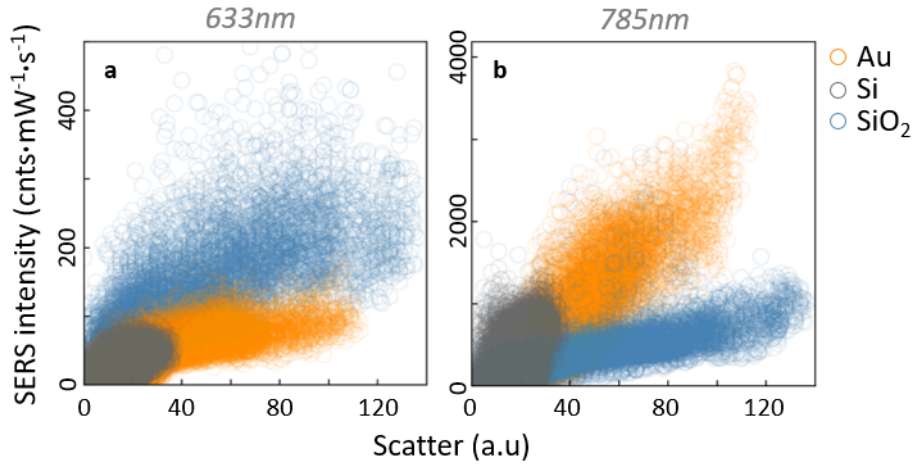


Fig. 4.10 **Correlation of SERS with Bright-Field Scatter.** Scatter plot showing correlation between bright-field extinction of each pixel and its SERS intensity with **a** 633 nm and **b** 785 nm excitation laser, for all three substrates.

and gold surfaces:

$$\frac{\text{Single-Pixel Scatter (Aggregate)}}{\text{Single-Pixel Scatter (Au Surface)}} \Big|_{532\text{nm}} = N \times \frac{\text{NPoM Reflectance}}{\text{Au Reflectance}} \Big|_{532\text{nm}} \quad (4.2)$$

where the reflectance from a gold nanoparticle-on-mirror and a flat gold surface are calculated by FDTD simulations. All values were evaluated at 532 nm. N therefore gives an estimate for the number of junctions probed per pixel and is found to have a value of $N \approx 1.1$. It is estimated that each junction contains roughly 100 close-packed CB[7] molecules [18]. Since the aggregate deposited on a gold has a SERS integrated signal on the order of 1000 cnts/mW/s, it can be estimated that each CB[7] molecule contributes 10 cnts/mW/s, in line with SERS observations in NPoM configurations for the same gaps and hence field enhancements.

These measurements can be compared to equivalent measurements of aggregates in solution. With equivalent laser power and integration times, it can be seen that the SERS counts measured in solution are 3 orders of magnitude less than for their dry counterparts. It can be shown (Appendix A) that this can be accounted for by the number density within the focal spot. The concentration within the solution is relatively low (to prevent destabilisation) and therefore as a fraction of the measured area, only a small part of the solution is made up of the volumes of plasmonic hot-spots. In comparison, when studying the dried aggregates it is possible to focus exactly on an aggregate and so a much higher proportion of the focal spot is filled with hot-spot regions. The amplification in signal due to deposition on a substrate is

greater when using a gold substrate due to the extra degree of plasmonic enhancement, and conversely it is lessened for Si due to absorption into the substrate. Surprisingly it is found that the signal from the 785 nm laser in such solution aggregates is now 5-fold weaker than from 633 nm, in the opposite ratio to dried aggregates. This can perhaps be explained by the higher absorption of light by water at 785 nm when compared to 633 nm, quoted as reaching 6-fold differences [109, 110].

The scattering signal from the bright-field images can be correlated to the SERS intensity for each pixel in turn across all 3 substrates. This is done for both the 633 nm and 785 nm SERS maps and is shown in Figure 4.10. The strong correlation between bright-field scatter and SERS signals across each point in the image maps can be seen for all three substrates. Since, on average, scattering is related to the number of nano-gaps at each pixel, this suggests that SERS signal also linearly adds from each nano-gap [106]. This is not immediately obvious since the distances between SERS emitters are sub-wavelength so constructive interference is possible. The situation demonstrated here is analogous to the typical linear increase of SERS with number of nanoparticles when no coupling is present.

To understand these differences more clearly, dark-field scattering measurements are taken to probe the plasmon resonances (Figure 4.11). These scattering spectra are taken over a number of aggregates on the different substrates and of an assortment of different positions, in order to give a representative picture of each system. The variation evidences the spatial inhomogeneities, but there are generally common features on each substrate. It is necessary to take numerous measurements across different positions of the aggregate for a dried aggregate fixed to a substrate in order to get the entire picture of the system. This is in comparison to an aggregate in solution, in which the variation in aggregate position is averaged out by diffusion over the time of measurement.

While a weak single-particle mode around 530 nm is always visible, the dominant chain modes are clearly shown at longer wavelengths. These red-shifted peak positions depend on the coupling strength between the nanoparticle and image charges in the substrate. When on SiO₂ the coupled mode is similar to in solution (Figure 4.11d), with a small red-shift due to very weak coupling to the substrate (Figure 4.11b). This red-shift is much larger when aggregates are placed on Au, and in fact the chain modes are largely out of the spectral window visible with the spectrometer. The high degree of coupling to the gold substrate also leads to emergence of a complex array of new modes, as those running through the aggregate couple to image charges formed in the substrate, with higher order components observed in the region 600-800 nm (Figure 4.11a). When on Si substrates the aggregate chain modes blue-shift to shorter wavelengths due to the damping by absorption in the semiconductor.

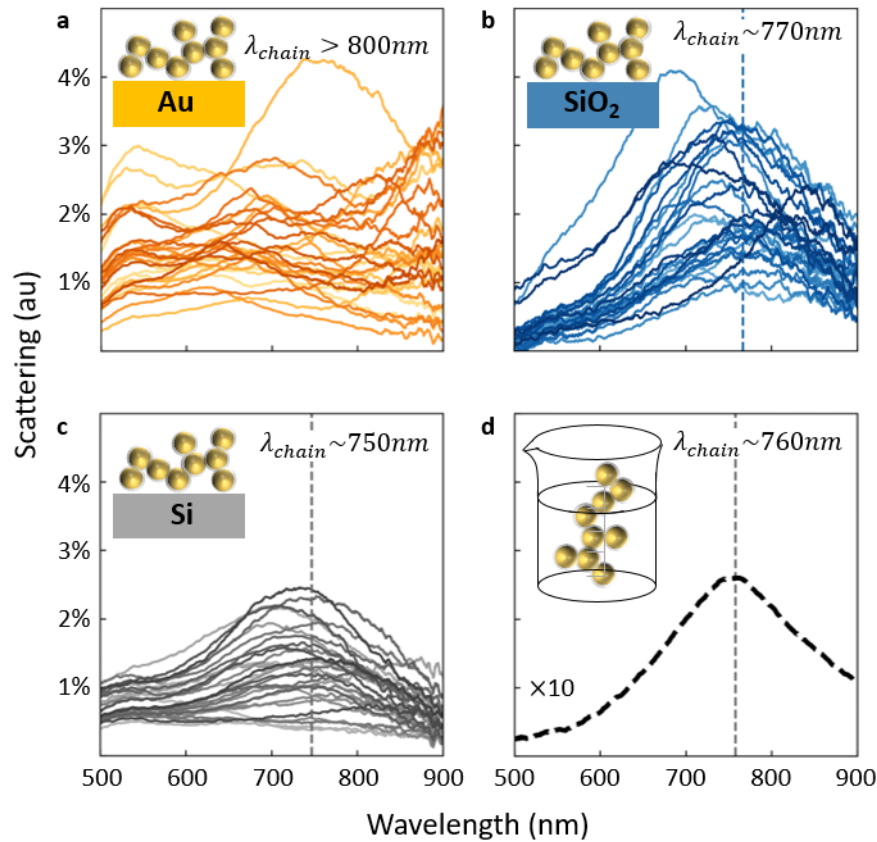


Fig. 4.11 **Dark-Field Scattering Spectra.** Representative collection of dark-field scattering spectra across different positions and aggregates on **a** gold, **b** silicon dioxide, and **c** silicon. Dashed line shows average chain-mode wavelength, if visible in spectral window. **d** Scatter of aggregates in solution, with no substrate present. Chain mode labelled.

This is also the reason that SERS is so much weaker on the Si substrates, since both elastic and inelastic scattering are similarly affected.

4.3.2 Finite-Difference Time-Domain Modelling

In order to fully investigate the different coupling at different positions in the structures I have simulated a ‘toy model’ version of the aggregate-on-substrate structure using finite-difference time-domain simulations (details in Section 3.3.1). The experimental configuration is mimicked with a toy model comprised of a chain of four nanoparticles spaced above substrates of either Au, Si or SiO₂ (Figure 4.12a) [19, 82]. The spacer layers at each nanoparticle-nanoparticle junction (herein labelled NP-NP) as well as at each substrate-nanoparticle (substrate-NP) junction have a height of 0.9 nm and refractive-index of 1.4

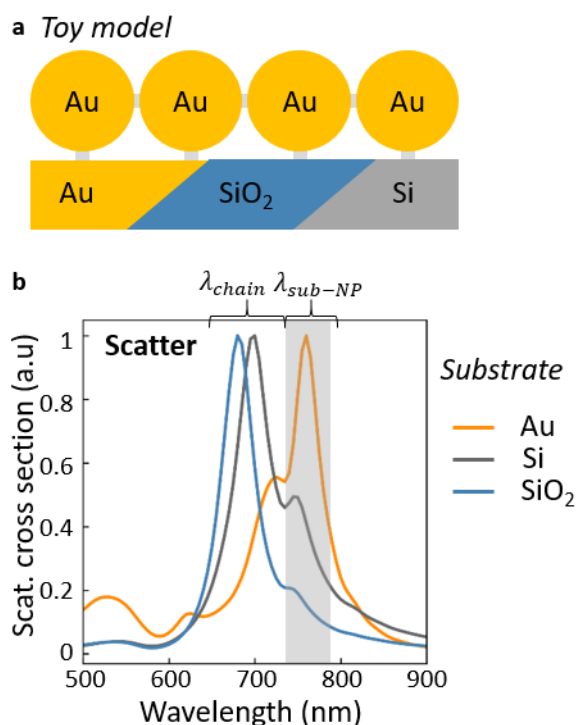


Fig. 4.12 **Toy Model System.** **a** Schematic of toy model of a four-nanoparticle chain spaced above Au, Si, and SiO₂ substrates simulated via finite-difference time-domain simulations. **b** Simulated scattering cross-sections calculated for schematic in a.

to match that of CB[7] [111]. Since it has been shown that only refractive-index changes in the immediate vicinity of the gap dominate results [43] CB[7] molecules surrounding the nanoparticle away from the gap regions have not been included. Due to computational constraints only four nanoparticles in a chain have been simulated, compared to the thousands formed experimentally. It is therefore expected that results produced here will be only indicative and blue-shifted from experimental results due to the well-studied red-shifts with increasing chain length [112].

The simulated far-field scattering spectra for each system can be seen in Figure 4.12b. The intensity scale is normalised to the maximum value for each system, so comparisons between absolute values for each system cannot be made; however the relative heights of different modes within a system can give valuable information. The ‘chain’ mode (λ_{chain}) for the 4 nanoparticles can be seen for each system lying in the 680-725 nm region. For the aggregates on gold, there is a strong mode at 760 nm (λ_{sub-NP}), arising from the coupling of the aggregate to the gold substrate. Although not seen in the experimental dark-field scattering results in Figure 4.11b,c, it can be seen that on both the Si and SiO₂ substrates there is a weak coupled mode, which is dwarfed by the relatively much bigger chain mode.

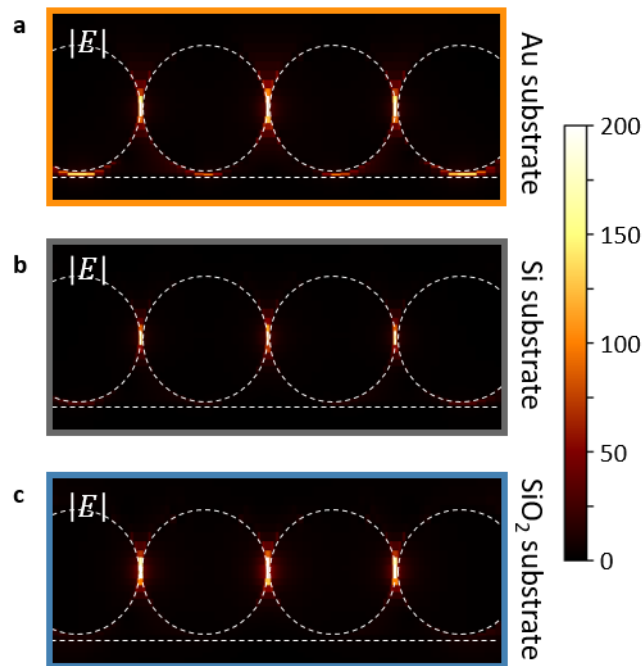


Fig. 4.13 **Magnitude of E field.** FDTD simulations showing $|E|$ surrounding a four-nanoparticle chain spaced 0.9 nm above an infinite substrate of **a** Au, **b** Si, and **c** SiO₂. Each is shown for the relevant resonant wavelength and colour scales are identical.

It is likely therefore that in the experimental spectra we observe only the chain mode for both Si and SiO₂, hence the homogeneity, whereas for the Au substrate we observe a mixture of both the chain mode and the higher-order coupling modes. The coupling of aggregate to substrate will vary with configuration and distance to substrate, hence the large variety of Au-substrate coupled modes observed in experiment (Figure 4.11a.). The spectral positions of λ_{chain} on Si and SiO₂ are very similar to each other, as observed in experiments, however in simulations it is found to be in the reverse order. Since only a sample of positions are measured experimentally across the aggregates in Figure 4.11b,c, this difference is not statistically significant.

Figure 4.13 shows the magnitude of the E field across the three systems. The NP-NP hot-spots of the chain mode can be clearly seen in all three cases. There is a clear hot-spot of slightly reduced intensity at the gap between the aggregate and substrate for the case of the gold substrate, but this is reduced to barely visible levels for the Si and SiO₂ systems.

The near-field spectra are extracted for all three systems at both the NP-NP junction and the substrate-NP junction, whereby the second nanoparticle in the chain is analysed for each realisation. At the substrate-NP junction (Figure 4.14d,e,f), the near-field spectra show much higher gap field intensities with the gold substrate when compared to the other two

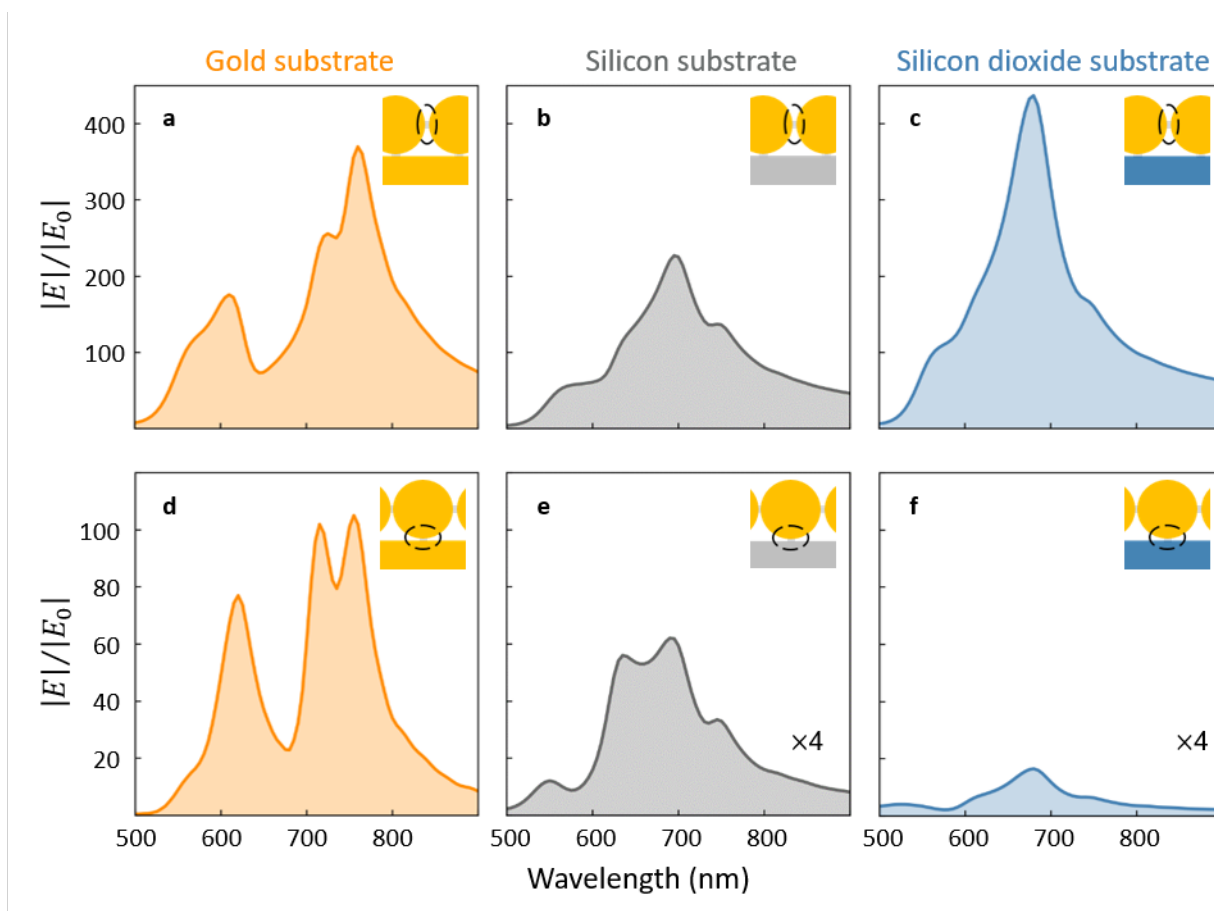


Fig. 4.14 **Extracted Near-Field Spectra.** Near-field spectra extracted from **a-c** nanoparticle-nanoparticle junctions and **d-e** substrate-nanoparticle junctions for each of the 3 substrate systems.

systems. Indeed, this enhancement is often used for single nanoparticles on Au substrates (NPoM configuration, Section 2.2.3). By contrast the NP-NP junctions in aggregates on SiO₂ and Au have comparable near-field intensities, with Si again weaker due to absorption (Figure 4.14a,b,c). Additionally, the field intensities in NP-NP junctions are much stronger than the substrate-NP junctions in all cases, suggesting that for dried aggregate geometries the field between the nanoparticles is largely responsible for field-enhancement processes such as SERS, confirming what was indicated by the intensities of SERS maps in Figure 4.7.

Both experimental results and toy model simulations show that the interaction between adjacent nanoparticles dominates the optical response and field enhancements of nanoparticle aggregates. However it is also shown that absorptive materials can have adverse effects on the field intensities experienced and so careful choice of substrate is needed when designing a SERS sensing system.

4.4 Conclusion

In this chapter I have studied the light emission from long-chain nanoparticle aggregates. Such aggregates contain thousands of plasmonic hot-spots and as such are useful tools for plasmonic sensing, especially using surface-enhanced Raman spectroscopy (SERS). Here I look at plasmonic sensing both in bulk systems in solution, where the signals from each hot-spot add together to form a total signal, and also map across single aggregates anchored to a substrate. I first discuss how computational techniques such as principal component analysis (PCA) can be used to optimise the information gained from a concentration series of analytes in emitted SERS spectra. I then look in detail at the emission of SERS photons from dried aggregates formed by addition of CB[7] and how the intensity of these signals can be altered by choice of underlying substrate. Here I track a single CB[7] peak rather than using PCA in conjunction with analyte molecules. It would be interesting to repeat these mapping measurements using multiple molecules and PCA to distinguish between molecular binding sites. In addition to experimental mapping I simulate a ‘toy model’ of a nanoparticle aggregate composed of only four nanoparticles using a finite-difference time-domain package. From this I can show that although careful choice of substrate is indeed important, as shown experimentally, the resulting plasmon emission is dominated by the hot-spots between adjacent nanoparticles.

Chapter 5

Observing Picocavities at Room Temperature

In this chapter I move from looking at long-chain nanoparticle aggregates with many nano-junctions to the single nano-junction of the nanoparticle-on-mirror (NPoM) structure. Within this I go even smaller, and look at the single adatom movements on the nanoparticle surfaces, which form ‘picocavities’ of even smaller mode volumes than the NPoM. Such picocavities have been observed previously at cryogenic temperatures [18], and here I push the limits of continuous wave (CW) laser techniques to observe them at room temperatures. I begin to characterise elements of this picocavity system through statistical analysis on thousands of nanoparticle-on-mirror structures, analysed through surface-enhanced Raman spectroscopy (SERS). Results from this chapter have been published in [113].

Experiments in this chapter make use of the custom-built integrated Raman and dark-field spectrometer (laser wavelength 633 nm), as described in Section 3.1.2. This is necessary in order to measure dark-field scattering and Raman scattering on the same structures in quick succession.

5.1 Room Temperature Dynamics

SERS on a single-molecule level has been the aim for many in the community for the last 50 years [27, 28] and therefore, increasing the confinement of optical fields has been an essential part of this research. There are many techniques for forming nanoscale hot-spots, with a brief introduction to some of these given in Section 2.2.2. Nanoparticle aggregates, self-assembled to form thousands of hot-spots, have been discussed in Chapter 4. However although confocal imaging and statistical techniques can reduce the number of hot-spots measured at any one

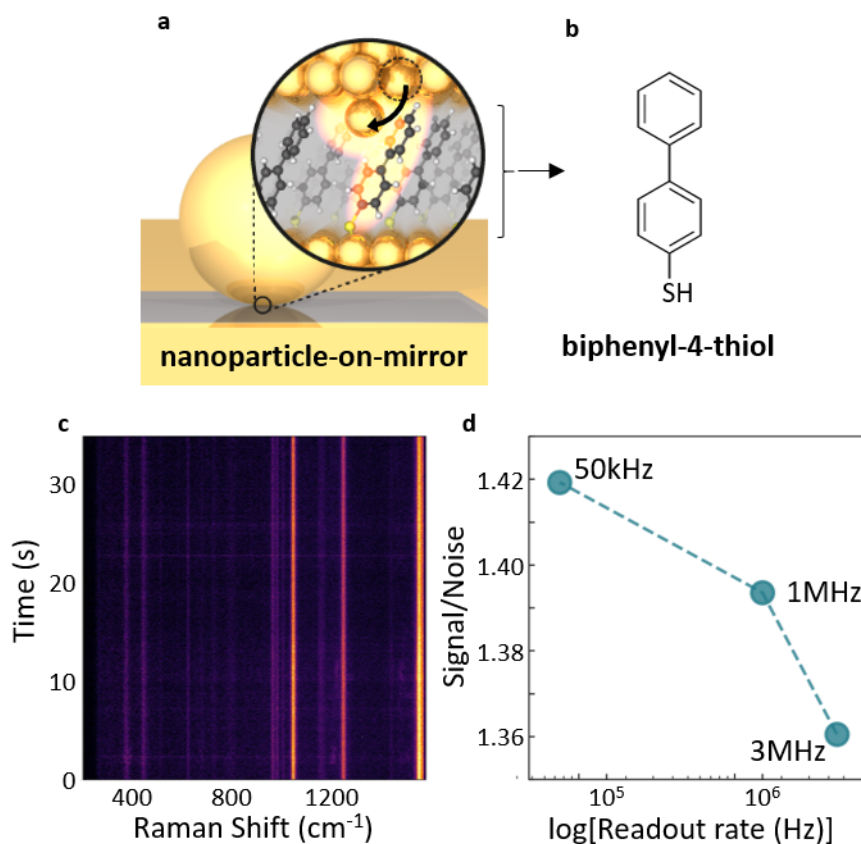


Fig. 5.1 **The NPoM system with BPT as a molecular spacer.** **a** Schematic of the nanoparticle-on-mirror system with a biphenyl-4-thiol (BPT) monolayer spacer. Inset shows adatom from nanoparticle creating a picocavity via an atomic scale lightning rod effect. Not to scale. **b** Chemical structure of biphenyl-4-thiol (BPT). **c** Example of ‘standard’ kinetic SERS spectra of BPT, recorded with 50 kHz CCD readout rate. **d** Overview of signal-to-noise ratio measured for each CCD readout rate.

time, there is still a large degree of averaging effects over multiple junctions and orientations, making the system not clean to study. In this chapter I will move down the confinement scale to look at an idealised individual junction with the nanoparticle-on-mirror (NPoM) structure. Introduced in Section 2.2.3, NPoM structures have been well-studied over the last decade [43, 80, 111, 114] as an analogue of a dimer structure, with a noble-metal nanoparticle inducing image charges in the underlying metal film. In this way nanocavities with optical mode volumes of 40-100 nm³ can be formed [18, 41]. The nanoparticle is separated from the film by a spacer, in this case a molecular monolayer of biphenyl-4-thiol (BPT), shown in Figure 5.1b.

It has been shown in recent work that within such nanocavities, a further level of optical confinement can occur [18]. Under laser irradiation a single metal adatom can protrude from the metal surface within the nanocavity, creating an atomic-level lightning-rod effect with the plasmonic field further confined around this adatom. Due to the subsequent reduction of field volumes to $\sim 1 \text{ nm}^3$ this has been termed a ‘picocavity’, a schematic of which is shown in Figure 5.1a.

A self-assembled monolayer (SAM) of biphenyl-4-thiol (BPT) is used as a molecular spacer in the NPoM system here due to its ability to form a robust and close-packed spacer layer [115–118], therefore excluding ions and impurities from the optically sensitive gap region. Because of this, the resulting kinetic SERS spectra are very clean and consistent in both peak intensity and peak position over time (example shown in Figure 5.1c), allowing for any small deviations from this norm to be measured and analysed more easily.

Picocavity formation leads to one such deviation from this norm (another: flare modes, will be discussed in Chapters 6 & 7). When a picocavity is formed, the single gold adatom leads to a further local enhancement of the optical field strength via the aforementioned lightning-rod effect [49]. This leads to a SERS enhancement factor > 200 , exceeding that of the ~ 100 other molecules in the nanocavity hot-spot and enabling observation of single-molecule SERS for BPT molecules in the picocavity volume. The picocavities also produce a strong field gradient across each bond within the single BPT molecule, breaking the selection rules that keep its IR-active modes dark in Raman and producing a whole new set of lines which are now visible in the emitted spectra (Figure 5.2b). The addition of new lines in the SERS spectra, which are visible also in the anti-Stokes due to the optomechanical pumping from the picocavity field, are now recognised as the characteristic signature of picocavity formation [18, 29]. Previously these lines had often been attributed to impurities in the system, but this cannot explain the high anti-Stokes spectral lines, which requires this extra degree of pumping to fill the excited vibrational states.

The existence of picocavities was previously shown in experiments carried out at cryogenic temperatures [18] (see description in Section 2.3.3). These conditions were needed to stabilise the adatom movements, which otherwise are fleeting at room temperatures. Here I show that by pushing the limits of CW laser spectroscopies to much shorter integration times, high-speed SERS can indeed resolve picocavity dynamics at room temperature.

The experimental details of the equipment used is detailed in Section 3.1.2. In order to ensure best observation of the system with low integration times, it is important to maximise signal-to-noise of the resulting spectra. Here I undertake an initial study at the three readout rates available with the Andor Newton CCD used for recording outcoupled Raman light. Having a higher readout rate enables shorter dead-times between subsequent spectra, but it can

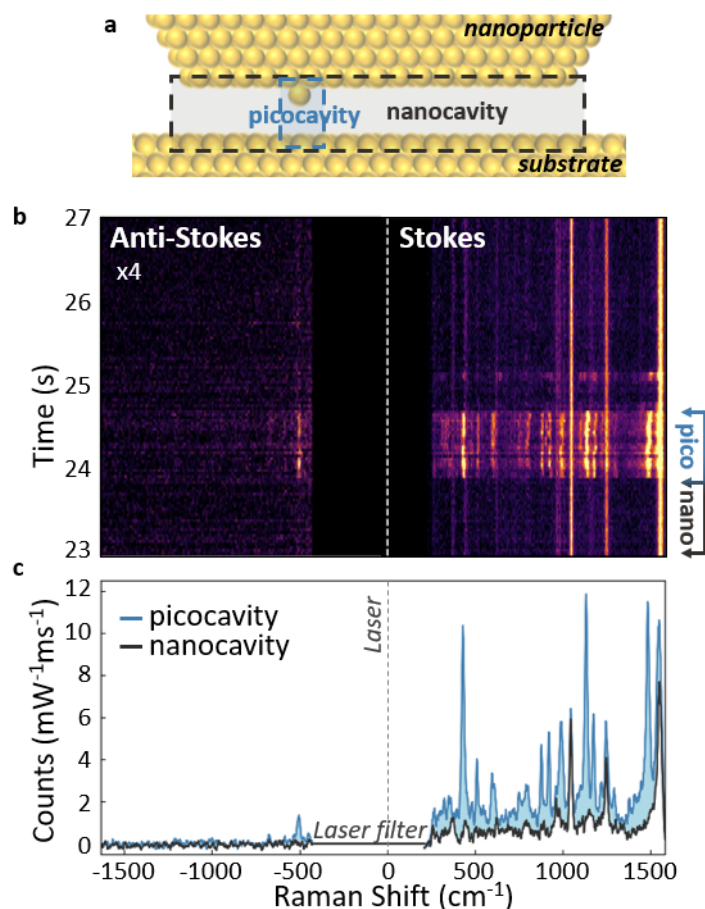


Fig. 5.2 Picocavities Observed at Room Temperatures. **a** Schematic of the gap region between the bottom nanoparticle facet and the metal substrate. Nanocavity and picocavity regions are labelled. **b** Kinetic SERS spectrum from an NPoM structure showing stable bulk BPT in a nanocavity (grey bracket on right) as well as a few-molecule picocavity event (blue bracket). Anti-Stokes (left) side multiplied by 4 for visibility. **c** Corresponding single SERS spectra from nanocavity and picocavity in (b).

be seen that this comes with the flip-side of a decrease in signal-to-noise ratio (Figure 5.1d). Although these differences are small, the peak intensity of signals becomes small enough that a low signal-to-noise ratio can completely obscure any result. As a result the ‘slowest’ readout rate of 50kHz is chosen to maximise signal-to-noise. This is then combined with ‘full vertical binning’ readout mode on the CCD, whereby all lines on the CCD are collapsed into one, rather than the more conventional cropping of vertical regions of interest. This has the effect of reducing the dead-time between subsequent spectra as much as possible, maximising temporal resolution, but adds the dark counts from all rows.

Automated particle-tracking methods (detailed in Section 3.1.2) are used alongside high-speed SERS in order to look at the characteristics of these picocavities. As a relatively new concept in the field, there is a huge amount of information still to be gathered on picocavities, in particular on the exact mechanism of formation. Here I show that useful statistical information can be gained through collection of large spectral datasets, enabling an initial study of room-temperature dynamics and properties to be made.

Using these automated methods, over 3000 NPoM structures are measured at room temperature, with 1000 high-speed SERS spectra recorded for each structure (>3 million spectra total), alongside metadata including dark-field images and spectra allowing for full characterisation of each NPoM. Figure 5.2 shows an example of picocavity event observed using these high-speed SERS techniques (more examples can be seen in Appendix B). The typical fingerprint of persistent lines originating from bulk BPT in the nanocavity (Figure 5.2a) can be seen consistently on the Stokes (right-hand) side of the spectra. A representative spectrum is shown in grey in Figure 5.2c. Picocavity events are recognised by the multitude of extra lines that transiently appear across the spectra for short bursts (here at times between 24 – 25 s). Previous measurements with typical 1 s integration times would average over the entire picocavity lifetime, but here 4 cm^{-1} spectral wandering can be observed. A single spectrum from this picocavity event is shown in blue in Figure 5.2c. It can be seen that although the vibrational modes from the nanocavity are not visible in the anti-Stokes (left) side of the spectrum, low Raman shift modes from the picocavity are weakly observed, as previously reported.

5.1.1 Picocavity Mode Positions

As described in Section 3.2, I have developed methods with which I can auto-detect picocavity events and from there extract all peak positions from those spectra at which a picocavity event is determined to have occurred. A histogram of all these peak positions is shown in Figure 5.3 for 172 picocavities. The nanocavity spectrum of BPT with no picocavity field gradients is shown on top in grey. The dashed lines in the histogram show the three main BPT nanocavity vibrations. These correspond to a ‘C-H rocking’ at 1079 cm^{-1} , a ‘coupled ring stretch’ of the benzene rings at 1281 cm^{-1} , and degenerate ‘ring stretch’ of each of the rings at 1586 cm^{-1} [18].

Although picocavity lines are detected across the spectral range, there is a higher concentration of picocavity modes in the region between these high Raman-activity vibrations, suggesting that they are somehow related to these bonds. It has been suggested in previous work [18] that the picocavity lines arise from a breaking of symmetry due to the field gradient produced from the adatom lightning-rod effect, thus enabling observation of previously

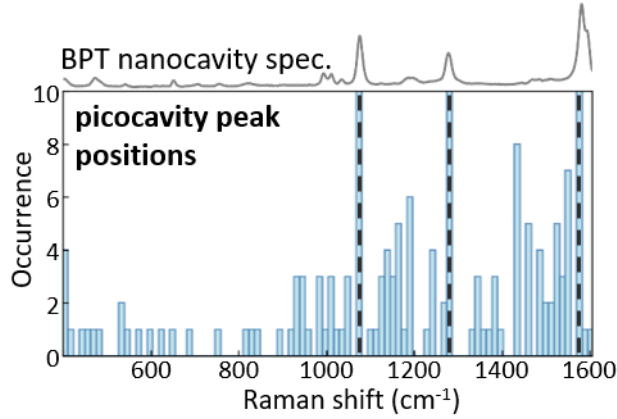


Fig. 5.3 **Picocavity Mode Positions.** Extracted peak positions from all picocavities collected in dataset. Grey spectrum on top panel shows a BPT nanocavity spectrum in the absence of any picocavity. Dashed lines below show the 3 major nanocavity modes.

dark IR modes. Although to the best of my knowledge, there are no experimental studies on the infrared modes of BPT, an interesting avenue of research would be to undertake surface-enhanced infrared absorption (SEIRA) measurements to see if the results can be corroborated. If so this would introduce a new technique for artificially building an IR spectrum from scattering measurements.

5.1.2 Temperature Trends

As described in 2.3.1, the anti-Stokes (AS) scattering process requires the molecule to already be in an excited vibrational state, whereas the Stokes (S) process starts from a ground state and therefore has no such population dependence. Therefore, assuming a Bose-Einstein energy distribution, the Stokes:anti-Stokes ratio R can be used to calculate an effective molecular temperature, T_{eff} from

$$R = \frac{I_{AS}}{I_S} = \exp \left[-\frac{hc}{k_B T_{\text{eff}}} \left(\frac{1}{\lambda_{laser}} - \frac{1}{\lambda_{mode}} \right) \right], \quad (5.1)$$

where $I_{AS,S}$ are the peak intensities of the equivalent AS and S modes respectively, and $\lambda_{laser,mode}$ are the wavelengths of the excitation laser and Stokes vibrational mode. T_{eff} is the effective temperature, so-called since it characterises the temperature required to achieve the excited state population in the absence of any pumping. It is important to note that in the case of picocavities, the effective temperature is not indicative of a thermal temperature, since the population is pumped by optomechanical coupling of the molecular vibrations to

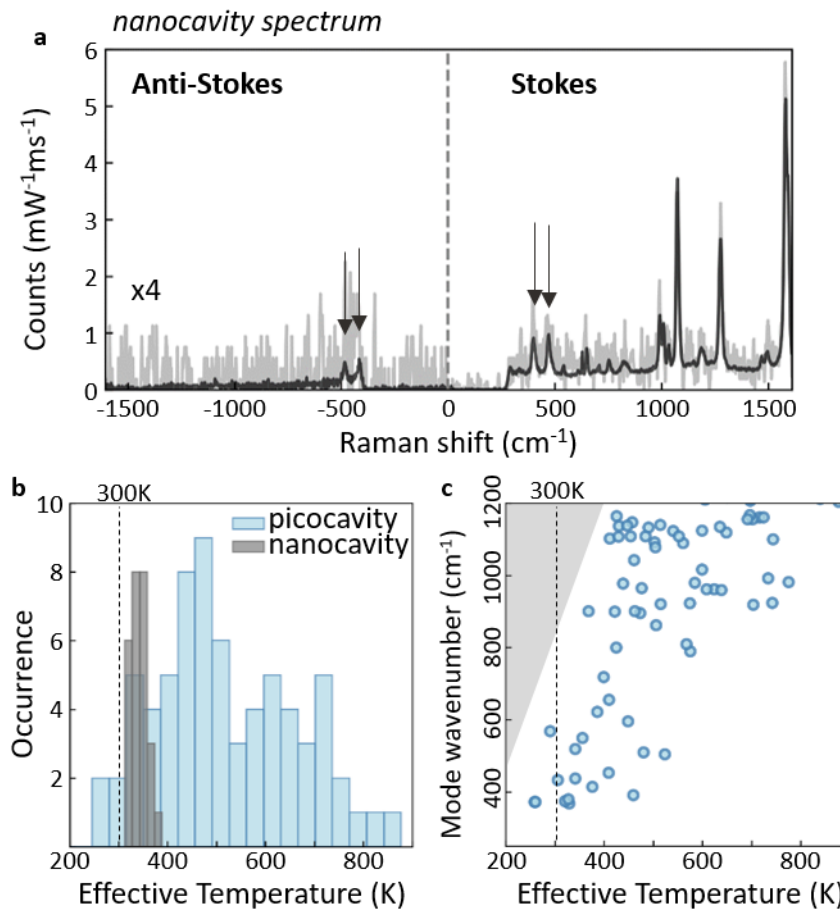


Fig. 5.4 Nanocavity and Picocavity Temperature Trends. **a** Example nanocavity single spectrum (light grey) with anti-Stokes lines impossible to pick out from the noise, compared to time-averaged over 30 s (dark grey) showing the low-wavenumber persistent peaks on both Stokes and anti-Stokes side, enabling calculation of temperature. Arrows denote modes used for temperature calculations. Anti-Stokes (left) side of spectrum multiplied by 4 for visibility. **b** Extracted effective temperatures for both picocavities and nanocavities, collected from > 1000 NPoM constructs. **c** Correlation between the effective temperature of the picocavity and the wavenumber of the vibrational mode in which it is estimated. Grey region is below the signal-to-noise limit.

the intense plasmon formed at the adatom, rather than thermal effects as the name suggests (see Section 2.3.3 for details).

The effective temperature is thus calculated for each picocavity event as well as each corresponding nanocavity. The local temperature of the surrounding SAM nanocavity molecules is calculated from the ratio of the persistent lines. Since there is no optomechanical pumping of these modes, longer time averages of > 30 s are required in order to have sufficient signal-to-noise ratio to extract AS peaks (Figure 5.4a).

The distribution of effective temperatures can be seen in Figure 5.4b. The nanocavity has a narrow distribution of temperatures across all NPoMs analysed, with an average temperature of 341 K, a reasonable value for temperature within the hot-spot under laser irradiation. In comparison, the effective temperatures extracted from picocavity lines show a much broader, hot distribution. This suggests that although NPoM structures are a fairly reliable method for forming consistent hot-spots, there are a variety of picocavity geometries that can form, with a range of vibrational coupling strengths arising from the range of adatom-molecule distances.

The single-molecule effective vibrational temperatures extracted from room temperature picocavities (400-800 K) are much lower than those previously extracted at cryogenic temperatures (> 1000 K) [18]. It is likely that this is due to the increased thermal depopulation of phonons by nonlinear phonon-phonon scattering when greater thermal vibrational backgrounds are present [119, 120].

A strong correlation (Pearson coefficient = 0.7) is found between the energy of the vibrational mode and the effective temperature calculated. This is shown clearly in the scatter plot in Figure 5.4c. Since the effective temperature gives a measure of the excited-state population pumped via optomechanical coupling, this suggests that the higher-wavenumber (lower-energy) vibrations overlap better with the plasmon in the gap.

5.2 Breaking Molecular Symmetry in the Gap

To further analyse picocavity dynamics at room temperature we slightly alter the BPT molecule, instead using one which has a cyanine tail group, known as 4'-cyanobiphenyl-4-thiol (NC-BPT, chemical structure shown in Figure 5.5d)¹. During NPoM fabrication the thiol head group binds to the flat gold surface as before, due to the strong Au-SH bonds. This leaves the cyanine group ($N\equiv C$) on the nanoparticle side of the gap, thus breaking the symmetry in our molecular gaps. The $N\equiv C$ bond (affected by adatoms protruding from the nanoparticle) has vibrations that are lower in wavenumber than the thiol and ring modes (affected by substrate adatoms). In this way we can now distinguish between picocavity spectra which originate from either nanoparticle or substrate surface. Particle-tracking methods are once again employed to measure ~ 2500 nanoparticles each for 1000 consecutive spectra, and picocavity spectra are sorted into one of the above two categories (Figure 5.5a-c).

Although a mechanism or explanation is unclear, it is also found that picocavity events last up to $10\times$ longer within this structure compared to those with a BPT spacer. It is likely

¹The work in this section was undertaken alongside Jack Griffiths, Nanophotonics Centre, Cambridge, UK, who carried out the experiments in Section 5.2.

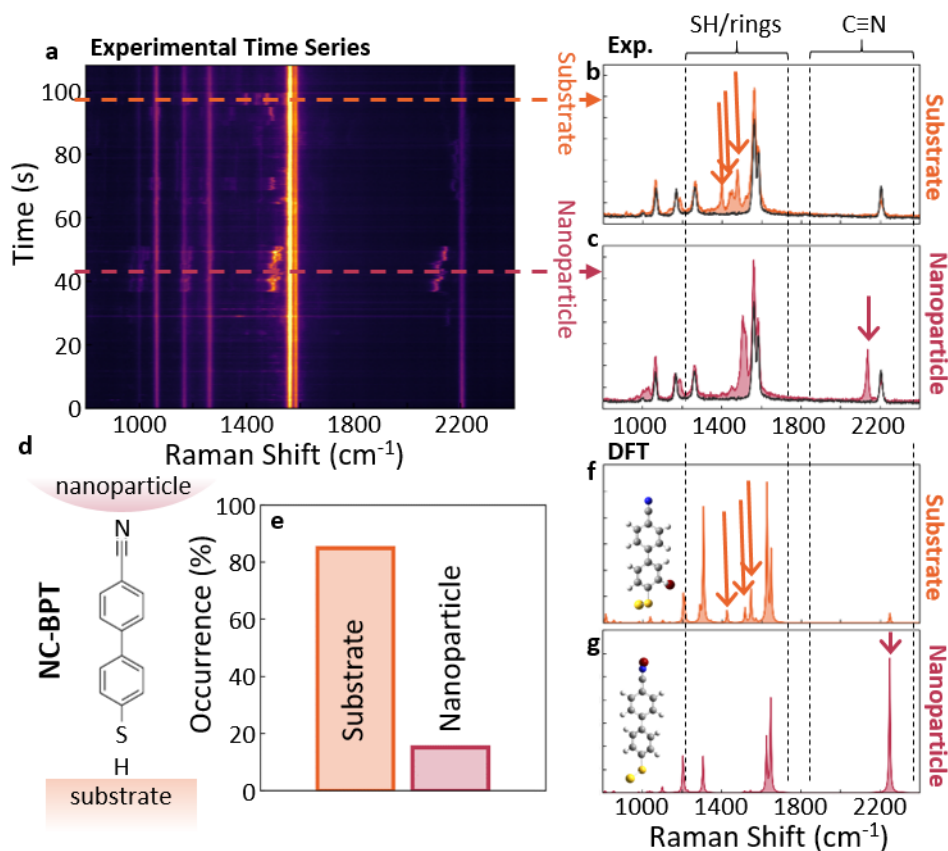


Fig. 5.5 Breaking Molecular Symmetry in the Gap. **a** Experimental time-series SERS spectrum from NPoM with a NC-BPT spacer. Persistent lines from bulk NC-BPT in the nanocavity are seen as well as picocavities originating from substrate adatoms (dashed orange) and nanoparticle adatoms (dashed pink). Corresponding individual spectra for **b** substrate picocavity and **c** nanoparticle picocavity. **d** Chemical structure of 4'-cyanobiphenyl-4-thiol (NC-BPT), with simplistic schematic showing how thiol group (SH) attaches to the substrate and cyanine group ($\text{N}\equiv\text{C}$) to the nanoparticle. **e** Relative percentage occurrence of each type of picocavity, measured from over 2500 NPoM structures. **f,g** Density functional theory (DFT) simulations for vibrational spectra predicted when gold adatom placed at bottom and top of molecule to simulate substrate- and nanoparticle-adatom picocavities, respectively. Inset shows simulated structures, red dot represents Au adatom.

that this is a result of changes in packing density or additional quasi N-Au bonds forming between the top of the SAM and the nanoparticle, but further studies are needed to ascertain this. As a result of this increase in picocavity lifetime, it is possible to correspondingly increase the integration time of SERS spectra recorded.

Examples of substrate-originating and nanoparticle-originating picocavity spectra can be seen in Figure 5.5b,c. The allocation of spectral groups is corroborated with density

functional theory (DFT) simulations². These are carried out for an individual NC-BPT molecule, with a gold adatom (shown in red in inset) placed either at the top or bottom of the molecule (Figure 5.5f,g). Although the DFT spectra do not entirely match those from experiments, it is clear that a nanoparticle Au adatom placed near the C≡N bond leads to changes in the $> 2000\text{ cm}^{-1}$ region and substrate Au adatoms will instigate spectral changes in the $1200\text{-}1500\text{ cm}^{-1}$ region. It should be noted that picocavities originating from a nanoparticle adatom can also affect the ring modes, but adatoms from the substrate do not affect the N≡C modes.

By auto-sorting picocavity spectra into these two groups, the relative likelihood of each class can be calculated (Figure 5.5e). The inhomogeneity in probability can be clearly seen, with picocavities originating from substrate considerably more frequent. This adds evidence to the suggestion that the molecular structure and bonding of the SAM in some way controls the likelihood of the picocavity adatom, but it is clear that a better understanding of the exact mechanism is needed.

5.3 Conclusion and Outlook

In this chapter I have moved from looking at large nano-aggregates with many plasmonic hot-spots to single junctions produced via the nanoparticle-on-mirror structure. Within these structures ‘picocavities’ are spontaneously formed by irradiation from an incident laser. These are regions of additional confinement formed by atomic-scale lightning-rod effects of single gold adatoms on the surface of either the nanoparticle or the mirror. I have shown here that it is possible to observe picocavities at room temperature using CW laser excitation methods and that statistical information can be extracted by measuring thousands of NPoM structures in a single experiment. I have begun by analysing the spectral variation in position of picocavity lines as well as studying their effective temperatures. In order to go some way into an initial understanding of what processes and conditions prompt formation of a picocavity, I describe here a study in which we break the symmetry of the molecule in the gap, enabling determination of whether the picocavity adatom originates from the nanoparticle or the mirror; and finding a systematic inhomogeneity. From here further study is needed. It appears from the literature that thiols have particularly strong interactions with gold atoms, thus producing numerous picocavities, but it could also be the case that there are differences

²DFT simulations are carried out by Yao Zhang, Materials Physics Center CSIC-UPV/EHU and Donostia International Physics Center DIPC, Donostia-San Sebastian, Spain. Simulations carried out using G16 (B3LYP/def2TZVP)

in lattice planes of gold between the bottom facet of the gold nanoparticle and the mirror formed by template-stripping.

Chapter 6

Broad-Band ‘Flare’ Events

In this chapter I move from talking about picocavity spectra, which have known origin, to a new class of spectral feature that is observed when collecting time-dependent SERS spectra from nanoparticle-on-mirror structures. These ‘flare’ modes appear fleetingly as a broad-band Gaussian background increase and have been observed consistently over the past two decades in single-molecule SERS studies [27–30, 66] although a thorough statistical investigation into their origin has not been carried out. A large number of studies discount these modes completely, putting them down to equipment fluctuations. Weiss et al. [30] attribute their observations of this to "motion of the adsorbed molecule on the surface, triggered by photodesorption events that are mediated by electron tunnelling between the molecule and surface". Cheng et al. [66] instead attribute the increased background they observe to "an induced field of the molecules, which increased the local field felt by the surrounding nanostructures". However the systems used in these experiments were quite different to those used in these thesis, with Weiss et al. utilising dye molecules alongside nano-crystals and Cheng et al. using a large aggregate of nano-flowers. Both of these lead to additional contributions and instabilities to the systems, making it harder to isolate the background increases.

Here I show that there are clear trends between different spacer molecules evidencing that they are indeed a physical effect. In this chapter I collect statistical information on the flare modes by analysing thousands of nanoparticle-on-mirror structures and looking at the temporal, spectral and power-dependent characteristics. In the following chapter I will put forward and evaluate a number of suggestions for the origin of flare modes and what this can tell us about the NPoM system.

As in Chapter 5, the experiments in this chapter make use of the custom-built integrated Raman and dark-field spectrometer, as described in Section 3.1.2.

6.1 Observation of Flare Modes

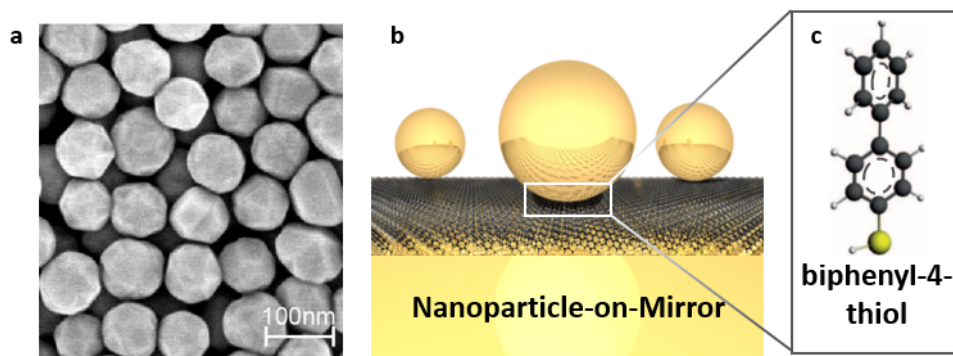


Fig. 6.1 **Nanoparticle-on-Mirror Structure for Single Hot-Spot Analysis.** **a** SEM images showing the distribution in geometry of ‘spherical’ nanoparticles used in NPoM constructs. **b** Schematic of nanoparticle-on-mirror construct with self assembled monolayer of **c** biphenyl-4-thiol (BPT).

Here I stay with the nanoparticle-on-mirror (NPoM) construct as a system for analysing single plasmonic nanojunctions. As mentioned in Chapter 5, biphenyl-4-thiol (BPT) is a very useful molecular spacer when looking at spectral abnormalities due to its temporally consistent nanocavity SERS spectra (as seen in Figure 5.1c). This enables good statistical characterisation of additional inelastic processes that may also be occurring in the vicinity of the nano-gap. The structure of the nanoparticle-on-mirror system can be seen in Figure 6.1. BPT is used as a molecular spacer for most of the in-depth analysis, although this is compared to other molecular spacers in Section 6.3. It is emphasised that although presented as spherical, the nanoparticles used have a myriad of crystalline shapes, as observed in the SEM image in Figure 6.1a. These shapes are not all monocrystalline and nanoparticles are known to contain multiple grain boundaries and crystal defects, as briefly introduced in Section 2.5 [75]. All these defects will alter the local plasma frequency in the immediate vicinity [121]. As well as crystallinity boundaries and defects, it has been shown that the crystallinity of nanoparticles is not entirely fixed and constant, but instead it is open to movement [122–124]. This is now known as the ‘quasi-molten’ model of nanoparticles.

As previously mentioned, the close-packing nature of self-assembled monolayers (SAMs) excludes any impurities from the hot-spot region and leads to a set of stable, high-intensity Raman lines, with minimal spectral wandering over time. This can be seen in Figure 6.2b. Aside from picocavities, which lead to additional sharp peaks appearing in both the Stokes and anti-Stokes spectra (discussed in depth in Chapter 5), another spectral feature can occasionally be observed. In this event, which we will herein term a ‘flare event’, there is a

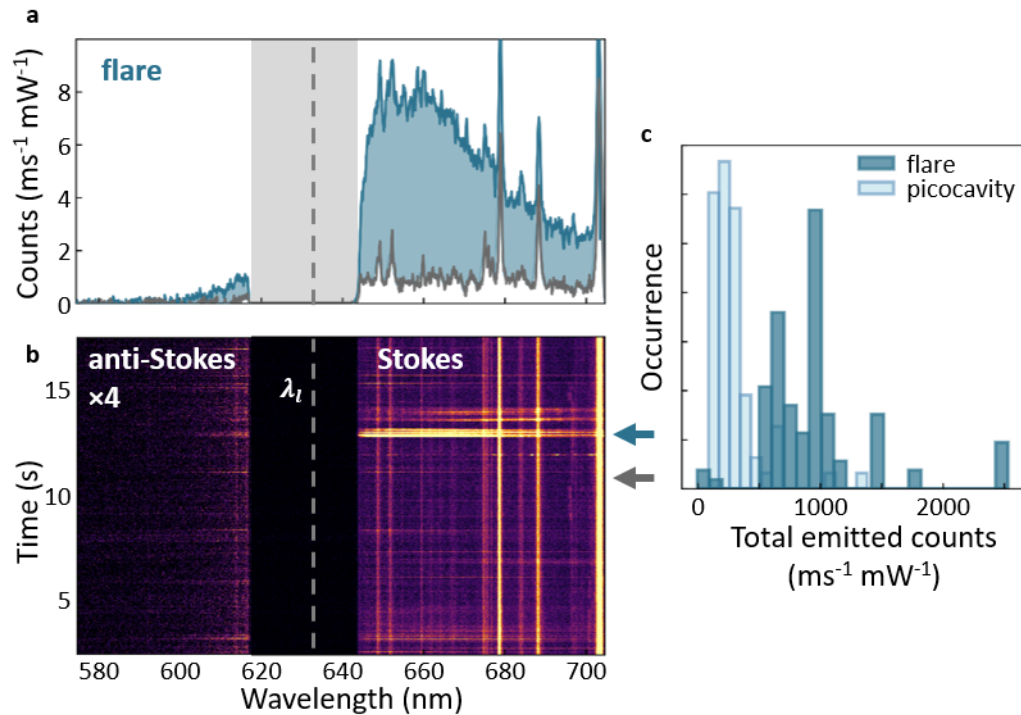


Fig. 6.2 **Observation of Flare Modes.** **a** Inelastic scattering spectra showing example flare mode (blue) compared to ‘standard’ BPT nanocavity spectrum from the same NPoM construct. Grey shaded region indicates laser filter, dashed line is laser wavelength (632.8 nm). **b** Kinetic spectra showing time dynamics of multiple flare spectra. Anti-Stokes (LH) side multiplied by 4 for visibility. Arrows denote flare and nanocavity spectra from (a). **c** Histogram showing total emitted counts for picocavity spectra compared to flare spectra for the same sample of NPoM constructs.

sudden emergence of a Gaussian-shaped background, lasting for only fractions of a second. An example time-series showing of a number of these events is shown in Figure 6.2b, with individual time-slices at the flare event (blue) and non-flare event (grey) shown in Figure 6.2a. Unlike picocavity lines, which are mirrored around the laser wavelength in the anti-Stokes, the peak of this flare mode is on the Stokes side and has a tail that extends into the anti-Stokes, but with no inversion symmetry around the laser line. By analysing ~ 100 flare events and summing the total emitted counts per unit time, the number of a photons emitted during a flare event is found to be roughly double that for picocavity events in the same dataset (Figure 6.2c) suggesting a difference in scattering efficiencies between the two events.

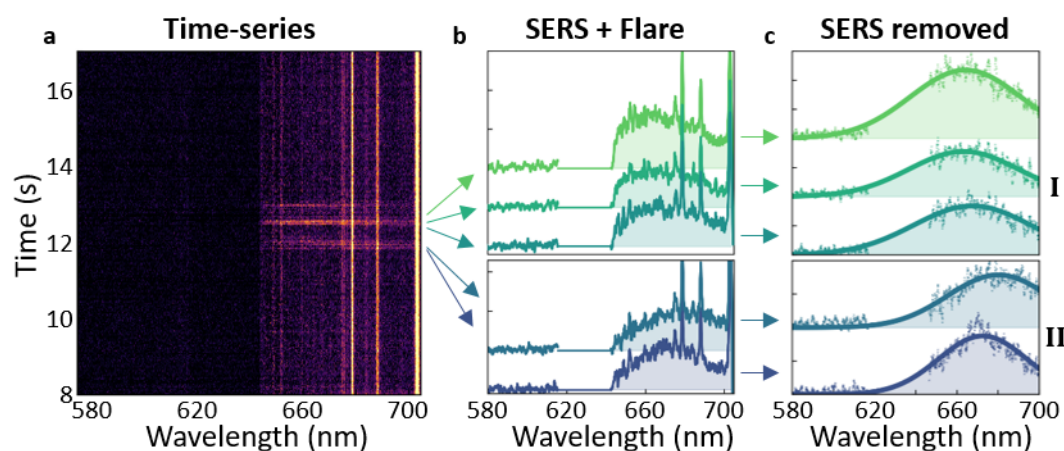


Fig. 6.3 **Gaussian Lineshape of Flare Modes.** **a** Example kinetic time-series showing flare events recorded alongside BPT SERS peaks. **b** Extracted spectra for which a flare event is occurring, showing both the SERS peaks and flare background. Flat line indicates laser filter region. **c** Flare modes from (b) with SERS contribution removed. Solid line shows Gaussian fit. Separated into I and II clusters from Figure 6.4b.

6.2 Multi-NPoM Analysis

Since the flare events are relatively rare and too fleeting to stabilise, automated particle-tracking experiments are carried out in order to collect statistics on their characteristics, with the hope of providing clues towards their origin (methods detailed in Section 3.2). Millions of NPoM structures are formed on a single sample, which can each be measured in turn. For each NPoM, 1000 spectra are taken in a fast kinetic series, each with a cycle time of 0.035 s. Autodetection code is run in order to pick out each occurrence of a flare mode (full details are given in Section 3.2). A single NPoM example time-series can be seen in Figure 6.3a, with b showing the extracted spectra containing flare events.

To further analyse the shape of the flare modes, the first SERS spectrum in the time series is subtracted from all the subsequent spectra in its series, leaving a zero for ‘normal’ events and an intensity increase for flare events. The resulting flare modes can be seen in Figure 6.3c, and are fit to a Gaussian profile. The origin of these flare modes is currently unknown, therefore herein they will be referred to as ‘inelastic scatter’. An interesting point to note is that although they clearly vary in spectral width and position, the flares shown in this example all occur within one kinetic scan of a *single NPoM structure*, demonstrating that their Gaussian lineshape can vary within the 35 s observation window of an individual construct.

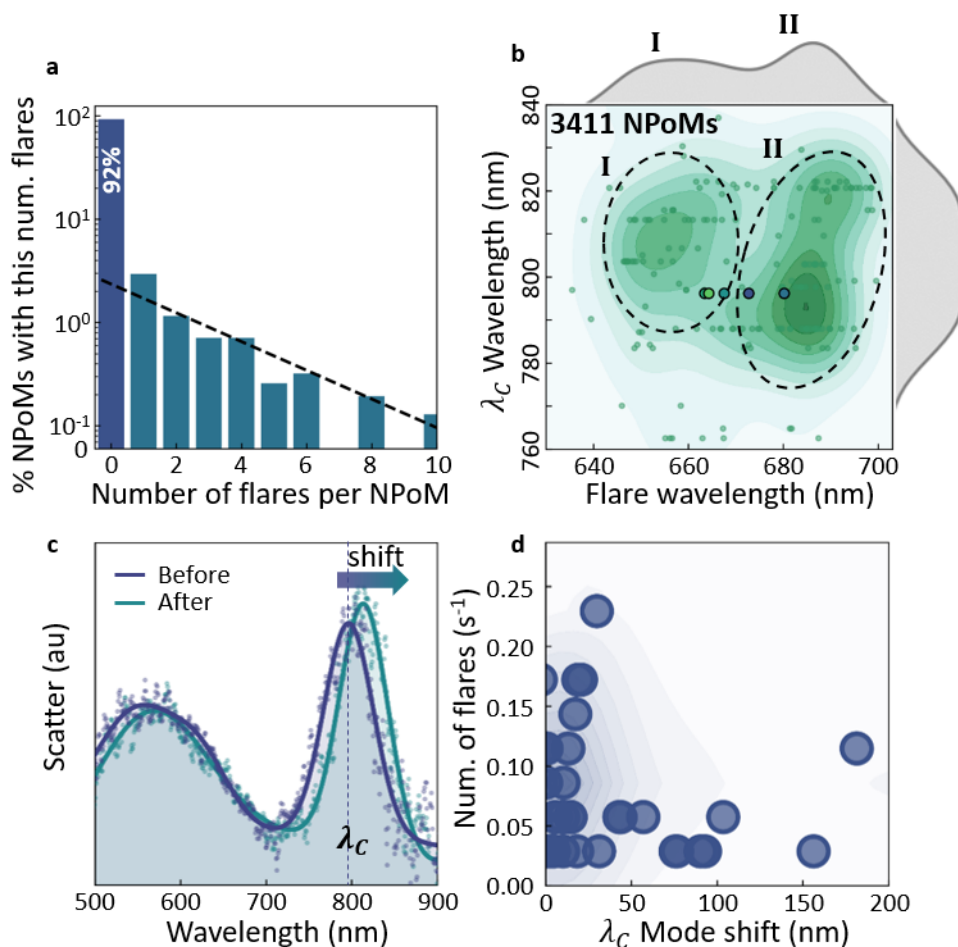


Fig. 6.4 Occurrence Statistics of Flares. **a** Fraction of NPoM structures showing different number of flares, shown on log-lin axes. **b** Density map of plasmon coupled-mode wavelength λ_C against flare mode centre wavelength for flares from 3411 NPoMs. Dashed line circles two identified clusters. Grey curves top and right show individual distributions. Points corresponding to spectra in Figure 6.3 are circled. **c** Example dark-field scattering spectra taken before (purple) and after (green) laser irradiation, showing slight λ_C red-shift. **d** Number of flares observed plotted against the coupled-mode shift observed. Scatter plot is plotted over a density map of the same distribution. Pearson coefficient of -0.24 calculated, indicating no correlation.

As previously mentioned, the emergence of these flare modes is relatively rare, complicating their analysis. This is quantified in Figure 6.4a, with 92 % of NPoMs studied showing no flare events at all within the 35 s time window. There can be seen to be an exponential distribution in number of flares seen after that (straight line on log-lin axes). This suggests that although there is an exponential probability distribution for those nanoparticles showing flares in the time-window, there are some nanoparticles which will never show any

flare events. The fact that only 8 % of nanoparticles show any flares at all underlines the need for automated tracking experiments and well-grounded statistics. Here I measure over 3000 NPoM constructs. As well as collecting inelastic-scattering measurements via laser irradiation such as those in Figure 6.3, dark-field (elastic) scattering measurements are also taken which elucidate the plasmonic modes of the NPoM before and after laser irradiation. The distribution in plasmonic modes measured in this way can indicate the range in nanoparticle size (and geometry) across the sample (see Section 2.2). To survey the range of flares detected, a density map of the fitted flare wavelength *vs* NPoM coupled-mode wavelength (λ_C) is plotted for all NPoMs (Figure 6.4b). It can be clearly seen that although there is a roughly mono-normal distribution in λ_C of NPoMs analysed as expected, there is a clear bi-modal distribution in flare wavelengths. This suggests that information is contained in these flare modes which is not unpacked in standard elastic dark-field scattering experiments. I here label these two cluster groups I and II. It is interesting to note that single NPoM constructs can show flare events of both types within a few seconds, demonstrated by the examples from Figure 6.3 circled in black in Figure 6.4b. This suggests that the flare events are not entirely nanoparticle-dependent.

Dark-field scattering has also been shown to be highly informative in revealing morphological changes to the NPoM constructs. This is particularly the case with the coupled mode λ_C , which has been shown to red-shift strongly with an increase in bottom facet width linked to nanoparticle damage from sufficient laser irradiation [114, 48, 46]. An example of dark-field scattering spectra from before and after the laser irradiation is shown in Figure 6.4a. Although a small red-shift is indeed observed, as expected, it can be seen that the 35 s of laser irradiation required for the inelastic scattering measurements is not sufficient to cause significant damage to the construct. This is the case for the majority of NPoM structures measured (74 % of NPoMs show λ_C shifts of less than 100 nm).

Nevertheless a degree of mode shift (and therefore damage) is indeed seen, with a very small number of cases of shifts up to 200 nm observed (Figure 6.4c). This amount of shift, although considerable, is relatively rare. It is likely that in these cases the nanoparticle is almost completely destroyed, and so is perhaps not that useful to consider. The differences in damage observed for different NPoM structures experiencing the same laser irradiation is not completely understood, but it is thought that the variation in damage is due to the variation in incoupling efficiency of light for non-identical nanoparticles.

The facet increase indicated by λ_C requires movement of surface atoms on the nanoparticle and so it is reasonable to suggest that if the flare event is related to nanoparticle geometry changes then the same process that leads to a higher degree of damage could also lead to a flare event. Figure 6.4c shows the correlation between the coupled-mode shift from before

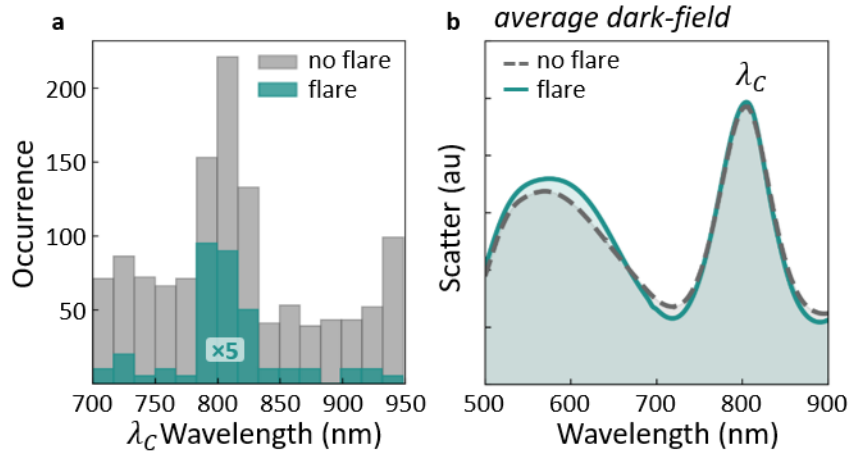


Fig. 6.5 **Plasmonic Mode Comparisons.** **a** Distribution of coupled-mode wavelengths measured via dark-field scattering, and **b** average dark-field scattering spectra for nanoparticles which show no flares (grey) and those which show at least one flare (green).

to after laser irradiation and the number of flares observed on that same NPoM structure. However the Pearson coefficient of -0.24 indicates close to no correlation. However it could be argued that instead there are two distinct populations of linear correlations, similar to the dual populations seen in Figure 6.4b. A similar lack of correlation is also observed between the duration of the flare event and the degree of redshift of the coupled-mode (Pearson coefficient of 0.13 , not pictured).

I can also compare plasmonic features of the NPoM structures which give rise to flares and those which do not, to see if the plasmonic modes can give clues to the possibility of a flare event occurring. Figure 6.5a shows the distribution of coupled mode wavelengths for the two cases. Figure 6.5b instead looks at the mean spectral shape for each case. Both give resoundingly near-identical results for the flare- and non-flare case, even if only the nanoparticles with $790 < \lambda_C < 830$ are considered, therefore clearly further analysis is needed.

6.2.1 Power-Dependent Measurements

The first step to understanding the physical process behind flares modes is to determine if their occurrence is light-activated. For picocavities this can be achieved by dynamically reducing the laser power to stabilise the cavity [18], however due to the fleetingly short nature of flare events, this is not possible. Instead, the effect of average power on the flare frequency and life-time can be determined by performing a power-series experiment. Here ~ 500 NPoM structures are analysed at each power, each for a period of 35 s (as before).

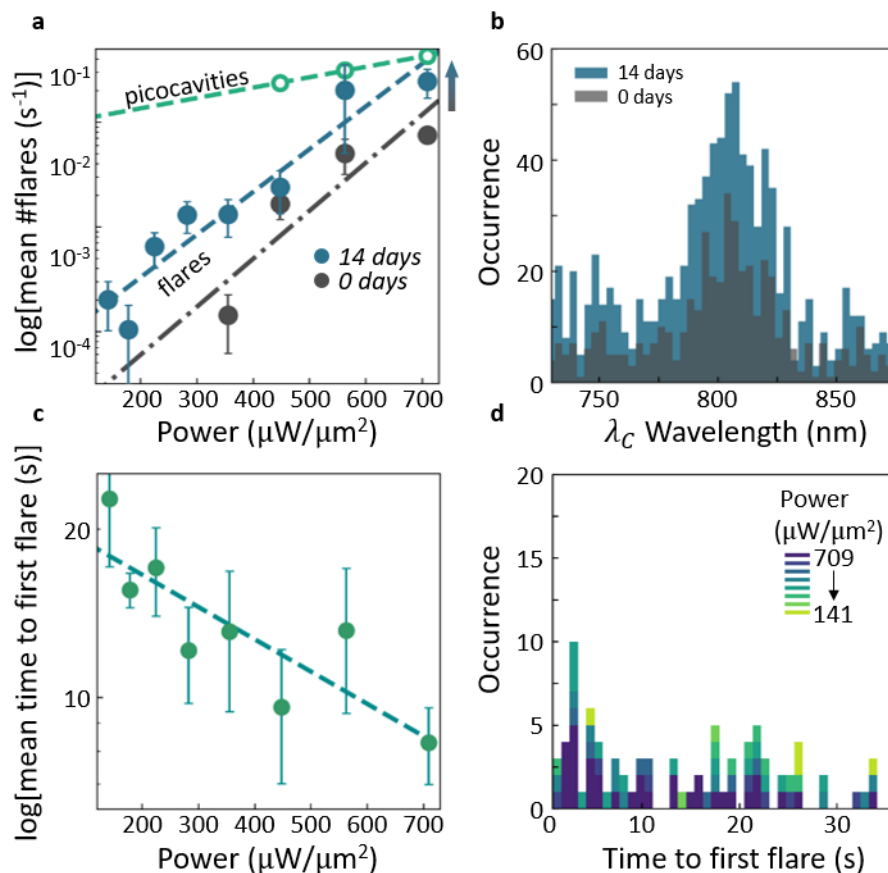


Fig. 6.6 Power Dependent Analysis of Flare Modes. **a** Mean number of flares per s vs incident laser power, for NPoM samples measured immediately after self-assembly (grey) or after 14 days in air at 300 K (blue), plotted on log-linear axes. Green shows equivalent analysis for picocavities. Here 500 NPoMs are surveyed for each power, lines show exponential fits, and error bars indicate standard deviation in the mean. **b** Histogram showing the distribution of coupled-mode wavelengths (λ_C) for both the sample at 0 days (grey) and at 14 days (blue), indicating that although there are changes to the number of flares observed, the coupled-mode is unchanged. **c** Mean time after laser turned on before first flare mode detected vs incident laser power, plotted on log-linear axes. Line shows exponential fit, error bars indicate standard deviation in the mean. **d** Stacked histogram showing overall distribution of time to first flare, different colours represent different laser powers.

In Figure 6.6a the average number of flare events per second of measurement is calculated at each laser power. A clear exponential power dependence is observed, as demonstrated by the straight-line fit on a log-lin plot. This strongly suggests that there is an activation energy that required to induce a flare event, indicating a structural process at play. This can be compared to picocavities extracted from the same dataset, which have a known activation

energy of 0.8 eV [18]. Since the gradient is calculated to be $5\times$ that of the picocavity power dependence, this suggests an activation energy of 4 eV for the flare events. Interestingly, it is found that if the sample is left to ‘age’ in air for two weeks and the experiment is repeated, the number of flares observed drastically increases. This is seen by a shift in the power dependence. The gradient is unchanged and so therefore is the activation energy; however initial conditions must be affected. The overall morphology of NPoMs on the sample is not somehow altered by ageing processes, as the distribution of coupled-mode positions remains near-identical (Figure 6.6b).

The activation energy requirement is further demonstrated by analysing statistics of time dynamics of the system. The ‘waiting time’ before a flare event is detected can be extracted from the dataset as the time between the start of laser irradiation and the first flare event. There are a number of errors associated with this measurement, as it is not possible to wait an infinite amount of time, so the cut-off here is the 35 s of measurement. This can be shown to follow a negative exponential relationship with laser power (Figure 6.6c), again indicating some sort of potential energy barrier. The overall distribution can be seen in the stacked histogram of waiting times in Figure 6.6d. It can be seen that the distribution does not follow a normal distribution, but instead a wide spread of variation in waiting time can be seen for all powers, with a slightly higher tendency to earlier times.

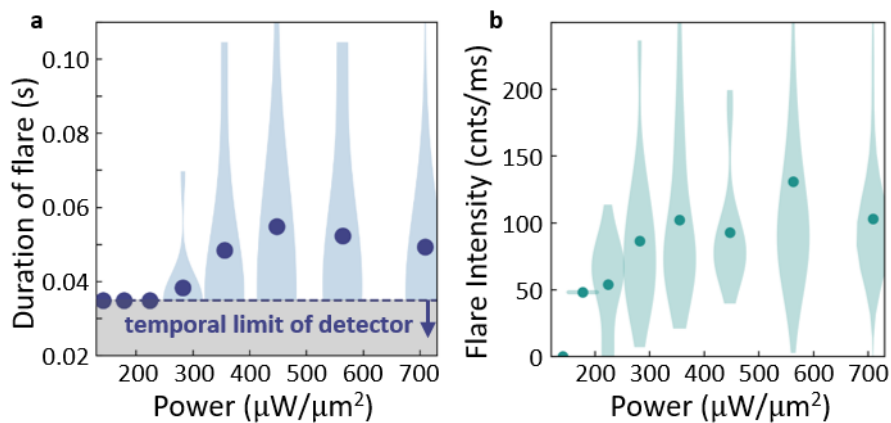


Fig. 6.7 Power Dependent Analysis of Flare Modes. **a** Violin plot showing duration of flare vs incident laser power. Points show mean values, blue shaded regions show distributions, grey region shows temporal limit of detector. **b** Violin plot showing height of extracted flare vs incident laser power. Points show mean values, shaded regions show distributions.

These flare events are themselves very short-lived. With a CW laser system temporal resolution is limited to the resolution of the detector, here 35 ms. However information on their duration can still be collected (Figure 6.7a). Points show the mean duration of a flare

event, with the blue violin plot showing the distribution in durations. The persistence of the flares can be seen to increase with laser power, suggesting that they are metastable if energy continues to be injected. The mean flare duration saturates at 50 ms, with larger variations both within and between NPoMs. As well as this, the integrated intensity of each flare mode can be fitted and extracted. This also appears to show a large variation (Figure 6.7b), and saturates at higher powers.

6.3 Comparison with Other Molecular Spacers

The clearest evidence that these flare events are in fact a physical effect and not down to purely equipmental fluctuations comes from the very different characteristics observed when biphenyl-4-thiol (BPT) is replaced with other molecular spacer molecules. Samples were made in which the BPT spacer was replaced by a more conductive equivalent (biphenyl-4,4'-dithiol: BPDT), a dye (methylene blue encapsulated in CB[7]: MB + CB[7]) as well as non-aromatic alkanethiol SAMs. In order to account for the slightly different gap distances produced with each of these spacers, three alkanethiols of varying heights were measured (hexadecanethiol: HDT; dodecanethiol: DDT; and nonanethiol: NNT).

More than 500 NPoM structures were analysed for each sample, and the mean number of flares is shown in Figure 6.8a. The addition of a second thiol group in BPDT can be seen to have little significant effect on the number of flares observed. Utilising instead an encased MB molecule shows a large increase, whereas the use of alkanethiols shows a very small, although non-zero, number of flares. No relationship between gap distance and number of flares is found between the alkanethiols. These results indicate that the termination bonding of molecular spacer to gold surface atoms is particularly important to consider in this system, as also shown when looking at picocavity adatoms, suggesting similar processes. It is important to note that the exclusion of water and ions as well as rigidity of SAM are not consistent across these samples, and this is likely having an additional effect on conditions in the gap.

Comparative density plots can be seen in Figures 6.8b-c. The distribution in coupled-mode wavelengths is shifted between the molecules, as expected and reported [36, 41], due to the differences in gap distance and gap refractive index of the subsequent NPoM structures. There are however clear differences in the density distributions of the flare modes when correlated to the λ_C wavelength. Both BPDT and BPT result in roughly bi-modal distributions, although the shape of these distributions is decidedly different. In comparison NPoM structures formed with MB + CB[7] show a much more unusual distribution shape, but no clearly clustered groups. It is interesting to note that although the spacer molecules have very different absorption spectra and refractive indices, the flare wavelength is centred

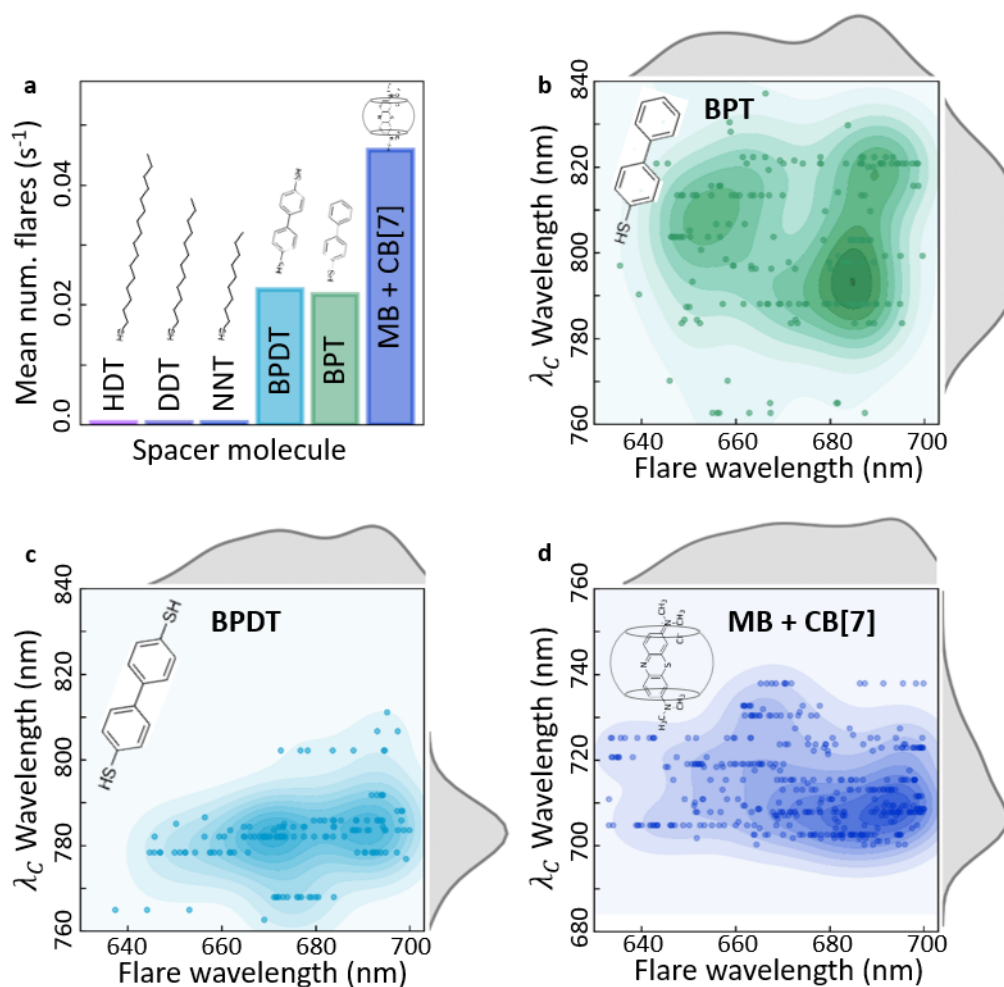


Fig. 6.8 **Comparison of Flare Modes for Different Spacer Molecules.** **a** Occurrence frequency of flare events for different spacer molecules depicted. Density maps showing spectral features of flare events observed for molecular spacers **b** biphenyl-4-thiol (BPT), **c** biphenyl-4,2-dithiol (BPDT) and **d** methylene blue dye (MB) encapsulated in cucurbit[7]uril molecules.

around roughly the same range, indicating processes related to this are not at the root of flare observations (more will be discussed in Chapter 7).

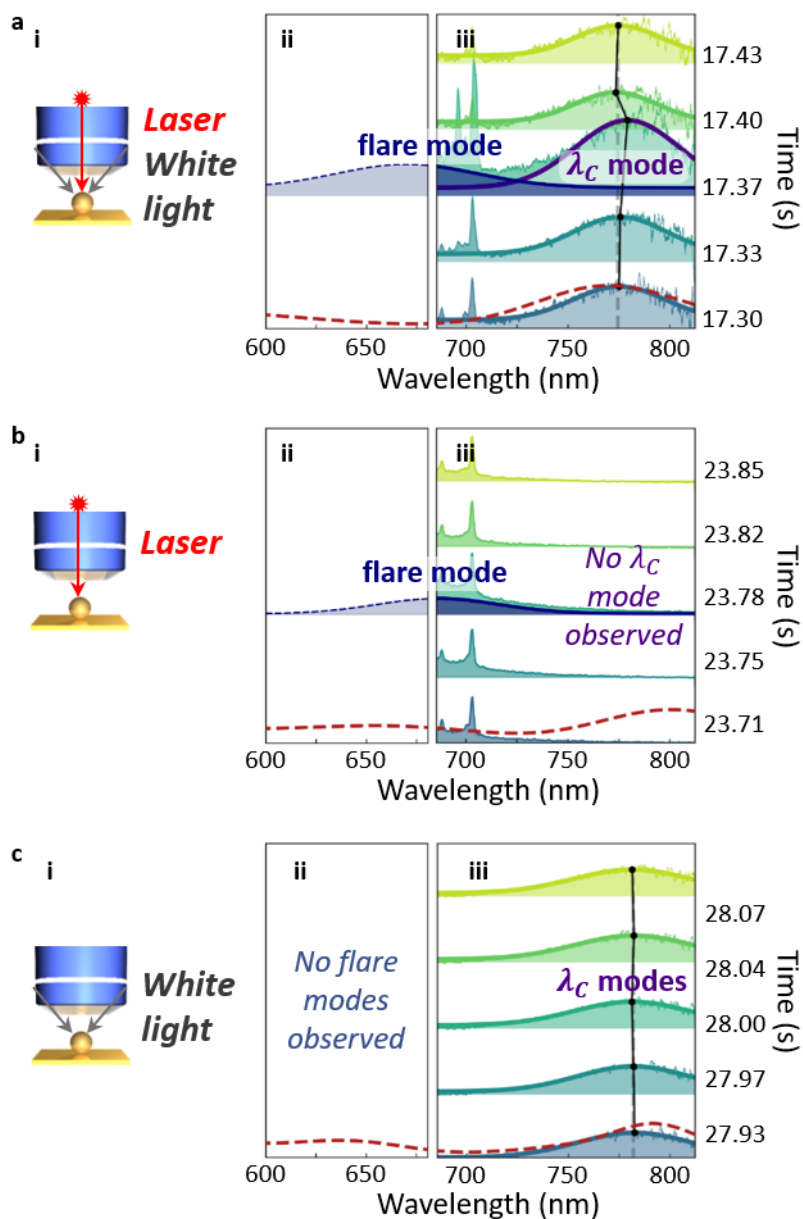


Fig. 6.9 **Simultaneous Observation of Flare and Coupled Modes.** Kinetic scattering spectra measured with **a** laser and white-light illumination, **b** laser illumination only, **c** white-light illumination only. Black points-on-line show coupled mode position. Left panels show flare fits. Dashed red line shows coupled mode measured with dark-field spectrometer, measured prior to kinetic series.

6.4 Combined White-Light and Inelastic Laser Light Scattering

Up until this point it is not obvious how flare events are linked to any kind of conformational change, since the shift in coupled mode is minimal and not correlated to the susceptibility of a NPoM construct to sustain a flare event. However in these measurements and analysis the dark-field scattering measurements used to characterise the NPoM are only taken before and after laser measurements. This is due to experimental constraints, whereby it is not possible to use a dark-field spectrometer when the laser is incident due to risk of it saturating. Additionally, the signal-to-noise ratio on the dark-field spectrometer limits integration times to 1 s, which is an order of magnitude larger than the flare event duration.

In order to investigate any changes to the NPoM scattering spectrum *during* a flare event, the experimental set-up was modified in a number of ways. The spectral grating was shifted in order to be able to observe the λ_C modes, which are higher in wavelength than the flare modes. Furthermore in addition to the laser excitation used to observe the flares, the system was simultaneously irradiated with the broad-band white light illumination usually used for standard dark-field scattering. Instead of measuring the dark-field scattering spectrum on the dark-field spectrometer, both laser scatter and white-light scatter were detected simultaneously on the Raman CCD (Figure 3.2). In this way any changes to λ_C could be observed exactly simultaneously to the flare event detection.

Figure 6.9a shows a typical flare event recorded in this way. Within the spectral range chosen, the higher-wavelength Raman modes of the BPT spacer molecule are visible as well as the tails of any flare events, giving an exact time stamp for when they occur. As mentioned, the coupled mode (λ_C) is also observed, and well matches the spectrum measured on the dark-field spectrometer at the start of the experiment (dashed red line). It can be seen that the λ_C mode stays relatively constant before and after the flare (dashed grey line shows average value), however at the exact time of the flare there is a small but clear instantaneous red-shift in mode position alongside an overall increase in intensity of the mode, before a return to initial position is observed. This observed red-shift in λ_C at the exact time-stamp of the flare event is strong evidence that the NPoM is undergoing structural changes in some way, but the return to initial position suggests this change is metastable, or that it is only fleetingly in the vicinity of the plasmonic hot-spot.

The control measurement in Figure 6.9b shows that with laser irradiation but no white light, no plasmonic coupled mode is observed, as expected. Additional control studies with white-light but no laser irradiation (Figure 6.9c) show consistent λ_C modes, unchanging over the course of the experiment. No flares are observed without laser irradiation.

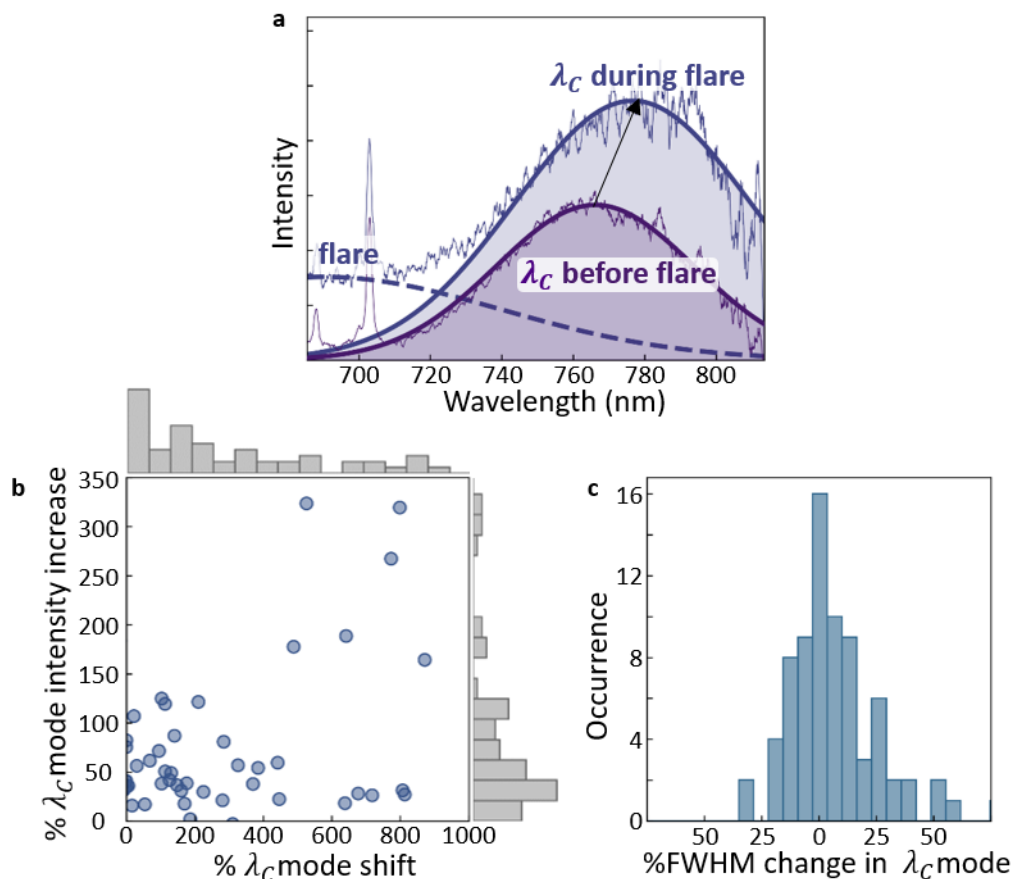


Fig. 6.10 Coupled Mode changes During Flare Events. **a** Example showing high-wavelength spectrum before flare event (purple) and during flare event (blue). Dashed line shows fitted flare mode. Solid lines show λ_C mode fits. **b** Correlation between coupled mode intensity increase and coupled mode redshift, both measured simultaneously to flare event. A Pearson coefficient of 0.35 indicates little to no correlation. Grey histograms top and right show individual distributions. **c** Percentage changes in full-width-half-maximum of coupled mode from before flare to during flare.

The λ_C red-shift is seen for over 250 NPoM structures measured. Whenever a flare is detected by the characteristic increase in background centred $\lesssim 700$ nm (dashed blue line Figure 6.10a), an increase in coupled mode is seen, accompanied by a λ_C red-shift. The degree of red-shift observed covers a wide range of values, as does the intensity increase, but both values are always positive, and a blue-shift or intensity decrease is never seen. The distribution in values can be seen in Figure 6.10b. Interestingly there is little correlation between the amount the mode increases and the degree it red-shifts, with a calculated Pearson coefficient of 0.35. This suggests that there are likely multiple processes at work. Not

pictured is the correlation between the flare-mode intensity and the λ_C shift, which is also insignificant, with a correlation coefficient of 0.22. Due to the constraints of the spectral window it is not possible to extract the wavelength of the flare mode without considerable error and so it is not possible to see whether this is related to the shifted λ_C position.

Figure 6.10c shows the distribution in percentage FWHM (full-width half-maximum) linewidth of the λ_C mode from before flare to during flare. There is a variation in width changes observed, with up to 50 % broadening or narrowing in width recorded, however as this distribution centres around zero it is not thought to be statistically significant.

6.5 Conclusion and Outlook

In this chapter I have presented the spectral features of unknown origin which I have termed ‘flare’ modes, for which I will discuss possible explanations of origin for in the following chapter. I have undertaken in-depth statistical analysis on the shape and characteristics of these modes, as well as analysed how the occurrence and spectral shape are altered by incident power and choice of molecular spacer.

In addition to this I have presented a new experimental technique which enables simultaneous observation of the elastically scattered coupled-plasmon mode excited via broad-band white light and inelastic flare modes with laser excitation. With this technique it is possible to observe the emergence of flare modes at the same time as recording the subsequent changes to the NPoM coupled mode. Although these flare events clearly require laser-light activation in order to occur (Section 6.2.1, Figure 6.9), detailed studies on the effect of incident laser *wavelength* have not been undertaken. This would be a very interesting additional measurement with the question of whether or not the flare wavelength was subsequently altered or not, providing additional clues to the flare mode’s origin. It would also be very interesting to look beyond molecular spacers to ‘hard’ spacers such as 2D materials (Section 2.14) as the NPoM surface energy, shown to be an important factor, would be very different.

The observations and analysis provided in this chapter have provided clues and evidence towards the origin of these so-called flare modes. In this next chapter I will look at how these puzzle pieces fit together and suggest possible roots of this broad-band light emission.

Chapter 7

Possible Origins of Flare modes

In the previous chapter I introduced a newly observed spectral feature which I have termed ‘flare’ modes. These inelastic modes are broad-band and very fleeting in time, as well as being relatively rare to see (only observed on 8% of NPoM structures measured). In this chapter I present a number of theories as to the origin of these modes. This list is by no means exhaustive and at this point it is not possible to fully conclude with certainty that any one of these theories is the definite origin of the flare-mode emission. Instead, I aim to present a number of possible explanations and to discuss the merits and pitfalls of each in turn, using the experimental evidence gathered in Chapter 6.

A large amount of data and analysis is presented in Chapter 6, providing a plethora of evidence and constraints on the potential origins of flares. Here I summarise the main experimentally observed features which require consideration when discussing possible theories:

- **The spectral range of flare wavelengths seen** (Figures 6.3, 6.4, 6.8). Under laser irradiation flares are only observed under in the 640-700 nm region, and are not seen for wavelengths > 700 nm (Figure 6.9). Although the distribution within this region changes with use of different molecules, the spectral range does not vary considerably.
- **No change to SERS lines of molecules observed** (Figure 6.1,6.3). The spacer nanocavity lines do not change in intensity and unlike a picocavity there is no observation of new spectral lines appearing at the time of a flare event.
- **The ms temporal dynamics of flare modes observed.** Flares appear sporadically, with the majority of NPoM structures demonstrating no flares at all in the time window of the measurement (Figures 6.4, 6.6). When they do appear, they are very fleeting, with mode durations of 30 – 100 ms (Figure 6.7).

- **The increased likelihood of flare events with sample age** (Figure 6.6).
- **The variation in number of flares observed with different spacer molecules** (Figure 6.8)
- **The observed changes to coupled mode (λ_C) at the time of a flare event.** When a flare mode is observed, a corresponding change in the dark-field scattering from the coupled mode can be simultaneously observed if the system is illuminated with a white-light as well as the 633 nm laser. The coupled mode is observed to red-shift and increase in intensity, although the magnitude of red-shift is not proportional to the intensity increase, suggesting multiple effects at play.

In light of these observations I will discuss a number of possible flare-mode origin theories:

1. Black-body radiation
2. Two photon absorption and emission
3. Hot electron emission
4. Structural changes to the nanoparticle. These include:
 - (a) A ‘pico-hole’
 - (b) A nanoparticle ‘crack’
 - (c) A grain boundary or defect.

Within these structural changes I will discuss how the changes in plasmonic modes can be emitted to the far-field, via discussion of electronic Raman scattering (ERS) and stimulated electronic Raman scattering (stimulated ERS).

7.1 Black-body Radiation

Due to the broad spectral shape of the flare modes, a natural initial assumption might be to suggest they are the result of black-body radiation. Black-body radiation is the emission of broad-band EM radiation from a black-body, with an emitted spectrum dependent entirely on the temperature of the body. There are a number of assumptions made when considering a perfect black-body. Black-body radiation assumes the system is in thermodynamic equilibrium. It also assumes the body is a perfect absorber (no reflection) and that all radiation leaving the object is independent of its structure and material, which we know not to be the

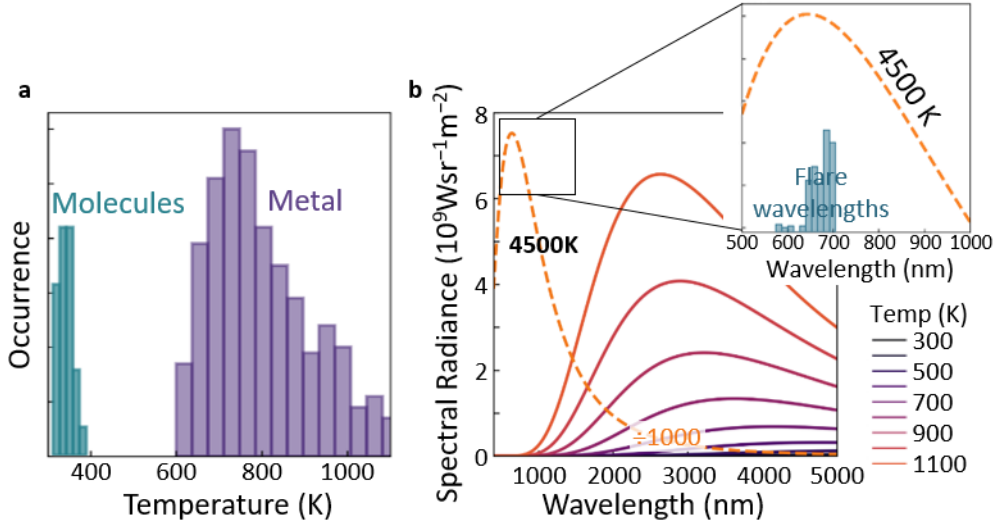


Fig. 7.1 **Black-Body Radiation.** **a** Measured molecular and metal temperatures from the experimental data in Chapter 6, calculated via anti-Stokes:Stokes peak ratios and anti-Stokes background exponentials, respectively. **b** Black-body radiation spectrum calculated using Equation 7.1 for the range of temperatures in (a). Inset shows a histogram of the centre wavelength of the observed flare modes. Dashed line shows temperature required to reach black-body radiation in this spectral region.

case for molecules and plasmonic metals. Additionally, light emission is diffuse, therefore radiating equally in all directions. Despite a lot of these assumptions not holding true for the system we are considering here, it has been shown that for many objects which are not black-bodies, such as planets and stars, black-body radiation can still be used as a first approximation [125].

Black-body emission is given by the spectral radiance (defined as the radiance of a surface per unit wavelength), $B_\lambda(\lambda, T)$ and is calculated in terms of wavelength (λ) and temperature (T) by the Planck equation:

$$B_\lambda(\lambda, T) = \frac{2hc^2}{\lambda^5} \frac{1}{e^{\frac{hc}{\lambda k_B T}} - 1}. \quad (7.1)$$

In the system that we are looking at there are two main components: the metal and the molecules, which are known to display slightly different temperatures under laser irradiation [113, 60]. The molecular temperature can be calculated experimentally through calculating the ratio of anti-Stokes:Stokes peak intensities, as was shown in Section 5.1.2, Equation 5.1. The electronic temperature of the metal can be calculated through measurement of the anti-Stokes background exponential, as described in [60]. Both distributions can be seen in

Figure 7.1a. Molecular temperatures fill a narrow distribution, just above room temperature, due to slight heating by the laser. The electrons in the metal are more directly pumped by the laser via the plasmon and so have higher temperatures in the region of 600-1100 K. The broader distribution in metal temperatures is likely due to the variation in incoupling efficiency to the NPoM structure by nanoparticles of different geometries.

In Figure 7.1b the Planck equation is plotted for the 300-1100 K range of temperatures measured in experiment. With these temperatures, black-body radiation would be expected to emit at $\lambda = 3000$ nm and higher, a much longer wavelength than the flare modes observed in experiment. The range of experimental wavelengths observed is shown in the histogram in the inset of Figure 7.1b, and spans the 600-700 nm spectral range. Working backwards from this we can calculate the black-body temperatures that would be required in order to see radiation in this spectral region to be ≈ 4500 K (dashed line, inset). There is no evidence so far that components of the system can reach temperatures anywhere close to this value, although it is true that the metallic temperatures measured this way give only the average value and do not elucidate the energy distribution within the metal. Black-body emission would additionally be expected to be consistent in time, and not show the temporal fluctuations observed within the system. For these reasons I believe we can discount black-body radiation as an origin of flare-mode emission.

7.2 Two-Photon Absorption and Emission

The process of two-photon absorption was predicted in 1931 [126] and confirmed experimentally 30 years later [127, 128]. In this process photons excite a molecule from the electronic ground state to an excited state, via a virtual state (red arrows, Figure 7.2a). This is followed by non-radiative relaxation (green) and then spontaneous radiative emission of two (or one) photons from the lowest excited state. The energy gap between the ground and excited states is set by the absorption properties of the molecule. In our measurements I initially utilise biphenyl-4-thiol (BPT) as a molecule in the gap, which has an absorption at 350 nm. In experiments the incident laser light is of wavelength 633 nm, therefore 2-photon absorption will excite the molecule beyond the lowest excited state. Following non-radiative relaxation, the spontaneous emission is from the lowest excited state, meaning the emitted light has to be of a wavelength > 633 nm and will in fact be centred around 700 nm. Single-photon emission is more likely, however this would result in an emitted photon of wavelength 350 nm, which is outside of the spectral region measured in experiment.

Since there are two laser photons absorbed here it should result in an emitted light intensity that goes as the square of the incident laser power. The violin plot of integrated

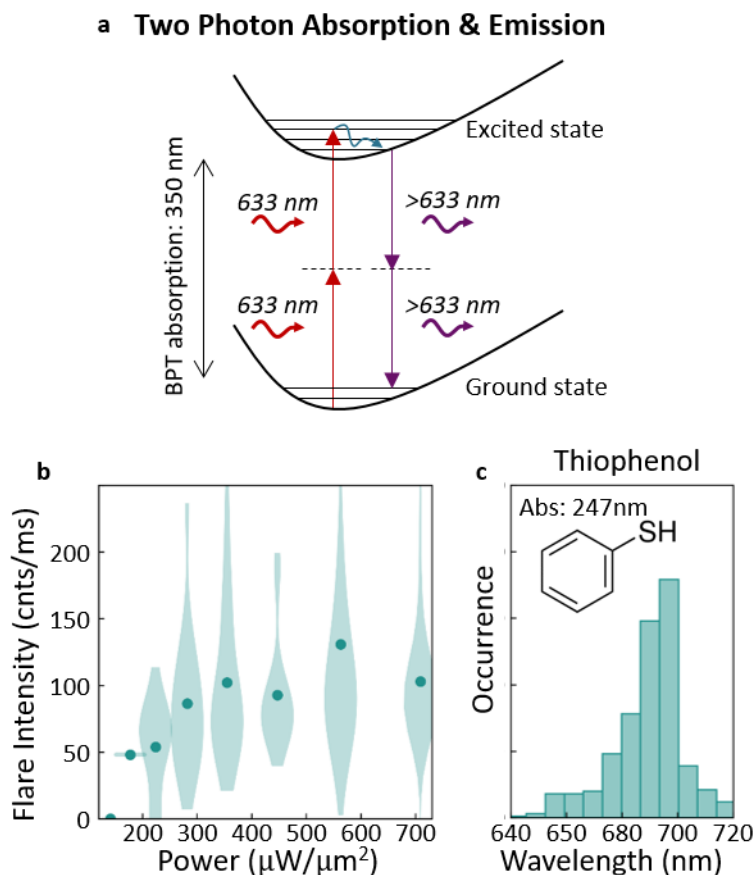


Fig. 7.2 Two-Photon Absorption and Emission. **a** Energy level diagram showing two-photon absorption followed by two photon-emission for the BPT molecule. Single photon emission is also possible but would result in emission in at 350 nm, outside of the measured spectral window, hence it is not considered here. **b** Experimental observations of integrated flare intensity with power, repeated from Figure 6.7, showing a sub-linear power dependence. Points show mean values, shaded regions show distributions. **c** Distribution of measured flare wavelengths for thiophenol. With an absorption at 247 nm, two photon emission would be measured at 494 nm, with three photon emission at 741 nm, neither matching with this distribution.

flare intensity with power from Section 6.2.1 is shown again here. This super-linear power dependence is clearly not observed. Instead a sub-linear dependence is seen, with saturation towards integrated intensities of 200 counts/ms.

An additional pitfall for this theory is the aforementioned similarity in flare wavelengths seen when different spacer molecules are utilised. Although there are some slight differences, molecular absorptions vary from 350 nm (BPT) to 680 nm (methylene blue). As a further check, a less-conjugated thiophenol molecule is measured (Figure 7.2c). Thiophenol has an

absorption at 247 nm, but the flare emission is still seen to be centred ≈ 700 nm, which does not fit with this model.

As well as these issues with expected wavelength of light emission, the model of two-photon absorption would also predict a consistent emission in time, with changes to intensity arising only from incident laser power. As mentioned this is not observed in experiment. For both of these reasons I believe we can discount two-photon emission as an explanation for flare mode emission.

7.3 Hot Electrons

Hot electrons are those within the energy distribution which have kinetic energy much higher than the Fermi level. They are known to occur in plasmonic metals as a result of non-radiative decay of the plasmon [129, 130]. Hot-electron light emission can subsequently occur as a result of electron-phonon scattering. However this occurs on a picosecond time-scale, and would be expected to appear constant on the millisecond time-scale used in experiments in Chapter 6. Hot electrons in 15 nm diameter nanoparticles have been predicted to have energies up to 2 eV [129]. This corresponds to 620 nm, so well-matched to the experimental region observed. However when slightly larger nanoparticles are used (diameter 25 nm), this falls to fractions of an electronvolt, corresponding to wavelengths > 1000 nm. For the 80 nm nanoparticles used in experiments here, the emission would be expected to be at even longer wavelengths. This is directly at odds with experimental observations, meaning we can discount this as a potential explanation.

7.4 Structural Changes

All the theories for flare-event origin suggested above have a common issue when comparing to experimental observations, in that none can explain the temporal nature of the flares. Flares appear inconsistently and infrequently, and when they do appear they have lifetimes on the order of 30 ms, whereas the lifetimes of processes described above are considerably shorter and so would be expected to appear consistent in time on our measurement time-scales. They also cannot explain the coupled-mode shifts seen in the dark-field at the exact time of a flare event, which strongly suggests a change in the NPoM structure.

In light of these inconsistencies I now turn to consider possible structural changes to the nanoparticle-on-mirror construct. It has been shown that structural changes to the surface of the nanoparticle can be observed under laser irradiation, including facet growth [48], formation of connective bridges [131] and picocavity-forming adatoms [18].

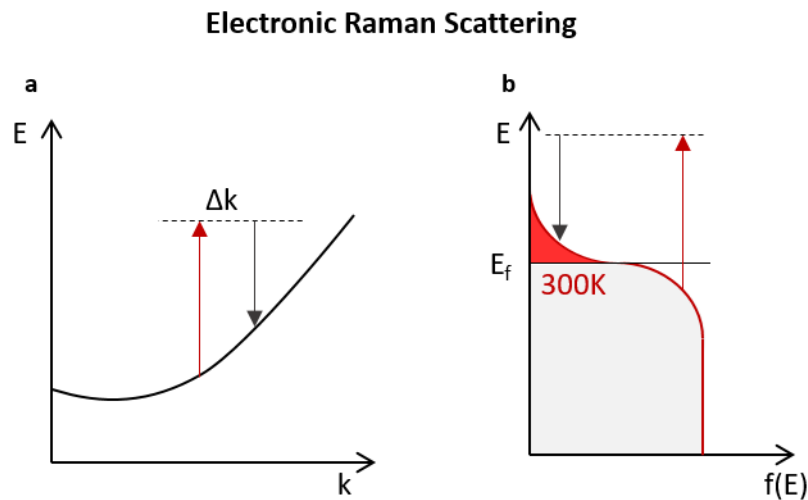


Fig. 7.3 **Electronic Raman Scattering.** **a** Band diagram and **b** Fermi diagram illustrating the electronic Raman scattering process responsible for SERS background. Electrons in the metal are photo-excited to a virtual state (dashed line) before radiatively relaxing to thermally excited states above the Fermi level (shaded red).

Here I propose 3 further structural alterations, and consider the implications of each:

- A ‘pico-hole’
- A nanoparticle ‘crack’
- A grain boundary or defect

For each of these geometries full boundary-element-method (BEM) simulations are carried out¹. In order for these structural changes to lead to light emission at the flare mode, it is suggested that the plasmonic resonances of the NPoM are altered by the change in geometry, and that light is emitted at the wavelengths of these altered modes via electronic Raman scattering, giving rise to the observed flare modes. Electronic Raman scattering (ERS) has been suggested in previous work to be at the root of observed SERS background effects and has been shown to follow the shape of the plasmon resonance [60, 61]. In this process electrons in the metal are photo-excited to a high-energy virtual state, before relaxing via Raman emission to states above the Fermi energy (Figure 7.3). This process requires a momentum change, Δk , which is provided by the field gradient inside the metal and is strongest at plasmon resonances, therefore giving an ERS background which mimics the

¹All BEM simulations in this thesis are developed and carried out by Mattin Urbieto, Materials Physics Center and Donostia International Physics Center, San Sebastian, with results analysed in collaboration with myself.

spectral shape of the plasmon resonance. ERS also requires light to penetrate into the metal. However, a mechanism is also required by which this ERS background is augmented above normal levels, as in the absence of flares it is too weak to be seen at these integration times.

It is noted that other studies have attributed the SERS background to interband scattering [132], however this is shown to also follow the plasmon resonance and so perhaps does not greatly affect this theory.

7.4.1 The Pico-hole Geometry

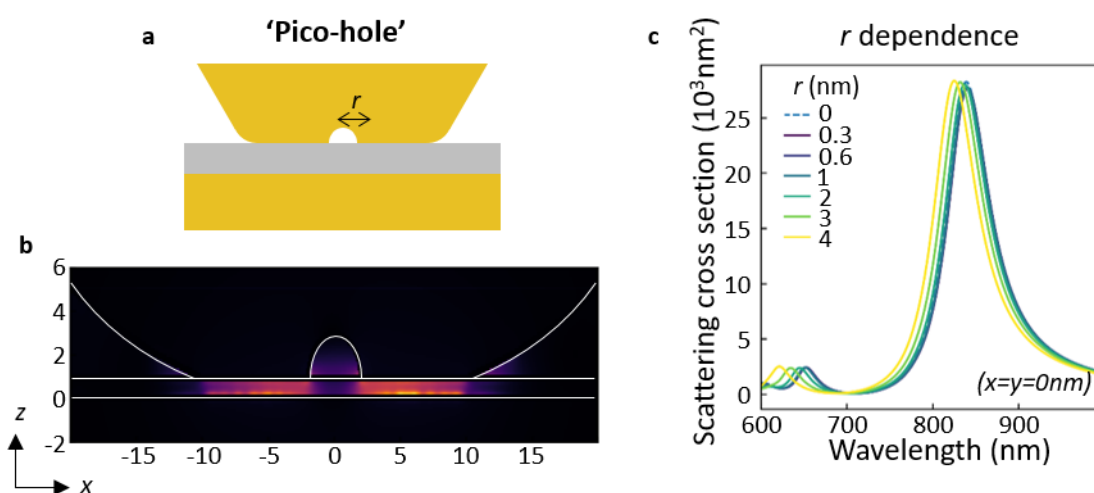


Fig. 7.4 **'Pico-hole' in a Nanoparticle Facet.** **a** The 'pico-hole' geometry simulated. **b** Simulated near-field intensities in the gap region. **c** Simulated Rayleigh-scattering cross-sections for various radii of pico-hole.

Since it has recently been shown that adatoms can form on the surface of nanoparticles, it is not unreasonable to consider the converse situation of a hole formed on the bottom facet of a nanoparticle. Figure 7.4a shows the geometry modelled in simulations. The calculated near-field can be seen in Figure 7.4b alongside the scattering cross-section in (c). The scattering cross-section shows the predicted plasmonic modes and is calculated for a variety of picohole sizes, from one atom up to much larger holes (0.3-4 nm in radius).

There are a number of issues with this geometry. Predominantly: what does it mean to have a 'hole' in the gold? It is very energetically unfavourable to form a vacuum in a system, so it is much more likely to be filled with air. In terms of surface energies, the energy required for an Au-air boundary is considerably higher than the Au-Au cohesion energy, making this exact geometry unlikely [133]. If, somehow, a pico-hole were to form on the surface of a nanoparticle, another issue is presented by the near-field map in Figure 7.4b. Picocavities

are recognised spectrally by the additional lines in the SERS spectrum observed due to the local field gradients created by the sharp feature of an adatom (see Section 2.3.3, and further analysis in Chapter 5). It can be seen that although it provides less of a lightning rod than the picocavity case, the pico-hole also produces a field gradient, and would be expected to similarly break the IR selection rules. However no extra lines are observed experimentally in the SERS spectra at the same time as flare events, suggesting that if nanoparticle structural changes are at the root of these modes, they must be changes which do not lead to extra field enhancement in the vicinity of the molecules.

7.4.2 The Nanoparticle Crack Geometry

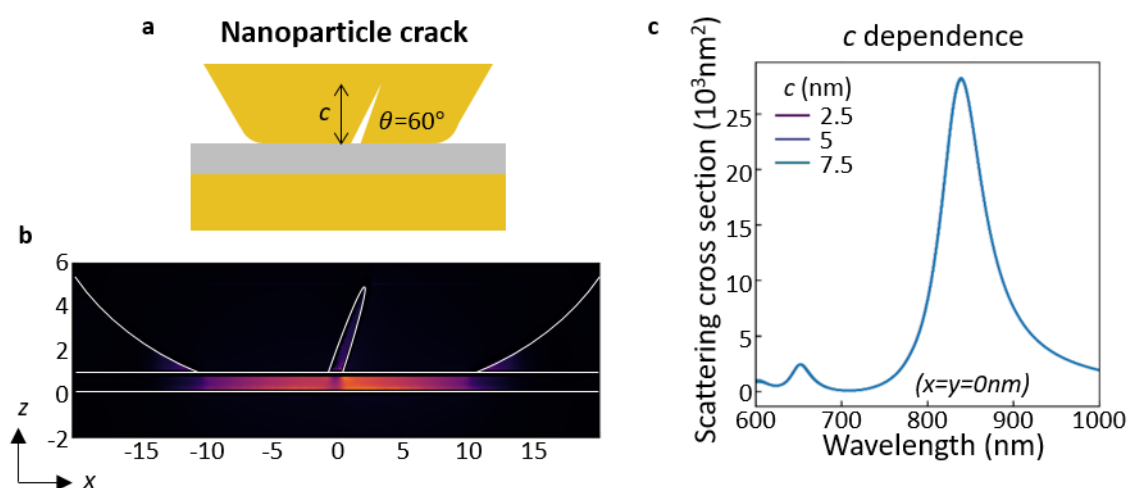


Fig. 7.5 **Nanoparticle Crack.** **a** The nanoparticle crack geometry simulated. **b** Simulated near-field intensities in the gap region. **c** Simulated Rayleigh-scattering cross-sections for various heights of crack.

As previously mentioned, the nanoparticles used in experiments are not truly spherical and instead have a variety of shapes. One of the geometries observed via SEM is the pentagonal bipyramid, or the similar truncated Marks decahedron structure [123, 134]. Pentagonal bipyramids are known to have an angle mismatch in their structure and have been shown to therefore exhibit variable strain throughout the nanoparticle [135]. The suggestion with this geometry is that perhaps this strain could in some way lead to a ‘crack’ through the centre of the nanoparticle as illustrated in Figure 7.5a. The simulated near-field and scattering cross-sections for this geometry can be seen in Figure 7.5b,c. It can be seen that the height of the crack has little effect on the scattering cross-section calculated. This is perhaps not

completely unexpected since the metal surface in the vicinity of the hot-spot is known to dominate the optical fields.

However, this geometry suffers from many of the same pitfalls as the pico-hole in Section 7.4.1. The near-field map can again be seen to demonstrate higher field gradients which would be expected to be visible in the SERS spectra as extra picocavity-like lines. Additionally it has to be considered how realistic this geometry is from a materials point of view. The formation of a crack in the nanoparticle involves the formation of two new Au-air boundaries, which requires considerably more energy than the Au-Au cohesion energy, as previously mentioned [133].

7.4.3 A Grain Boundary Modelled by a Reduction in Local Plasma Frequency

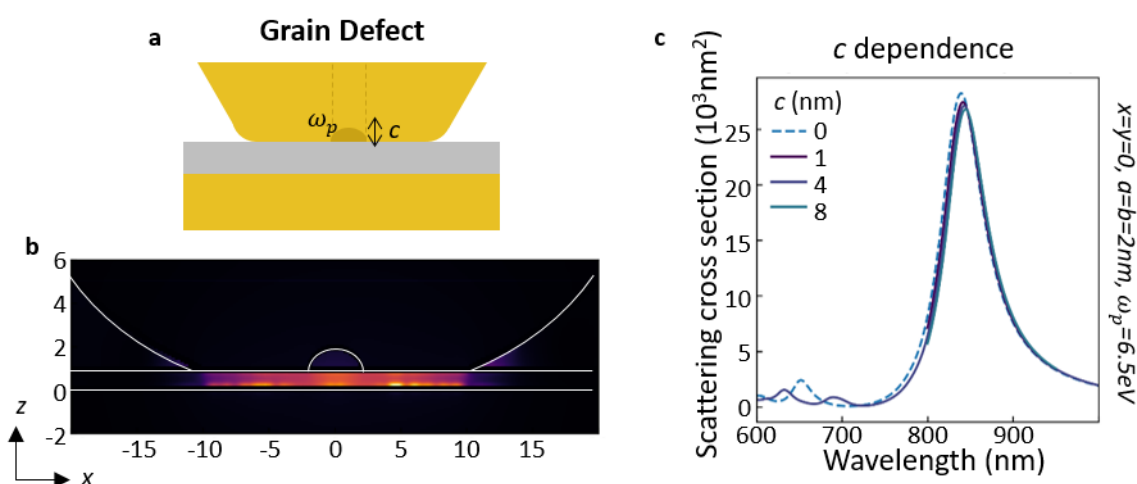


Fig. 7.6 **Grain Defect on the Nanoparticle Facet.** **a** The grain-defect geometry simulated by a patch of reduced ω_p . **b** Simulated near-field intensities in the gap region. **c** Simulated Rayleigh-scattering cross-sections for various patch sizes.

Rather than forming a crack due to the lattice-plane defects, it is more realistic to think instead of a grain boundary with a reduced number density of gold atoms. Such grain boundaries have been shown to appear at the facets of nanoparticles using electron-microscopy methods [75, 76] but changes observed using optical methods have not yet been shown. Since the local plasma frequency is related to the number density via $\omega_p^2 = \frac{ne^2}{\epsilon_0 m^*}$ (see Section 2.1.1), in a classical picture the reduction in number density has the effect of directly reducing the local plasma frequency in the vicinity of the defect. It has been suggested that local plasma frequencies are reduced by 25 % in the vicinity of a grain boundary [121].

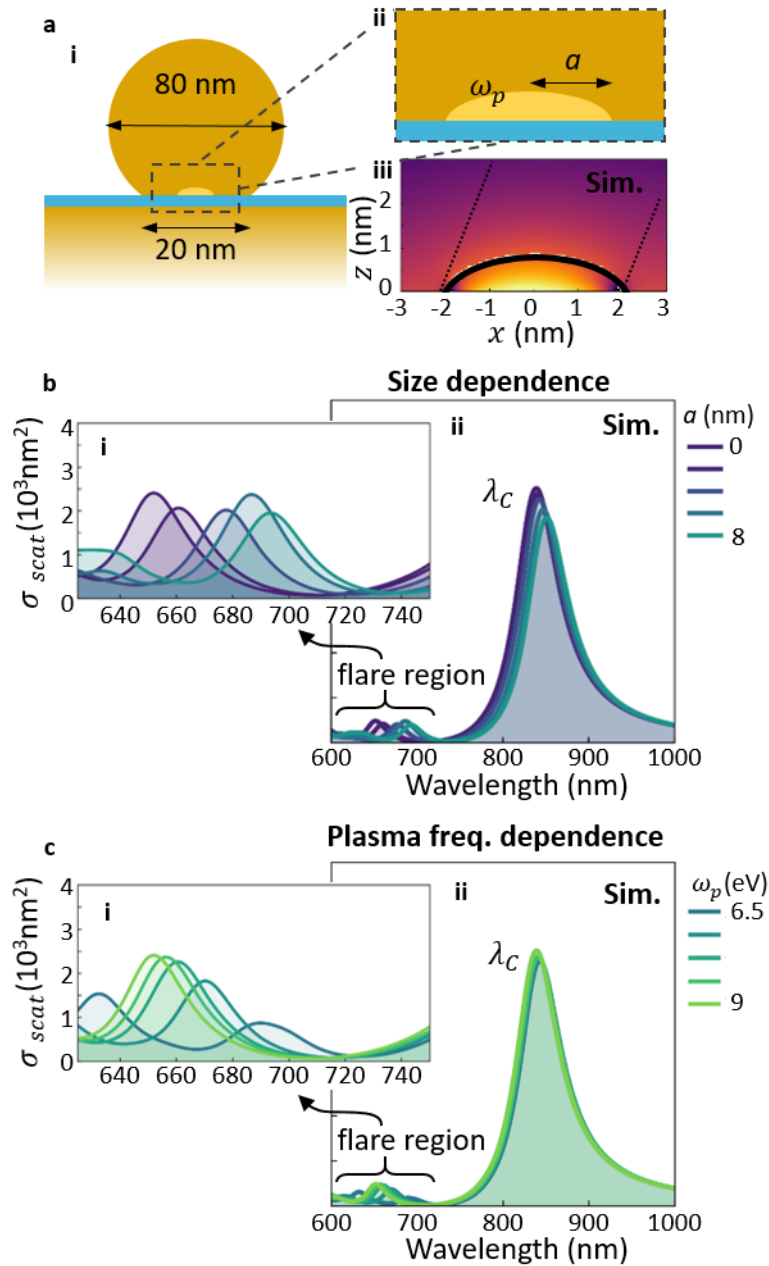


Fig. 7.7 Further Simulations on the Grain Defect Patch Geometry. **a,i**, BEM simulation geometry. **ii** shows region of defect patch of lower ω_p and radius a , with **iii**, optical field inside patch at coupled mode resonance λ_C (black line shows boundary between bulk gold and defect patch). **b** Simulated scattering cross sections (σ_{scat}) for patch of $\omega_p = 7 \text{ eV}$ for $a = 0 - 8 \text{ nm}$. Inset shows zoom in of observed flare region. **c** Simulated scattering cross sections (σ_{scat}) for patch of $a = 2 \text{ nm}$ for $\omega_p = 6.5 - 9 \text{ eV}$, where $\omega_p(\text{bulkAu}) = 9 \text{ eV}$ is the plasma frequency of the bulk gold. Inset shows zoom in of observed flare region.

Grain boundaries and lattice defects cause a similar reduction of this local plasma frequency, meaning this classical model is relatively flexible, with the size of patch and amount of reduction in ω_p accounting for the existence of many different types of defect. As well as being a more realistic representation of the physical effects of atomic lattice boundaries than the crack in Section 7.4.2, this geometry does not suffer from the issue of increased field gradients, a feature which would lead to additional Raman lines (Figure 7.6b). It can be seen in Figure 7.6c, that similarly to the crack geometry, the height of the patch does not significantly effect results, reinforcing the idea that the surface effects dominate the far-field response.

Further analysis can be done on this simulated structure, shown in Figure 7.7. A small patch of reduced ω_p is placed in the centre of the bottom facet of the nanoparticle, as shown by the schematic in Figure 7.7a,i-ii. The small penetration of light into the metal is shown by the field intensity in Figure 7.7a,iii, demonstrating why the height of the patch has little effect. The effect on far-field optical scatter with changes in size and plasma frequency are shown in Figure 7.7a,b respectively.

With the introduction of this patch of reduced plasma frequency, $\omega_p - \Delta\omega_p$, it can be seen that higher order (shorter wavelength) plasmon modes can be shifted from the simple NPoM case. Both an increase in size of the patch and an increase in $\Delta\omega_p$ can shift the plasmonic modes across the 640-700 nm spectral region, covering the region in which flare modes are observed in experiment and giving credibility to this model as an explanation for experimental observations.

As previously mentioned at the start of this section it is important when discussing this theory of ERS emission to consider why the signal would be expected to be much higher than the weak ERS background usually observed from NPoM structures. By considering that enhanced Raman scales to the 4th power of the optical field, it can be shown (Appendix C) that the increase in ERS background is given by:

$$\frac{I_{flare}}{I_{noflare}} = \left(\frac{a}{w}\right)^2 \left[\frac{e(\omega_p - \Delta\omega_p)}{e(\omega_p)}\right]^5, \quad (7.2)$$

where a, w are the width of the patch and the nanoparticle facet, respectively; $e(\omega_p - \Delta\omega_p)$ is the field penetration in the patch of reduced ω_p representing the grain boundary and $e(\omega_p)$ is the field penetration into the rest of the metal. The perpendicular displacement field, D_{\perp} , across the metal-gap boundary is conserved, therefore

$$\epsilon_m E_{\perp m} = \epsilon_g E_{\perp g}, \quad (7.3)$$

where $\epsilon_{g,m}$ are the permittivities in the gap and metal respectively. Field penetration into the metal is therefore given by $e = \frac{\epsilon_g}{\epsilon_m}$. When ω_p is reduced at a grain boundary, so is ϵ_m , thus increasing field penetration in this region to $e(\omega_p - \Delta\omega_p)$. Therefore it can be seen that a patch of reduced plasma frequency will increase the penetration of light into the metal and thus increase emitted light from the ERS background process.

As well as the emergence of new modes in the flare region, a red-shift in coupled mode (λ_C) is seen with increasing size of the patch, matching what is seen in experiments. However in simulations this red-shift is always accompanied by a *decrease* in intensity of λ_C , which is directly the opposite of experimental observations. This will be discussed in more detail in Section 7.5.

Analytical Description

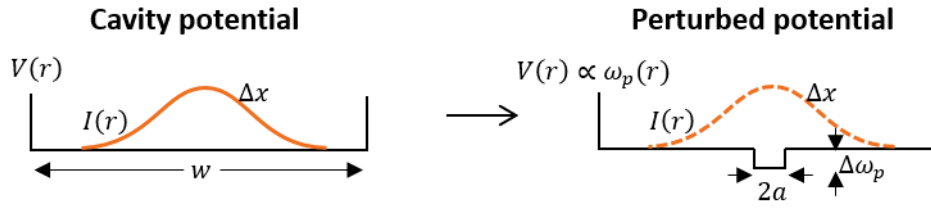


Fig. 7.8 Analytic Model for Patch Perturbing ω_p at Centre of Nanoparticle Facet.

As shown in Figure 7.7, both a larger $\Delta\omega_p$ in the defect ‘patch’ region at the centre of the nanoparticle facet and an increase in patch radius can affect the plasmonic modes of the simulated system. In order to better understand this it is useful to consider an analytical perturbation model of the system. Here we concentrate on the λ_C red-shifts predicted by the introduction of the patch of reduced ω_p . The metal-insulator-metal dispersion relation has shown to be a good approximation for modes within the nanoparticle-on-mirror cavity, and is given by [136]:

$$k_{||} = -\frac{2\epsilon_{gap}}{d\epsilon_{metal}} = -\frac{2\epsilon_{gap}}{d} \left[\epsilon_{\infty} - \frac{\omega_p^2}{\omega_{loc}^2} \right]^{-1}, \quad (7.4)$$

where $k_{||}$ is the wavevector parallel to the surface, d is the gap distance, ϵ_{gap} , ϵ_{metal} are the dielectric constants in the gap and metal respectively, ω_{loc} is the local frequency and ω_p is the plasma frequency of the gold. Rearranging this for ω_{loc} gives the local dispersion relation:

$$\omega_{loc}^2 = \frac{\omega_p^2}{\epsilon_{\infty} - \frac{2\epsilon_{gap}}{k_{||}d}}. \quad (7.5)$$

To calculate the change in λ_C when a patch of reduced ω_p is included, it can be assumed that the Gaussian field intensity of the mode in the gap is perturbed by a small change in potential proportional to ω_p . The original gap cavity potential with no patch region is shown on the left-hand side of Figure 7.8, with the perturbed potential shown on the right. By assuming that the local shift in frequency is proportional to the change in plasma frequency ($\delta\lambda_C/\lambda_C = -\delta\omega_{loc}/\omega_{loc}$), and assuming an unperturbed plasmon frequency ω_{p0} , the overlap integral in this first order perturbation theory can be written:

$$\begin{aligned}\frac{\delta\lambda_C}{\lambda_C} &= -\frac{1}{2} \frac{\int I(r) \frac{\delta\omega_p}{\omega_p} d^2r}{\int I(r) d^2r} \\ &= \frac{1}{2} \frac{\int I(r) \left[1 - \frac{\omega_p(r)}{\omega_{p0}}\right] d^2r}{\int I(r) d^2r} \\ &= \frac{1}{2} \left(\frac{\Delta\omega_p}{\omega_{p0}}\right) \int_0^a \exp\left(-\ln 2 \frac{r^2}{\Delta x^2}\right) \cdot d^2r,\end{aligned}\quad (7.6)$$

where $\Delta x = \sqrt{2Rd/\epsilon_{gap}}$ is the lateral spatial width of the coupled mode, R is the nanoparticle radius and d the gap distance. The prefactor of 1/2 is included since the perturbation is assumed only on one side of the waveguide (the nanoparticle facet side). The final result can then be written:

$$\frac{\delta\lambda_C}{\lambda_C} = \frac{1}{2} \left(\frac{\Delta\omega_p}{\omega_{p0}}\right) \left[1 - \exp\left(-\frac{\epsilon_g a^2 \ln 2}{2Rd}\right)\right] \quad (7.7)$$

giving an analytical expression for coupled mode shifts on the introduction of a patch of reduced ω_p .

Equation 7.7 can be plotted for a and $\Delta\omega_p$, as shown by the dashed lines in Figure 7.9a,i-ii. This is compared to the results calculated in BEM simulations (points, Figure 7.9a,b) and can be seen to match well for low values of $a, \Delta\omega_p$.

The coupled-mode red-shift (Equation 7.7) and increase in ERS intensity (Equation 7.2) can be plotted across both a and ω_p parameter space in order to compare to experimental observations (Figure 7.9b). Dashed purple lines show the variation in patch radius, a , for a constant value of $\Delta\omega_p$ and solid lines show varied $\Delta\omega_p$ for a constant patch radius. The grey histograms left and bottom show the experimentally measured distributions of flare intensity compared to background ($I_{flare}/I_{noflare}$, left) and of percentage red-shift in λ_C (bottom). This shows that there is a range of patch characteristics which could lead to the variety of experimental results observed, illustrating the possible variations in grain boundaries and defects indicated by this model. A central density of small patches ($a = 2 - 4$ nm) with high deviation from bulk gold plasma frequency ($\Delta\omega_p = 2.5 - 2.8$ eV) is predicted (highlighted

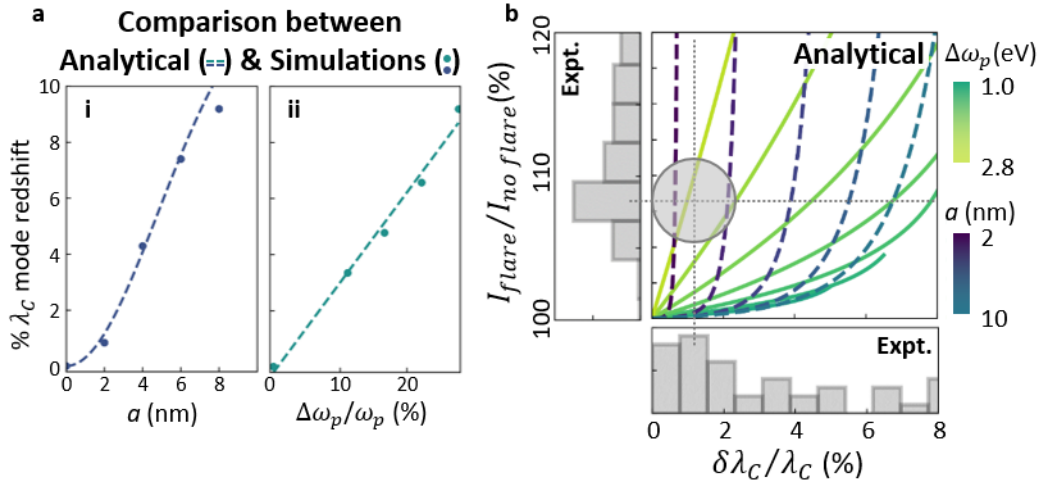


Fig. 7.9 Comparison of Analytical Model to Simulations and Experiments. **a** Comparison between analytical model (dashed line) and BEM simulations (points) when calculating the percentage λ_C red-shift for different values of **i** a ($\Delta\omega_p = 1.5$ eV), and **ii** $\Delta\omega_p/\omega_p$ ($a = 8$ nm). **b** Analytical model for relative flare intensity and mode red-shift vs $(a, \Delta\omega_p)$. Grey histograms show experimental distributions for flare intensity (left) and λ_C mode red-shift (bottom). Grey dashed lines and shaded circle show maximum likelihood regions from experimental results.

by dashed lines and shaded circle). These parameters strongly suggest single- or few-plane defects, such as those which have been observed via other methods [75, 76, 121].

Evaluation of Grain Boundary Model as Origin of Flare Modes

In this section I have shown that the model of a patch (radius a) of reduced plasma frequency $\omega_p - \Delta\omega_p$, analogous to a grain boundary reaching the surface of a gold nanoparticle, has the potential to explain a lot of the observed features of flare modes. The spectral range of flares observed in Chapter 6 is well matched to the short-wavelength plasmonic modes, altered by defect patches of various sizes and reduced plasma frequencies. Compared to the other two geometries considered in Sections 7.4.1 and 7.4.2, this is the only one in which a change to the plasmonic modes is achieved without creating a lightning-rod region which would be expected to throw up extra spectral lines in the Raman spectra.

In order to match the temporal observations of flare modes which appear sporadically, the grain boundaries must appear and disappear on the millisecond time-scale, before reverting to an identical situation as before. While this is unlikely due to the complete reorganisation

of the nanoparticle crystal structure required, a plausible explanation would be that the defects move across and away from the plasmonic hot-spot on this time-scale, only becoming observable when directly in the vicinity of the facet centre. Although nanoparticles have been shown to have a quasi-molten nature [124, 123, 122] via electron microscopy methods, this is the first time that these sort of effects have been observed optically. If we are indeed viewing the formation and restructuring of atomic-scale surface defects via optical methods, this opens a whole new field of opportunity for non-destructive analysis of nanoparticle grain boundaries, which can be measured here *in situ* and under ambient conditions. This will open the way towards understanding how chemical reactions on surfaces can be affected by the surfaces themselves, with the sorts of interactions hinted at in Chapter 5.

Although this model is successful in explaining a number of the observed flare features, there are a number of issues not addressed. The increased likelihood of flares with age of nanoparticle is not understood, although it is possible that oxidative effects lead to a higher number of defects within the nanoparticle, leading to a higher number of flare modes observed. However, more research would be needed to ascertain whether defect numbers do in fact increase in this way, possibly through correlation with electron microscopy. Similarly it cannot explain why more flares are observed for different spacer molecules. It is likely that this difference is due to molecular binding to the gold (since purely molecular processes have been ruled out), but more understanding of this is needed.

Additionally, although the red-shift in λ_C is predicted by simulations, the coupled-mode observations are not entirely predicted by this model. In experimental observations flare modes are only observed in the 640-700 nm region, with broad-band white light required in order to observe the higher-wavelength coupled modes. It is true that there is a drop-off in ERS intensity further from the laser due to the increased momentum difference required; however, for there to be no remnant of ERS in the coupled-mode region (700-800 nm) a drastic drop-off would be required, inconsistent with the intensity of flare modes observed near to this region.

Additionally this model does not address why an increase in coupled-mode intensity is seen in the event of a flare. In fact simulations predict that all λ_C red-shifts should be seen alongside a *decrease* in intensity of the coupled mode. In light of this, we consider here an additional effect based on stimulated electronic Raman scattering.

7.5 Stimulated Electronic Raman Scattering

In order to explain the increase in coupled-mode strength seen in Figure 6.9, an additional process is considered here. It is noted that this increase in intensity at coupled-mode

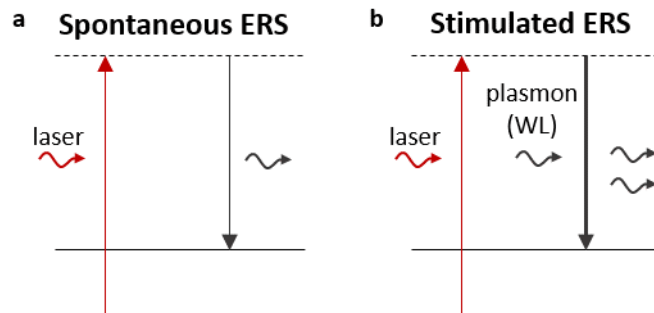


Fig. 7.10 **Stimulated Electronic Raman Scattering.** Mechanism for **a** spontaneous electronic Raman scattering background (as in Figure 7.3), and **b** stimulated electronic Raman scattering background, stimulated by the white-light via the plasmon.

wavelengths is only observed when the system is irradiated by laser and broad-band white light simultaneously. It is possible that alongside the ERS process leading to emission at the lower-wavelength flare modes, there is an additional *stimulated* electronic Raman-scattering (stimulated ERS) process occurring, such as that described by Figure 7.10. The process of stimulated ERS has been demonstrated with CW systems looking at dimers [137] and nanowires [138], by using two lasers: one to pump the system and another to stimulate emission. In the case here it is suggested that the incident white light is filtered by the λ_C plasmon to a single coherent mode, thus enabling the optical confinement to be high enough that it can stimulate emission from the excited state back to the ground state, emitting two photons at the λ_C wavelength. Although the process of CW stimulated ERS has been shown to occur in other studies, it is difficult to either prove or disprove whether this is what is happening here. In order to do so would require an experiment to be designed in which the system is pumped by two lasers: one at the original wavelength (633 nm) and the other to match the coupled-mode wavelength λ_C . The elastic scatter from the second laser would then need to be removed, but as this would not be possible spectrally it would need to be done via polarisation or k-space methods. An additional test for this mechanism would be to evaluate whether the *stimulated* ERS (that is the *additional* increase in λ_C mode seen at the time of a flare) were dependent on the white-light intensity, as would be expected for a stimulated process.

7.6 Conclusion and Outlook

In the previous chapter I introduced a new spectral feature, termed ‘flare’ modes, and characterised them through temporal and power-dependent measurements. In this chapter

I have presented a number of theories and models, in an attempt to explain the origin of these modes. There are multiple experimental features of these modes observed in Chapter 6, with the main features requiring explanation summarised at the start of this chapter. These include:

- The spectral range of flares observed
- No change to Raman lines observed
- The temporal dynamics of flare modes observed
- The increased likelihood of flares with sample age
- The variation in number of flares observed with different spacer molecules
- The observed changes to the coupled mode (λ_C) observed at the time of a flare event

In this chapter I have addressed and discussed a number of possibilities of flare origin with respect to these experimental observations. These possibilities are not exhaustive, and at this point there is no one model discussed here that can explain *all* observations. I aim here to discuss the possible models and give reasons as to why I believe some of them can be discounted.

In the first part of this chapter I looked into known optical effects including black-body radiation, two-photon absorption and emission, and hot-electron emission. Both black-body radiation and two-photon absorption are effects that might initially be proposed when considering this problem due to the spectral shape of the flare modes observed. However in both of these cases there is a mismatch between the predicted wavelength of the emitted light and what is actually observed. Additionally, molecular effects are ruled out due to the small degree of variation in flare wavelength seen when different molecular spacers are used. Hot-electron emission could feasibly be in the correct wavelength range for very small nanoparticles, but for the size of nanoparticles used here (80 nm) it is significantly higher in wavelength than the flare emission observed.

However, the main issue with these three theories is the inconsistencies with observed temporal distributions. Flares are shown to happen very infrequently, and when they do occur their lifetime is on the order of 30-50 ms. The lifetimes of these three processes mean that on the time-scales measured in experiments, the intensity of the flares would be expected to vary with incident laser power, but the temporal variation observed is not expected.

For all these reasons I propose that it is most likely that structural changes to the NPoM structure are initiating the flare events. In the following part of the chapter (Section 7.4) I suggest that the structural changes alter the plasmonic modes, thus altering the electronic

Raman scattering (ERS) emitted from the metal. A key feature to explain is why the intensity of the flare modes is greatly increased from the small ERS background usually seen. This is only possible when considering a small nanometre region of reduced ω_p , which matches a defect or grain-boundary region. Any sharp features such as those formed in the ‘pico-hole’ and ‘crack’ geometries (Sections 7.4.1, 7.4.2) would be expected to produce additional lines in the Raman spectra, something which is clearly not seen in experiment.

Patches of different sizes and with various reductions in ω_p are modelled and can be shown to support plasmonic modes in the flare region. The best fit to the data suggests patches of lateral size 2 – 4 nm and 25 – 30% reduction in local plasma frequency, ω_p . These characteristics are strongly indicative of the parameters expected at a grain boundary [121]. However this model cannot explain simply the feature that the observed coupled mode intensity increases at the time of a flare event. A possible explanation of this observation is an additional process of stimulated ERS, in which the scattering process is enhanced by the white-light filtered through the plasmon mode.

It should be additionally noted that the difference in *number* of flares observed with different spacer molecules is not addressed by any of these models. Although there is a degree of understanding that different molecular groups interact differently with the gold surface [117], demonstrated in Chapter 5, this is something that requires further investigation within the nanoparticle-on-mirror system.

From the evidence and discussion provided in Chapters 6, and 7, it is clear that a number of questions still remain as to the origin of these flare modes. However it has been shown that structural changes to the nanoparticle are the most likely candidates, with changes to the local plasma frequency caused by grain boundaries or surface defects successfully explaining a lot of the observed features.

Chapter 8

Conclusion and Outlook

In this thesis the enhancement of vibrational scattering for molecules placed in the vicinity of gold nanoparticles has been investigated. In order to maximise field enhancement, coupled nanostructures are used, in particular long chain nano-aggregates and nanoparticle-on-mirror constructs. The former are self-assembled via addition of cucurbit[n]uril (CB[n]) molecules to colloidal gold nanoparticles to form fractal-like aggregates supporting plasmonic ‘chain’ modes throughout the structure. Such CB[n] molecules have been shown to enable sequestration of analyte molecules, placing them directly in the plasmonic hot-spot for optimal plasmonic sensing.

In the first part of this thesis I have shown how the detection of synthetic cannabinoids can be reliably detected using gold nano-aggregates towards the nanomolar regime through integration of surface-enhanced Raman spectroscopy (SERS) techniques with principal-component-analysis (PCA) statistical methods. However slight inconsistencies between detection limits of different analyte molecules were observed, likely due to the relative size of the analyte molecule compared to the CB[n] encapsulator molecule, as well as differences in solubility. Moving forward it will be necessary to better understand the relative kinetics of nanoparticle, analyte molecule and CB[n] encapsulator, in order to further improve the viability of this system for the drug detection field.

As a further investigation into such nano-aggregates I have explored how the plasmonic field is altered by transferring them to a dry state, with particular focus on the effect of supporting substrates of different materials through SERS of the CB[7] spacer molecules. I have found that although noble metal substrates lead to higher detected SERS signals, it is in fact the hot-spots between adjacent nanoparticles which dominate over those between the nanoparticle and substrate. Additionally, I have shown that anchoring nano-aggregates to a substrate increases the measured SERS signal by three orders of magnitude, due to the increased number density measured within the focal spot of the objective. Such results

mean that careful choice of substrate is important when utilising nano-aggregates in a dry environment for plasmonic sensing.

As well as gold nanoparticle aggregates, I have utilised the nanoparticle-on-mirror (NPoM) construct for the final three results chapters in this thesis. The NPoM construct is formed by spacing a single nanoparticle above a flat gold film by a molecular spacer layer. The nanometric proximity of the nanoparticle induces image charges in the gold surface, leading to the formation of dimer-like plasmonic coupled modes. Under laser irradiation adatoms can protrude from the gold surfaces, leading to the formation of ‘picocavities’, with mode volumes calculated to be $< 1 \text{ nm}^3$ [18]. Such picocavities lead to additional spectral lines in the measured SERS spectra due to the field gradients experienced by single molecular bonds and the subsequent visibility of previously dark IR modes.

In the second part of this thesis I have shown that it is possible to observe these picocavities at room temperature and ambient conditions by pushing the limits of high-speed CW laser spectroscopy. Through careful choice of molecular spacer with a thiol head group and cyanine tail, we can analyse the resulting spectral lines and show that it is considerably more likely that the picocavity adatoms emerge from the surface of the flat gold film than the bottom facet of the nanoparticle.

There remain a number of questions to be answered here. By choosing a spacer molecule with different molecular head and tail groups it is possible to identify the spatial origin of the adatom, but it is not possible to know whether the choice of molecule is altering this result. Is it that the structure of the gold film makes it more susceptible to adatom formation than the nanoparticle? Or is it instead that the thiol head group which attaches to the gold film somehow initiates the picocavity formation? Both of these situations are possible, either together or separately. It is difficult to form NPoM structures with the molecular spacer completely reversed (thiol group on gold nanoparticle side, cyanine group towards gold film) due to the order in which the structure is formed and the higher bonding strength of the thiol group to gold. A possible technique may be to instead form the monolayer on the surface of the nanoparticle, before drop-casting the covered nanoparticles onto the gold film. However this requires exact knowledge of the concentrations needed for full nanoparticle surface coverage, as any free molecules in solution would be expected to attach thiol end down on to the gold mirror, resulting in a mixed monolayer and skewed results. An alternative control could be to form a spacer monolayer with both a cyanine head and tail and compare to see if results from this match results from Chapter 5. This would tell us whether the number of picocavities is indeed reduced by a cyanine group compared to a thiol.

As well as the additional lines occasionally observed in NPoM SERS spectra on the formation of a picocavity, I have shown that a further spectral feature can sometimes be observed. Unlike the picocavity lines, which are similar in linewidth to the nanocavity SERS lines, these new features (termed ‘flare’ modes) are Gaussian in shape and broader in width. The time-scale and incident laser power dependence is also different to that of a picocavity, with typical events lasting only 30-50 ms (compared to the > 1 s of picocavities) and observed much less often.

Although briefly seen in older work, these modes have been discounted, or put down to ‘experimental fluctuations’. In this thesis I have shown through detailed statistical analysis over thousands of nanoparticles with various molecular spacers that they are indeed a physical effect. I have presented here a number of possibilities as to the origin of these observed modes. Through ruling out a number of optical and structural effects as well as matching to theoretical models I conclude that the most probably cause of these flare modes is formation of nanoparticle grain defects which lead to a reduction in local plasma frequency. This increases light penetration into the metal and results in a subsequent increase in the emitted electronic Raman scattering (ERS) background observed.

However, it is clear that there is a degree of uncertainty around this model, with a number of discontinuities between experimentally observed results and predicted measurements. Most pressing of these is the large variation in flare events recorded for different spacer molecules, as well as the unexplained increase in NPoM coupled mode (λ_C) observed at the time of flare event.

It is possible that the latter of these issues can be explained through stimulated ERS, whereby the white light is filtered through the plasmon to stimulate emission at the coupled wavelength, λ_C . In order to prove this, an experiment could be designed whereby two lasers are used to irradiate the system. The first would excite the flare modes, as has been shown in Chapters 6 & 7. The second laser would be matched to the wavelength of the NPoM coupled mode, λ_C , resulting in stimulated electronic Raman scattering. Since the resulting scattered light would be at the same wavelength as the second laser it will be necessary to remove the laser light by non-spectral means. This can be done by k-space filtering or polarisation methods but is non-trivial. An alternative, perhaps simpler, experiment to prove the mechanism of stimulated ERS would be to analyse the proportionality in intensity seen around the λ_C wavelength at the time of the flare. If this is indeed due to stimulated ERS, it would be expected to be linear with white-light intensity.

The former of these issues hints towards the same questions asked of the variation in picocavity events: how do the spacer molecules interact with the gold surfaces? I have shown here how collection of large experimental data-sets and thorough statistical analysis

can be used to elucidate some of these answers. I have shown that molecules which bind directly to the gold surface (i.e. thiols) act differently in terms of both their picocavity and flare spectra when compared to those which rely on weaker binding forces (i.e. CB[n] + analyte composites). This is seen by the relative picocavity dynamics but also in the different distributions in flare spectral wavelength observed. In order to understand the NPoM system more fully it is my belief that this is an area which should be studied further. As well as having implications for flares and picocavities within the NPoM system it is also important to understand for plasmonic sensing with CB[n] molecules within the nano-aggregates systems.

Throughout this thesis I have designed experiments and developed techniques to measure molecular dynamics far below the diffraction limit. I have shown how surface-enhanced spectroscopies, in particular surface-enhanced Raman spectroscopy and analysis of the newly discovered ‘flare’ modes, can be used to probe metallic surface dynamics on the nanoscale. Although some defects have been imaged via other methods, optical detection opens the doors to the use of non-destructive *in situ* methods under room temperatures and ambient conditions. These methods have significant implications for a large variety of experiments, giving insight into new ways to study chemistry at metal surfaces.

References

- [1] Robert Hooke. *Micrographia: or, some physiological descriptions of minute bodies made by magnifying glasses*. 1665.
- [2] M Faraday. Thoughts on Ray Vibrations. *Philosophical Magazine*, 28, 1846.
- [3] Bhavya Sharma, Renee R. Frontiera, Anne-Isabelle Henry, Emilie Ringe, and Richard P. Van Duyne. SERS: Materials, applications, and the future. *Materials Today*, 15(1-2):16–25, jan 2012.
- [4] J. J. Mock, M. Barbic, D. R. Smith, D. A. Schultz, and S. Schultz. Shape effects in plasmon resonance of individual colloidal silver nanoparticles. *The Journal of Chemical Physics*, 116(15):6755–6759, apr 2002.
- [5] C. V. Raman and K. S. Krishnan. A new type of secondary radiation. *Nature*, 121(3048):501–502, mar 1928.
- [6] James Bohning. The Raman Effect. *ACS - An International Historic Chemical Landmark*.
- [7] The Nobel Prize in Physics.
- [8] A. L. Schawlow and C. H. Townes. Infrared and optical masers. *Physical Review*, 1958.
- [9] R Gordon Gould et al. The laser, light amplification by stimulated emission of radiation. In *The Ann Arbor conference on optical pumping, the University of Michigan*, volume 15, page 128, 1959.
- [10] A. Sommerfeld. Ueber die Fortpflanzung elektrodynamischer Wellen längs eines Drahtes. *Annalen der Physik und Chemie*, 303(2):233–290, jan 1899.
- [11] J. Zenneck. Über die Fortpflanzung ebener elektromagnetischer Wellen längs einer ebenen Leiterfläche und ihre Beziehung zur drahtlosen Telegraphie. *Annalen der Physik*, 328(10):846–866, jan 1907.
- [12] R. H. Ritchie. Plasma Losses by Fast Electrons in Thin Films. *Physical Review*, 106(5):874–881, jun 1957.
- [13] E. Kretschmann. The angular dependence and the polarisation of light emitted by surface plasmons on metals due to roughness. *Optics Communications*, 5(5):331–336, aug 1972.

- [14] A. James McQuillan. The discovery of surface-enhanced Raman scattering. *Notes and Records of the Royal Society*, 2009.
- [15] Kuo-Chen Chou. Low-frequency collective motion in biomacromolecules and its biological functions. *Biophysical Chemistry*, 30(1):3–48, may 1988.
- [16] Rishabh Jain, Diego Calderon, Patricia R. Kierski, Michael J. Schurr, Charles J. Czuprynski, Christopher J. Murphy, Jonathan F. McAnulty, and Nicholas L. Abbott. Raman Spectroscopy Enables Noninvasive Biochemical Characterization and Identification of the Stage of Healing of a Wound. *Analytical Chemistry*, 86(8):3764–3772, apr 2014.
- [17] Duo Lin, Shangyuan Feng, Hao Huang, Weisheng Chen, Hong Shi, Nenrong Liu, Long Chen, Weiwei Chen, Yun Yu, and Rong Chen. Label-Free Detection of Blood Plasma Using Silver Nanoparticle Based Surface-Enhanced Raman Spectroscopy for Esophageal Cancer Screening. *Journal of Biomedical Nanotechnology*, 10(3):478–484, mar 2014.
- [18] Felix Benz, Mikolaj K Schmidt, Alexander Dreismann, Rohit Chikkaraddy, Yao Zhang, Angela Demetriadou, Cloudy Carnegie, Hamid Ohadi, Bart De Nijs, Ruben Esteban, Javier Aizpurua, and Jeremy J Baumberg. Single-molecule optomechanics in "picocavities". *Science*, 354(6313):726–729, nov 2016.
- [19] P. B. Johnson and R. W. Christy. Optical Constants of the Noble Metals. *Physical Review B*, 6(12):4370–4379, dec 1972.
- [20] M. A. Ordal, Robert J. Bell, R. W. Alexander, L. L. Long, and M. R. Querry. Optical properties of fourteen metals in the infrared and far infrared: Al, Co, Cu, Au, Fe, Pb, Mo, Ni, Pd, Pt, Ag, Ti, V, and W. *Applied Optics*, 24(24):4493, dec 1985.
- [21] Anatoly V Zayats and Igor I Smolyaninov. Near-field photonics: surface plasmon polaritons and localized surface plasmons. *Journal of Optics A: Pure and Applied Optics*, 5(4):S16–S50, jul 2003.
- [22] Xi Wang, Yang Deng, Qitong Li, Yijing Huang, Zilun Gong, Kyle B. Tom, and Jie Yao. Excitation and propagation of surface plasmon polaritons on a non-structured surface with a permittivity gradient. *Light: Science and Applications*, 5(12):e16179–e16179, dec 2016.
- [23] Jack J. Mock, David R. Smith, and Sheldon Schultz. Local refractive index dependence of plasmon resonance spectra from individual nanoparticles. *Nano Letters*, 3(4):485–491, 2003.
- [24] Surbhi Lal, Stephan Link, and Naomi J. Halas. Nano-optics from sensing to waveguiding. *Nature Photonics*, 1(11):641–648, nov 2007.
- [25] Craig F. Bohren and Donald R. Huffman, editors. *Absorption and Scattering of Light by Small Particles*. Wiley-VCH Verlag GmbH, Weinheim, Germany, apr 1998.
- [26] Stefan Alexander. Maier. *Plasmonics : fundamentals and applications*. Springer, 2007.

- [27] S. Nie and Steven R. Emory. Probing Single Molecules and Single Nanoparticles by Surface-Enhanced Raman Scattering. *Science*, 275(February):1102–1106, 1997.
- [28] Katrin Kneipp, Yang Wang, Harald Kneipp, Lev T. Perelman, Irving Itzkan, Ramachandra R. Dasari, and Michael S. Feld. Single Molecule Detection Using Surface-Enhanced Raman Scattering (SERS). *Physical Review Letters*, 78(9):1667–1670, mar 1997.
- [29] Hyun Hang Shin, Gyu Jin Yeon, Han Kyu Choi, Sang Min Park, Kang Sup Lee, and Zee Hwan Kim. Frequency-Domain Proof of the Existence of Atomic-Scale SERS Hot-Spots. *Nano Letters*, 18(1):262–271, 2018.
- [30] Amir Weiss and Gilad Haran. Time-dependent single-molecule Raman scattering as a probe of surface dynamics. *Journal of Physical Chemistry B*, 105(49):12348–12354, 2001.
- [31] V. Matarazzo, S. De Nicola, G. Zito, P. Mormile, M. Rippa, G. Abbate, J. Zhou, and L. Petti. Spectral characterization of two-dimensional Thue-Morse quasicrystals realized with high resolution lithography. *Journal of Optics*, 13(1), 2011.
- [32] David P Fromm, Arvind Sundaramurthy, P. James Schuck, Gordon Kino, and W E Moerner. Gap-dependent optical coupling of single "bowtie" nanoantennas resonant in the visible. *Nano Letters*, 4(5):957–961, 2004.
- [33] Wenqi Zhu, Mohamad G. Banaee, Dongxing Wang, Yizhuo Chu, and Kenneth B. Crozier. Lithographically fabricated optical antennas with gaps well below 10 nm. *Small*, 7(13):1761–1766, jul 2011.
- [34] Lee Weller, Vivek V Thacker, Lars O Herrmann, Elisa A Hemmig, Anna Lombardi, Ulrich F Keyser, and Jeremy J Baumberg. Gap-Dependent Coupling of Ag-Au Nanoparticle Heterodimers Using DNA Origami-Based Self-Assembly. *ACS Photonics*, 3(9):1589–1595, 2016.
- [35] Syed Rahin Ahmed, Jeonghyo Kim, Van Tan Tran, Tetsuro Suzuki, Suresh Neethirajan, Jaebeom Lee, and Enoch Y. Park. In situ self-assembly of gold nanoparticles on hydrophilic and hydrophobic substrates for influenza virus-sensing platform. *Scientific Reports*, 7(1):44495, dec 2017.
- [36] Felix Benz, Christos Tserkezis, Lars O. Herrmann, Bart De Nijs, Alan Sanders, Daniel O. Sigle, Laurynas Pukenas, Stephen D. Evans, Javier Aizpurua, and Jeremy J. Baumberg. Nanooptics of molecular-shunted plasmonic nanojunctions. *Nano Letters*, 15(1):669–674, jan 2015.
- [37] Richard W Taylor, Rubén Esteban, Sumeet Mahajan, Roger Coulston, Oren A Scherman, Javier Aizpurua, and Jeremy J Baumberg. Simple composite dipole model for the optical modes of strongly-coupled plasmonic nanoparticle aggregates. *Journal of Physical Chemistry C*, 116(47):25044–25051, 2012.
- [38] Mengmeng Sun, Fei Liu, Yukun Zhu, Wansheng Wang, Jin Hu, Jing Liu, Zhifei Dai, Kun Wang, Yen Wei, Jing Bai, and Weiping Gao. Salt-induced aggregation of gold nanoparticles for photoacoustic imaging and photothermal therapy of cancer. *Nanoscale*, 8(8):4452–4457, feb 2016.

- [39] Cloudy Carnegie, Rohit Chikkaraddy, Felix Benz, Bart De Nijs, William M. Deacon, Matthew Horton, Wenting Wang, Charlie Readman, Steven J. Barrow, Oren A. Scherman, and Jeremy J. Baumberg. Mapping SERS in CB: Au Plasmonic Nanoaggregates. *ACS Photonics*, 4(11):2681–2686, nov 2017.
- [40] Han Kyu Choi, Won Hwa Park, Chan Gyu Park, Hyun Hang Shin, Kang Sup Lee, and Zee Hwan Kim. Metal-Catalyzed Chemical Reaction of Single Molecules Directly Probed by Vibrational Spectroscopy. *Journal of the American Chemical Society*, 138(13):4673–4684, 2016.
- [41] Rohit Chikkaraddy, Bart de Nijs, Felix Benz, Steven J. Barrow, Oren A. Scherman, Edina Rosta, Angela Demetriadou, Peter Fox, Ortwin Hess, and Jeremy J. Baumberg. Single-molecule strong coupling at room temperature in plasmonic nanocavities. *Nature*, 535(7610):127–130, jul 2016.
- [42] Bin Dong, Yurui Fang, Xiaowei Chen, Hongxing Xu, and Mengtao Sun. Substrate-, wavelength-, and time-dependent plasmon-assisted surface catalysis reaction of 4-nitrobenzenethiol dimerizing to p,p- dimercaptoazobenzene on Au, Ag, and Cu films. *Langmuir*, 27(17):10677–10682, sep 2011.
- [43] Felix Benz, Bart de Nijs, Christos Tserkezis, Rohit Chikkaraddy, Daniel O. Sigle, Laurynas Pukenas, Stephen D. Evans, Javier Aizpurua, and Jeremy J. Baumberg. Generalized circuit model for coupled plasmonic systems. *Optics Express*, 23(26):33255, dec 2015.
- [44] Kevin J. Savage, Matthew M. Hawkeye, Rubén Esteban, Andrei G. Borisov, Javier Aizpurua, and Jeremy J. Baumberg. Revealing the quantum regime in tunnelling plasmonics. *Nature*, 491(7425):574–577, nov 2012.
- [45] Prashant K. Jain, Wenyu Huang, and Mostafa A. El-Sayed. On the universal scaling behavior of the distance decay of plasmon coupling in metal nanoparticle pairs: A plasmon ruler equation. *Nano Letters*, 7(7):2080–2088, 2007.
- [46] Marie Elena Kleemann, Rohit Chikkaraddy, Evgeny M. Alexeev, Dean Kos, Cloudy Carnegie, Will Deacon, Alex Casalis De Pury, Christoph Große, Bart De Nijs, Jan Mertens, Alexander I. Tartakovskii, and Jeremy J. Baumberg. Strong-coupling of WSe₂ in ultra-compact plasmonic nanocavities at room temperature. *Nature Communications*, 8(1):1296, dec 2017.
- [47] Felix Benz, Rohit Chikkaraddy, Andrew Salmon, Hamid Ohadi, Bart de Nijs, Jan Mertens, Cloudy Carnegie, Richard W. Bowman, and Jeremy J. Baumberg. SERS of Individual Nanoparticles on a Mirror: Size Does Matter, but so Does Shape. *The Journal of Physical Chemistry Letters*, 7(12):2264–2269, jun 2016.
- [48] J. Mertens, A. Demetriadou, R. W. Bowman, F. Benz, M. E. Kleemann, C. Tserkezis, Y. Shi, H. Y. Yang, O. Hess, J. Aizpurua, and J. J. Baumberg. Tracking Optical Welding through Groove Modes in Plasmonic Nanocavities. *Nano Letters*, 16(9):5605–5611, sep 2016.

- [49] Mattin Urbietta, Marc Barbry, Yao Zhang, Peter Koval, Daniel Sánchez-Portal, Nerea Zabala, and Javier Aizpurua. Atomic-Scale Lightning Rod Effect in Plasmonic Picocavities: A Classical View to a Quantum Effect. *ACS Nano*, 12(1):585–595, jan 2018.
- [50] John Turkevich, Peter Cooper Stevenson, and James Hillier. A study of the nucleation and growth processes in the synthesis of colloidal gold. *Discussions of the Faraday Society*, 11(0):55, jan 1951.
- [51] Xinyi Dong, Xiaohui Ji, Hongli Wu, Lili Zhao, Jun Li, and Wensheng Yang. Shape Control of Silver Nanoparticles by Stepwise Citrate Reduction. *The Journal of Physical Chemistry C*, 113(16):6573–6576, apr 2009.
- [52] You-Jin Lee, Nicholas B. Schade, Li Sun, Jonathan A. Fan, Doo Ri Bae, Marcelo M. Mariscal, Gaehang Lee, Federico Capasso, Stefano Sacanna, Vinothan N. Manoharan, and Gi-Ra Yi. Ultrasoother, Highly Spherical Monocrystalline Gold Particles for Precision Plasmonics. *ACS Nano*, 7(12):11064–11070, dec 2013.
- [53] Marie-Elena Kleemann, Jan Mertens, Xuezhi Zheng, Sean Cormier, Vladimir Turek, Felix Benz, Rohit Chikkaraddy, William Deacon, Anna Lombardi, Victor V. Moshchalkov, Guy A. E. Vandenbosch, and Jeremy J. Baumberg. Revealing Nanostructures through Plasmon Polarimetry. *ACS Nano*, 11(1):850–855, jan 2017.
- [54] Marek Grzelczak, Jorge Pérez-Juste, Paul Mulvaney, and Luis M. Liz-Marzán. Shape control in gold nanoparticle synthesis. *Chemical Society Reviews*, 37(9):1783, aug 2008.
- [55] Kwangyeol Lee, Minsik Kim, and Heonjo Kim. Catalytic nanoparticles being facet-controlled. *Journal of Materials Chemistry*, 20(19):3791, may 2010.
- [56] Peter Vandenabeele, Howell G.M. Edwards, and Luc Moens. A decade of Raman spectroscopy in art and archeology, 2007.
- [57] L.-P. Choo-Smith, H. G. M. Edwards, H. P. Endtz, J. M. Kros, F. Heule, H. Barr, J. S. Robinson, H. A. Bruining, and G. J. Puppels. Medical applications of Raman spectroscopy: From proof of principle to clinical implementation. *Biopolymers*, 67(1):1–9, jan 2002.
- [58] Bart de Nijs, Cloudy Carnegie, István Szabó, Rohit Chikkaraddy, David Gryns, Marlous Kamp, Charlie Readman, Marie-Elena Kleemann, Oren A. Scherman, Edina Rosta, and Jeremy J. Baumberg. Chemically Tailoring Plasmonic Hotspots for SERS sensing. *Submitted (ACS Nano)*, 2019.
- [59] Bart De Nijs, Felix Benz, Steven J Barrow, Daniel O Sigle, Rohit Chikkaraddy, Aniello Palma, Cloudy Carnegie, Marlous Kamp, Ravishankar Sundararaman, Prineha Narang, Oren A Scherman, and Jeremy J Baumberg. Plasmonic tunnel junctions for single-molecule redox chemistry. *Nature Communications*, 8(1), 2017.
- [60] James T. Hugall and Jeremy J. Baumberg. Demonstrating Photoluminescence from Au is Electronic Inelastic Light Scattering of a Plasmonic Metal: The Origin of SERS Backgrounds. *Nano Letters*, 15(4):2600–2604, apr 2015.

- [61] Jan Mertens, Marie-Elena Kleemann, Rohit Chikkaraddy, Prineha Narang, and Jeremy J. Baumberg. How Light Is Emitted by Plasmonic Metals. *Nano Letters*, 17(4):2568–2574, apr 2017.
- [62] Peter F. Bernath and Joseph L. Knee. Spectra of Atoms and Molecules. *American Journal of Physics*, 1996.
- [63] Anna Lombardi, Angela Demetriadou, Lee Weller, Patrick Andrae, Felix Benz, Rohit Chikkaraddy, Javier Aizpurua, and Jeremy J Baumberg. Anomalous Spectral Shift of Near- And Far-Field Plasmonic Resonances in Nanogaps. *ACS Photonics*, 3(3):471–477, 2016.
- [64] Mikolaj K. Schmidt, Ruben Esteban, Alejandro González-Tudela, Geza Giedke, and Javier Aizpurua. Quantum Mechanical Description of Raman Scattering from Molecules in Plasmonic Cavities. *ACS Nano*, 10(6):6291–6298, jun 2016.
- [65] Philippe Roelli, Christophe Galland, Nicolas Piro, and Tobias J. Kippenberg. Molecular cavity optomechanics as a theory of plasmon-enhanced Raman scattering. *Nature Nanotechnology*, 11(2):164–169, feb 2016.
- [66] Yuqing Cheng, Jingyi Zhao, Te Wen, Guantao Li, Jianning Xu, Aiqin Hu, Qihuang Gong, and Guowei Lu. Enhanced Light Emission from Plasmonic Nanostructures by Molecules. *Journal of Physical Chemistry C*, 121(42):23626–23632, 2017.
- [67] Cucurbituril, sigma aldrich. <https://www.sigmaaldrich.com/catalog/product/aldrich/545228?lang=en®ion=GB>. Accessed: 2018-12-10.
- [68] Steven J. Barrow, Setu Kasera, Matthew J. Rowland, Jesús Del Barrio, and Oren A. Scherman. Cucurbituril-Based Molecular Recognition. *Chemical Reviews*, 115(22):12320–12406, nov 2015.
- [69] Richard W. Taylor, Tung Chun Lee, Oren A. Scherman, Ruben Esteban, Javier Aizpurua, Fu Min Huang, Jeremy J. Baumberg, and Sumeet Mahajan. Precise subnanometer plasmonic junctions for SERS within gold nanoparticle assemblies using cucurbit[n]uril "glue". *ACS Nano*, 5(5):3878–3887, may 2011.
- [70] Stefan Knoppe and Thomas Burgi. Chirality in thiolate-protected gold clusters. *Accounts of Chemical Research*, 47(4):1318–1326, apr 2014.
- [71] Thomas Bürgi. Properties of the gold-sulphur interface: from self-assembled monolayers to clusters. *Nanoscale*, 7(38):15553–15567, 2015.
- [72] John Schaibley and Xiaodong Xu. Spintronics: A lucky break. *Nature Physics*, 10(11):798–799, nov 2014.
- [73] Charlie Readman, Bart de Nijs, István Szabó, Angela Demetriadou, Ryan Greenhalgh, Colm Durkan, Edina Rosta, Oren A. Scherman, and Jeremy J. Baumberg. Anomalous Large Spectral Shifts near the Quantum Tunnelling Limit in Plasmonic Rulers with Subatomic Resolution. *Nano Letters*, page 2051–2058, feb 2019.

- [74] Andrea C. Ferrari. Raman spectroscopy of graphene and graphite: Disorder, electron-phonon coupling, doping and nonadiabatic effects. *Solid State Communications*, 143(1-2):47–57, jul 2007.
- [75] Grain boundary mediated hydriding phase transformations in individual polycrystalline metal nanoparticles. *Nature Communications*, 8(1):1084, dec 2017.
- [76] Jianwei Miao, Peter Ercius, and Simon J.L. Billinge. Atomic electron tomography: 3D structures without crystals. *Science*, 353(6306), 2016.
- [77] K. Lu. Stabilizing nanostructures in metals using grain and twin boundary architectures. *Nature Reviews Materials*, 1(5):16019, may 2016.
- [78] M. A. Tschopp and D. L. McDowell. Asymmetric tilt grain boundary structure and energy in copper and aluminium. *Philosophical Magazine*, 87(25):3871–3892, sep 2007.
- [79] Zongrui Pei, Xie Zhang, Tilmann Hickel, Martin Friák, Stefanie Sandlöbes, Biswanath Dutta, and Jörg Neugebauer. Atomic structures of twin boundaries in hexagonal close-packed metallic crystals with particular focus on Mg. *npj Computational Materials*, 3(1):6, dec 2017.
- [80] Rohit Chikkaraddy, Xuezhi Zheng, Felix Benz, Laura J. Brooks, Bart De Nijs, Cloudy Carnegie, Marie Elena Kleemann, Jan Mertens, Richard W. Bowman, Guy A.E. Vandenbosch, Victor V. Moshchalkov, and Jeremy J. Baumberg. How Ultranarrow Gap Symmetries Control Plasmonic Nanocavity Modes: From Cubes to Spheres in the Nanoparticle-on-Mirror. *ACS Photonics*, 4(3):469–475, mar 2017.
- [81] Ulrich Hohenester and Andreas Trügler. MNPBEM - A Matlab toolbox for the simulation of plasmonic nanoparticles. *Computer Physics Communications*, 183(2):370–381, 2012.
- [82] Edward D. Palik. *Handbook of optical constants of solids*. Academic Press, 1998.
- [83] Nina Hüsken, Richard W. Taylor, Dodzi Zigah, Jean-Christophe Taveau, Olivier Lambert, Oren A. Scherman, Jeremy J. Baumberg, and Alexander Kuhn. Electrokinetic Assembly of One-Dimensional Nanoparticle Chains with Cucurbit[7]uril Controlled Subnanometer Junctions. *Nano Letters*, 13(12):6016–6022, dec 2013.
- [84] Martin Moskovits. Surface-enhanced Raman spectroscopy: A brief retrospective. *Journal of Raman Spectroscopy*, 36(6-7):485–496, jun 2005.
- [85] Surface-Enhanced Raman Spectroscopy. *Annual Review of Analytical Chemistry*, 1(1):601–626, jul 2008.
- [86] Chad A. Mirkin, Robert L. Letsinger, Robert C. Mucic, and James J. Storhoff. A DNA-based method for rationally assembling nanoparticles into macroscopic materials. *Nature*, 382(6592):607–609, aug 1996.
- [87] Kadir Aslan, Claudia C Luhrs, and Víctor H Pérez-Luna. Controlled and reversible aggregation of biotinylated gold nanoparticles with streptavidin. *Journal of Physical Chemistry B*, 108(40):15631–15639, 2004.

- [88] Hongxing Xu, Erik J. Bjerneld, Mikael Käll, and Lars Börjesson. Spectroscopy of Single Hemoglobin Molecules by Surface Enhanced Raman Scattering. *Physical Review Letters*, 83(21):4357–4360, nov 1999.
- [89] Karen Faulds, Rachael E. Littleford, Duncan Graham, Geoffrey Dent, and W. Ewen Smith. Comparison of Surface-Enhanced Resonance Raman Scattering from Unaggregated and Aggregated Nanoparticles. *Analytical Chemistry*, 76(3):592–598, 2004.
- [90] Lanlan Sun, Yonghai Song, Li Wang, Cunlan Guo, Yujing Sun, Zhuang Li, and Zhelin Liu. Ethanol-induced formation of silver nanoparticle aggregates for highly active SERS substrates and application in DNA detection. *Journal of Physical Chemistry C*, 112(5):1415–1422, 2008.
- [91] Jonathan A Fan, Chihhui Wu, Kui Bao, Jiming Bao, Rizia Bardhan, Naomi J Halas, Vinothan N Manoharan, Peter Nordlander, Gennady Shvets, and Federico Capasso. Self-assembled plasmonic nanoparticle clusters. *Science*, 328(5982):1135–1138, may 2010.
- [92] Ying Fang, Nak Hyun Seong, and Dana D. Dlott. Measurement of the distribution of site enhancements in surface-enhanced raman scattering. *Science*, 321(5887):388–392, jul 2008.
- [93] Linhan Lin, Xiaolei Peng, Mingsong Wang, Leonardo Scarabelli, Zhangming Mao, Luis M. Liz-Marzán, Michael F. Becker, and Yuebing Zheng. Light-Directed Reversible Assembly of Plasmonic Nanoparticles Using Plasmon-Enhanced Thermophoresis. *ACS Nano*, 10(10):9659–9668, oct 2016.
- [94] Ruben Esteban, Richard W Taylor, Jeremy J Baumberg, and Javier Aizpurua. How chain plasmons govern the optical response in strongly interacting self-assembled metallic clusters of nanoparticles. *Langmuir*, 28(24):8881–8890, 2012.
- [95] Sezin Yuksel, Almut M. Schwenke, Guido Soliveri, Silvia Ardizzone, Karina Weber, Dana Cialla-May, Stephanie Hoepfener, Ulrich S. Schubert, and Jurgen Popp. Trace detection of tetrahydrocannabinol (THC) with a SERS-based capillary platform prepared by the in situ microwave synthesis of AgNPs. *Analytica Chimica Acta*, 939:93–100, oct 2016.
- [96] Ian Jolliffe. Principal Component Analysis. In *International Encyclopedia of Statistical Science*, pages 1094–1096. Springer Berlin Heidelberg, Berlin, Heidelberg, 2011.
- [97] Hervé Abdi and Lynne J. Williams. Principal component analysis. *Wiley Interdisciplinary Reviews: Computational Statistics*, 2(4):433–459, jul 2010.
- [98] Svante Wold, Kim Esbensen, and Paul Geladi. *Principal Component Analysis*. 2012.
- [99] I.C. Prentice. Non-Metric Ordination Methods in Ecology. *The Journal of Ecology*, 65(1):85–94, mar 1977.
- [100] K. G. Joreskog, J. E. Klován, and R. A. Reymont. *Geological factor analysis*. Elsevier Scientific Pub. Co, 1976.

- [101] L. Eriksson, E. Johansson, N. Kettaneh-Wold, J. Trygg, C. Wikström and S. Wold. *Multi- and Megavariate Data Analysis Part I: Basic Principles and Applications*. 2006.
- [102] Destari Pratiwi, J. Paul Fawcett, Keith C Gordon, and Thomas Rades. Quantitative analysis of polymorphic mixtures of ranitidine hydrochloride by Raman spectroscopy and principal components analysis. *European Journal of Pharmaceutics and Biopharmaceutics*, 54(3):337–341, nov 2002.
- [103] Shangyuan Feng, Rong Chen, Juqiang Lin, Jianji Pan, Guannan Chen, Yongzeng Li, Min Cheng, Zufang Huang, Jiesi Chen, and H. Zeng Haishan. Nasopharyngeal cancer detection based on blood plasma surface-enhanced Raman spectroscopy and multivariate analysis. *Biosensors and Bioelectronics*, 25(11):2414–2419, jul 2010.
- [104] Geurt Deinum, Daniel Rodriguez, Tjeerd J. Römer, Maryann Fitzmaurice, John R. Kramer, and Michael S. Feld. Histological Classification of Raman Spectra of Human Coronary Artery Atherosclerosis Using Principal Component Analysis. *Applied Spectroscopy*, 53(8):938–942, aug 1999.
- [105] Nathan Halko, Per-Gunnar Martinsson, and Joel A. Tropp. Finding structure with randomness: Probabilistic algorithms for constructing approximate matrix decompositions. *arXiv*, arXiv:0909, sep 2009.
- [106] Andrew R. Salmon, Ruben Esteban, Richard W. Taylor, James T. Hugall, Clive A. Smith, Graeme Whyte, Oren A. Scherman, Javier Aizpurua, Chris Abell, and Jeremy J. Baumberg. Monitoring Early-Stage Nanoparticle Assembly in Microdroplets by Optical Spectroscopy and SERS. *Small*, 12(13):1788–1796, apr 2016.
- [107] Setu Kasera, Frank Biedermann, Jeremy J. Baumberg, Oren A. Scherman, and Sumeet Mahajan. Quantitative SERS Using the Sequestration of Small Molecules Inside Precise Plasmonic Nanoconstructs. *Nano Letters*, 12(11):5924–5928, nov 2012.
- [108] Sumeet Mahajan, Robin M Cole, Jonathon D Speed, Suzanne H Pelfrey, Andrea E Russell, Philip N Bartlett, Stephen M Barnett, and Jeremy J Baumberg. Understanding the surface-enhanced Raman spectroscopy "background". *Journal of Physical Chemistry C*, 114(16):7242–7250, 2010.
- [109] Robin M Pope and Edward S Fry. Absorption spectrum 380-700 nm of pure water. II. Integrating cavity measurements. *Applied Optics*, 36(33):8710–8723, 1997.
- [110] Linhong Kou, Daniel Labrie, and Petr Chylek. Refractive indices of water and ice in the 0.65- to 25- μm spectral range. *Applied Optics*, 32(19):3531, jul 1993.
- [111] Bart De Nijs, Richard W Bowman, Lars O Herrmann, Felix Benz, Steve J Barrow, Jan Mertens, Daniel O Sigle, Rohit Chikkaraddy, Anna Eiden, Andrea Ferrari, Oren A Scherman, and Jeremy J Baumberg. Unfolding the contents of sub-nm plasmonic gaps using normalising plasmon resonance spectroscopy. *Faraday Discussions*, 178:185–193, 2015.

- [112] Richard W. Taylor, Rubén Esteban, Sumeet Mahajan, Javier Aizpurua, and Jeremy J. Baumberg. Optimizing SERS from Gold Nanoparticle Clusters: Addressing the Near Field by an Embedded Chain Plasmon Model. *The Journal of Physical Chemistry C*, 120(19):10512–10522, may 2016.
- [113] Cloudy Carnegie, Jack Griffiths, Bart de Nijs, Charlie Readman, Rohit Chikkaraddy, William M. Deacon, Yao Zhang, István Szabó, Edina Rosta, Javier Aizpurua, and Jeremy J. Baumberg. Room-Temperature Optical Picocavities below 1 nm³ Accessing Single-Atom Geometries. *The Journal of Physical Chemistry Letters*, 9(24):7146–7151, dec 2018.
- [114] C. Tserkezis, R. Esteban, D. O. Sigle, J. Mertens, L. O. Herrmann, J. J. Baumberg, and J. Aizpurua. Hybridization of plasmonic antenna and cavity modes: Extreme optics of nanoparticle-on-mirror nanogaps. *Physical Review A - Atomic, Molecular, and Optical Physics*, 92(5):053811, nov 2015.
- [115] Abraham Ulman. Formation and Structure of Self-Assembled Monolayers. *Chemical Reviews*, 96(4):1533–1554, 1996.
- [116] Hannu Häkkinen. The gold–sulfur interface at the nanoscale. *Nature Chemistry*, 4(6):443–455, jun 2012.
- [117] Evangelina Pensa, Emiliano Cortés, Gastón Corthey, Pilar Carro, Carolina Vericat, Mariano H. Fonticelli, Guillermo Benítez, Aldo A. Rubert, and Roberto C. Salvarezza. The Chemistry of the Sulfur–Gold Interface: In Search of a Unified Model. *Accounts of Chemical Research*, 45(8):1183–1192, aug 2012.
- [118] J. Christopher Love, Lara A. Estroff, Jennah K. Kriebel, Ralph G. Nuzzo, and George M. Whitesides. Self-assembled monolayers of thiolates on metals as a form of nanotechnology. *Chemical Reviews*, 105(4):1103–1169, 2005.
- [119] C. B. Harris, R. M. Shelby, and P. A. Cornelius. Effects of Energy Exchange on Vibrational Dephasing Times in Raman Scattering. *Physical Review Letters*, 38(24):1415–1419, jun 1977.
- [120] Kyoung Duck Park, Eric A Muller, Vasily Kravtsov, Paul M Sass, Jens Dreyer, Joanna M Atkin, and Markus B Raschke. Variable-Temperature Tip-Enhanced Raman Spectroscopy of Single-Molecule Fluctuations and Dynamics. *Nano Letters*, 16(1):479–487, 2016.
- [121] Ola Hunderi. Influence of grain boundaries and lattice defects on the optical properties of some metals. *Physical Review B*, 7(8):3419–3429, 1973.
- [122] L D Marks. Experimental studies of small particle structures. *Reports on Progress in Physics*, 57(6):603–649, jun 1994.
- [123] L D Marks. Surface structure and energetics of multiply twinned particles. *Philosophical Magazine A: Physics of Condensed Matter, Structure, Defects and Mechanical Properties*, 49(1):81–93, 1984.
- [124] P M Ajayan and L D Marks. Quasimelting and Phases of Small Particles P. *Phys. Rev. Lett.*, 60(7):585–587, 1987.

- [125] Aldo Serenelli, Rene Rohrmann, and Masataka Fukugita. On the nature of the black-body stars. *arXiv*, page arXiv:1804.01236, apr 2018.
- [126] Maria Göppert-Mayer. Über Elementarakte mit zwei Quantensprüngen. *Annalen der Physik*, 401(3):273–294, jan 1931.
- [127] W. Kaiser and C. G. B. Garrett. Two-photon excitation in CaF₂: Eu²⁺. *Physical Review Letters*, 7(6):229–231, sep 1961.
- [128] I. D. Abella. Optical Double-Photon Absorption in Cesium Vapor. *Physical Review Letters*, 9(11):453–455, dec 1962.
- [129] Alejandro Manjavacas, Jun G Liu, Vikram Kulkarni, and Peter Nordlander. Plasmon-induced hot carriers in metallic nanoparticles. *ACS Nano*, 8(8):7630–7638, 2014.
- [130] Kyle Marchuk and Katherine A. Willets. Localized surface plasmons and hot electrons. *Chemical Physics*, 445:95–104, dec 2014.
- [131] J. Mertens, A. Demetriadou, R. W. Bowman, F. Benz, M.-E. Kleemann, C. Tserkezis, Y. Shi, H. Y. Yang, O. Hess, J. Aizpurua, and J. J. Baumberg. Tracking Optical Welding through Groove Modes in Plasmonic Nanocavities. *Nano Letters*, 16(9):5605–5611, sep 2016.
- [132] Yi-Yu Cai, Eric Sung, Runmin Zhang, Lawrence J. Tauzin, Jun G. Liu, Behnaz Ostovar, Yue Zhang, Wei-Shun Chang, Peter Nordlander, and Stephan Link. Anti-Stokes Emission from Hot Carriers in Gold Nanorods. *Nano Letters*, 19(2):1067–1073, feb 2019.
- [133] D. Holec, P. Dumitraschkewitz, F. D. Fischer, and D. Vollath. Size-dependent surface energies of Au nanoparticles. *arXiv*, dec 2014.
- [134] Structure of a thiol monolayer-protected gold nanoparticle at 1.1 Å resolution. *Science*, 318(5849):430–433, oct 2007.
- [135] Bart Goris, Jan De Beenhouwer, Annick De Backer, Daniele Zanaga, K Joost Batenburg, Ana Sa, Luis M Liz-Marza, Sandra Van Aert, Sara Bals, Jan Sijbers, and Gustaaf Van Tendeloo. Measuring Lattice Strain in Three Dimensions through Electron Microscopy. *Nano Lett.*, 15:6996–7001, 2015.
- [136] Daniel O Sigle, Jan Mertens, Lars O Herrmann, Richard W Bowman, Sandrine Ithurria, Benoit Dubertret, Yumeng Shi, Hui Ying Yang, Christos Tserkezis, Javier Aizpurua, and Jeremy J Baumberg. Monitoring morphological changes in 2D monolayer semiconductors using atom-thick plasmonic nanocavities. *ACS Nano*, 9(1):825–830, 2015.
- [137] C. L.D. Lee and K C Hewitt. First demonstration of surface enhanced-stimulated Raman spectroscopy (SE-SRS) using low-power CW sources. *Faraday Discussions*, 205:227–232, 2017.
- [138] Jian Wu, Awnish K. Gupta, Humberto R. Gutierrez, and Peter C. Eklund. Cavity-Enhanced Stimulated Raman Scattering from Short GaP Nanowires. *Nano Letters*, 9(9):3252–3257, sep 2009.

Appendix A

Comparison of Hot-Spot Density

The three-orders of magnitude difference in SERS intensity measured between aggregates dried down onto a substrate and those measured in solution is in line with a back-of-the-envelope calculation of the reduction in hot-spot density within the focal spot. This appendix walks through the very rough estimations used to check these orders of magnitude are sensible.

To estimate the number of nanoparticles measured at any one time in solution we first need to estimate the focal depth probed. With an NA of 0.75 for the objective lens used, and a refractive index $n \approx 1.4$ for the solution, the focal depth, d , of region probed can be calculated to be

$$d = \frac{\lambda n}{NA^2} \approx 1.6 \times 10^{-6} \text{ m} \quad (\text{A.1})$$

giving an estimated focal volume of $1.2 \times 10^{-12} \text{ cm}^3$. The nanoparticle supplier (BBI Solutions) quotes the concentration of nanoparticles to be $9 \times 10^{10} \text{ cm}^{-3}$, therefore at any one time the number of nanoparticles in the focal spot of the laser is ≈ 0.1 .

When considering the aggregates dried onto a substrate we first consider the number of nanoparticles that could possibly fit in a 2D projection of the laser focal spot, assuming there is no contribution from those hidden behind the top layer. The spot diameter of the laser is $1 \mu\text{m}$, so assuming a perfectly round laser spot, this gives a spot area of $\approx 785\,000 \text{ nm}^2$. The 2D projection of NP surface area is calculated to be $\approx 1250 \text{ nm}^2$, assuming the nanoparticles are perfectly spherical (which is known not to be the case). The maximum number of nanoparticles that could therefore fit inside the focal spot is ≈ 600 . However, if we then assume that only $1/3$ of the spot area contains nanoparticles due to the fractal geometries of the aggregates, we arrive then at an estimate of 200 nanoparticles measured.

The ratio of number of nanoparticles probed at any time in solution compared to dry is therefore $0.1 : 200 = 1 : 2000$, giving the 3 orders of magnitude observed in experiments.

Appendix B

Room-Temperature Picocavity Examples

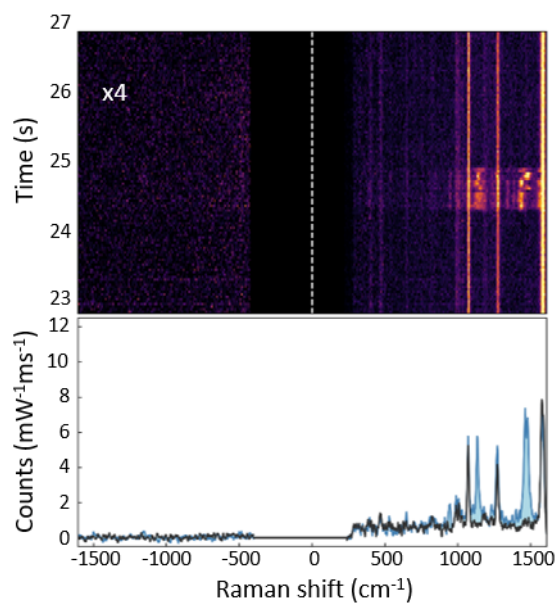


Fig. B.1

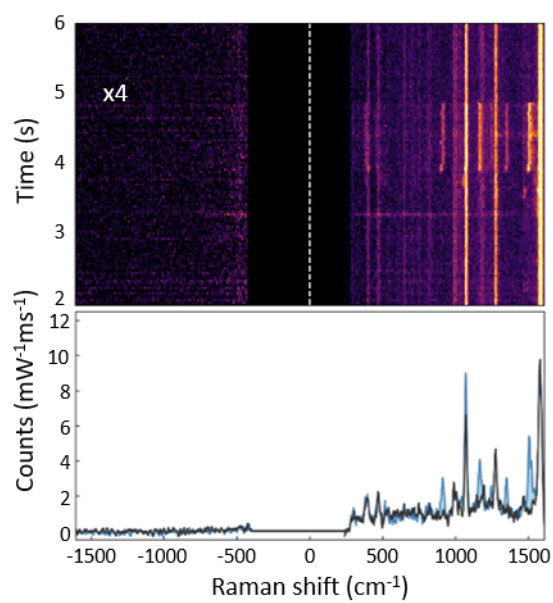


Fig. B.2

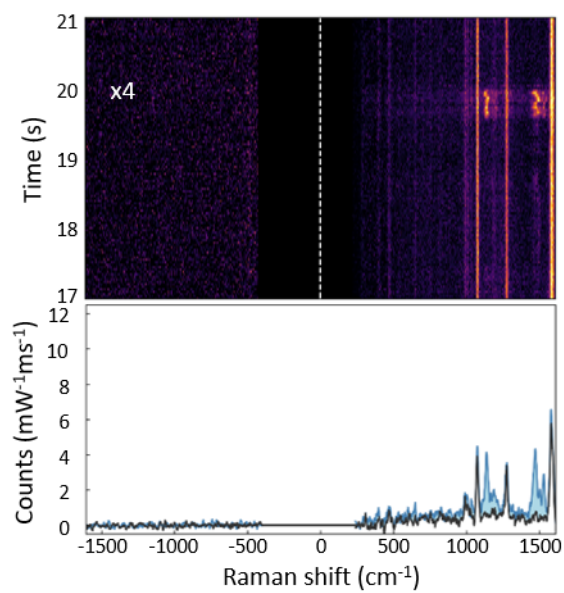


Fig. B.3

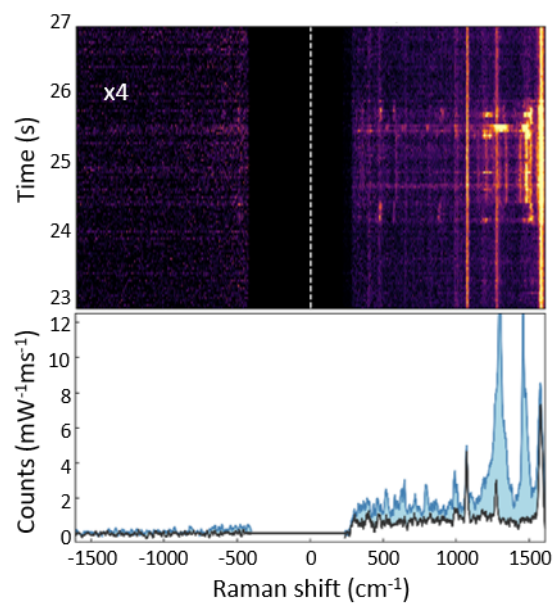


Fig. B.4

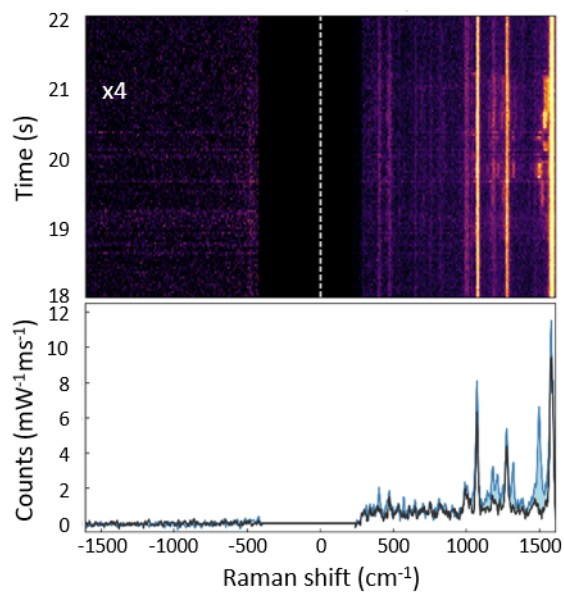


Fig. B.5

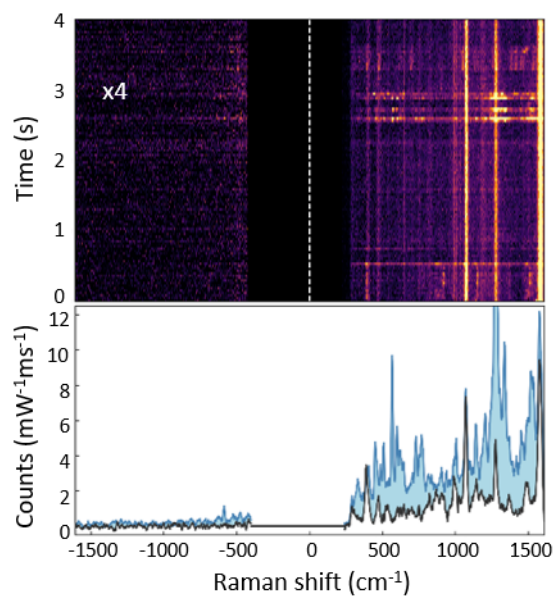


Fig. B.6

Appendix C

Derivation of the ERS Background Increase

Here the derivation of the proposed increase in ERS background due to a patch of reduced ω_p is given.

The displacement field perpendicular to the surface must be conserved from the dielectric gap into the metal, therefore:

$$\epsilon_{metal}E_{metal} = \epsilon_{gap}E_{gap}. \quad (C.1)$$

The penetration into the metal is given by

$$e(\omega_p) = \frac{E_{metal}}{E_{gap}} = \frac{\epsilon_{gap}}{\epsilon_{metal}(\omega_p)}. \quad (C.2)$$

In the defect region ω_p is reduced, therefore so is ϵ_{metal} therefore penetration into this patch ($e(\omega_p - \Delta\omega_p)$) increases:

$$e(\omega_p - \Delta\omega_p) = \frac{\epsilon_{gap}}{\epsilon_{metal}(\omega_p - \Delta\omega_p)}. \quad (C.3)$$

The skin depth δ_{\perp} is inversely proportional to this field penetration, $\delta_{\perp} \propto 1/e$, because it depends on the metal permittivity. The ERS in the metal giving rise to the flare is proportional to the 4th power of optical field in the metal, multiplied by the volume in which this field penetrates within the metal of $\pi a^2 \delta_{\perp}$, so that:

$$I_{flare} \propto \pi a^2 \delta_{\perp} (eE_{gap})^4. \quad (C.4)$$

Assuming the Poynting flux is conserved for metal-insulator-metal plasmons propagating inside the gap waveguide, hence $|E_g|^2 k_{||}$ is conserved, this leads to enhancement in the field within the dielectric at the centre of the facet of $E_g \propto \sqrt{\epsilon}$. This is indeed supported by the simulations, for instance when reducing $\omega_p = 9\text{ eV}$ to 6.5 eV gives a +24 % increase in E_g as predicted.

Therefore the increase in ERS background at a defect of reduced ω_p is given by:

$$\frac{I_{flare}}{I_{noflare}} = \left(\frac{a}{w}\right)^2 \frac{e}{e'} \left(\frac{e'\sqrt{e'}}{e\sqrt{e}}\right)^4, \quad (\text{C.5})$$

where $e' \equiv e(\omega_p - \Delta\omega_p)$. This therefore simplifies to

$$\frac{I_{flare}}{I_{noflare}} = \left(\frac{a}{w}\right)^2 \left[\frac{e(\omega_p - \Delta\omega_p)}{e(\omega_p)}\right]^5, \quad (\text{C.6})$$

as shown in the text.